Upscaling thin film solar cells for water treatment devices

Paolo Maggioni 4622731

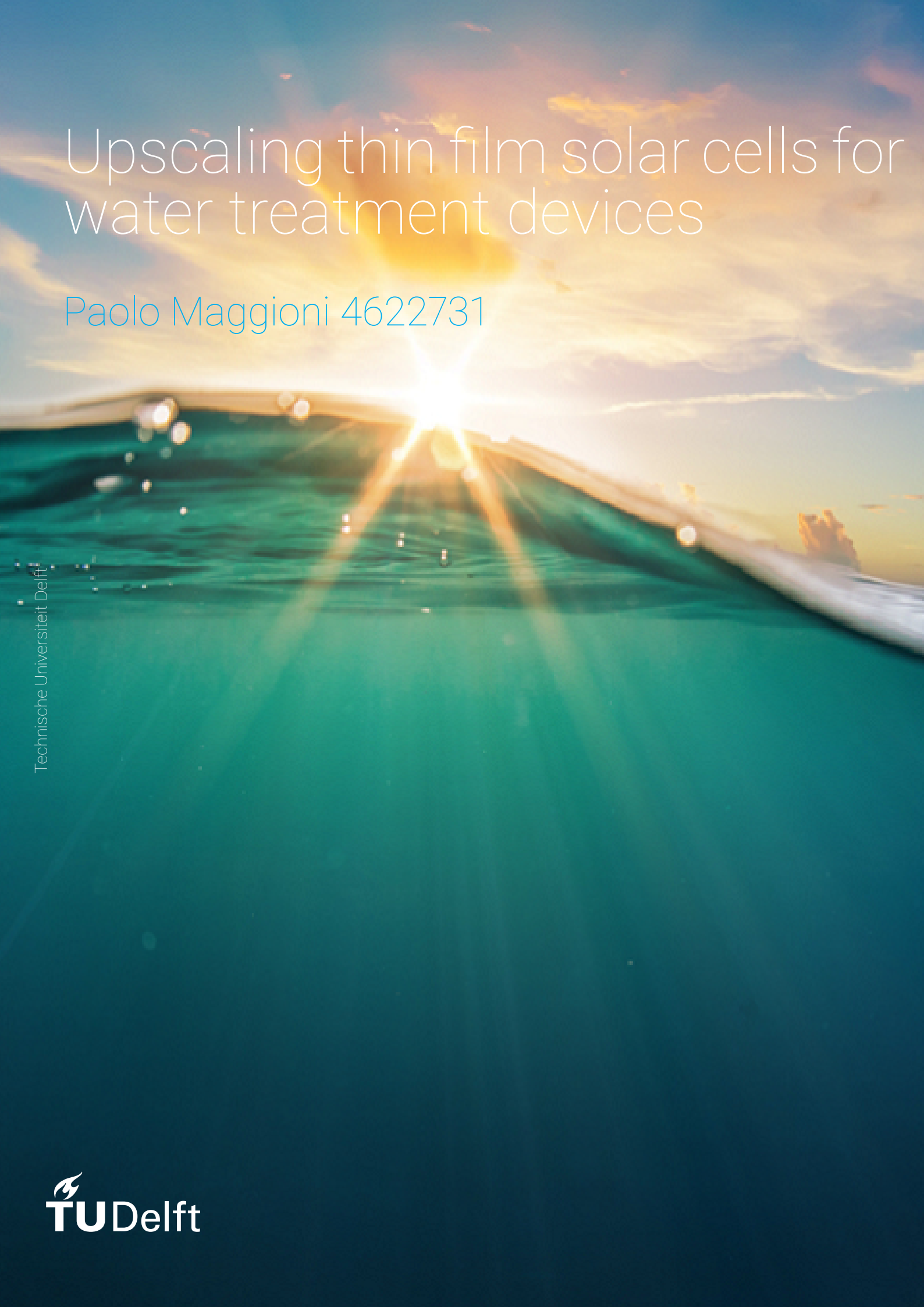

Technische Universiteit Delft

TU Delft

Upscaling thin film solar cells for water treatment devices

by

Paolo Maggioni 4622731

to obtain the degree of Master of Science

at the Delft University of Technology,

to be defended publicly on Wednesday September 19, 2018 at 2:00 PM.

Student number:	4622731	
Project duration:	September 1, 2017 – September 19, 2018	
Graduation committee:	Chair:	Prof. dr. ir. A. H. M. Smets
	Daily supervisor:	MSc. T. De Vrijer
	Reviewer:	Dr. ir. O. Isabella
	External Reviewer:	Dr. ir. L. M. Ramirez Elizondo

This thesis is confidential and cannot be made public until September 19, 2018.

TU Delft

Abstract

The availability of clean drinking water and various energy sources has always been taken for granted and considered to be infinite throughout human history. However, nowadays, we have reached a historical moment in which we are over-exploiting the Earth's resources. The reduction of the high level of pollution in the air and in the water is one of the main challenges that the next generations will have to face. Photovoltaic technologies offer a clean and cheap solution for both water purification and hydrogen generation for energy storage.

The main goal of this thesis is to upscale lab-scale thin film solar cells, by a factor of 600, optimized for water treatment devices. To this end, two alternative solutions have been explored.

On the one hand, a metallic front contact grid has been designed to minimize the power losses in large area pin superstrate solar cells. On the other hand, a thin film mini-module has been manufactured by isolating small area nip substrate solar cells and connecting them in parallel.

The implementation of the front metallic grid has enabled the upscaling of pin superstrate amorphous silicon solar cells by a factor of around 10. Additionally, the laser ablation process needed for dividing the sample into multiple cells has been studied and optimized for nip substrate amorphous silicon devices. Finally, some of the major problems that cause the formation of shunts have been identified. However, the relatively high density of shunts through the amorphous silicon bulk prevents the device from achieving higher efficiencies at larger dimensions.

Preface

The end of this thesis project marks the end of my career as a student. Many people should be mentioned and thanked for having made the two years in Delft an amazing experience.

First of all, I would like to thank my daily supervisor, Thierry, for his supervision and patience. The several times I walked into his office he was always available for discussions and suggestions. Thanks also for the scrupulous work he has done in correcting this report, to make it a more clear and interesting manuscript. I would like to thank Prof. Dr. ir. Arno Smets for the possibility of carrying out this project under his supervision and for his contagious optimism. Furthermore I would like to thank Dr. ir. Olindo Isabella for being part of my thesis committee and for the possibility of working under his supervision during the PV Lab course. Besides that, I would like to thank him for his willingness to help students like me that were not under his supervision and for the times he gave me advice when we met in the corridors. Thanks to Dr. ir. Laura Ramirez Elizondo as well, for being part of my thesis committee as external member.

This thesis could not be completed without the fundamental help of the technicians of the EKL laboratory. A big thanks, therefore, to Martijn Tijssen and Stefaan Heirman for the incredible work they carry out daily. Without their effort the machines would not be constantly available. Thanks also for the interesting discussions we had, that helped me more than once in solving problems I was facing during the project.

Furthermore, my gratitude goes to Gianluca Limodio, to always find some time to help me and giving suggestions, both in the cleanroom or in the daily work (and during the amazing matches with *Atletico Ribusciados*).

Many students from all over the world have enriched my stay here during the last two years. I would like to start thanking all the *setties*, which in one way or another have been part of my everyday life. Thanks to my office mates, Simona, Chris and Aurora for the coffee brakes and for being there when the work was tiring and the end of the thesis seemed far away. Thanks to Yifeng, for the help during my work in the cleanroom and for the amazing gasoline/whiskey you made me try; I am still wondering how it did not corrode all my organs! Thanks to Sandeep, for being a perfect colleague in the PV Lab and for showing me that anyhow, no matter if it rains or snows, smokers can always *go for a smoke*.

Thanks to the amazing Italian-Delftian group, Irene, Nicolò, Giacomo, Fillo, Raffa, Marco and all the others for the parties, the bbq's and all the things we have done together.

Thanks to all my friends back in Italy, especially to the *Secessione* group, Alessio, Anna, Marta, Panz and Susi, and to Fra, for showing me that friendship remains, even if we meet only once per year. I hope there will be more occasions for spending time together again in the future.

An enormous thanks with all my heart goes to my Dutch family. To *Dr. Master Sensei Pelotudo* Andrés, for being both the most photogenic friend I have, but also the most helpful and generous person I have ever met. To Martina, for the diabetes I will have in few years due to the tonnes of butter you used, but also for the needed touch of femininity and happiness you brought since the moment you entered the door of our house. To Vitto, for showing me that there is no limit to *la tamarraggine*, but also for always being there to cook and amazing dinner, or when I needed just a few words from a friend to cheer me up. To Thomas, for his amazing skills as *quarterback* but mostly for being one of the best friends I have ever met, to whom I could confide every single thing that was coming to my mind. To Luca, for demonstrating me that it is possible to survive eating rice and chicken, for the we time spent crying watching Candreva but also for all the laugh we had due to your incredible sharp humor. To Taglia, for showing me that common people are made of

70% water but that there are some that are made out of 90% air, but also for being a funny, lovely and generous *parassita* (double insult to remain coherent). To Ciola, for showing me that in reality names are not important and the World is populated by *cari*, but also for being an amazing smiling optimistic person that makes every day a better day. Finally to Julen, for the unforgettable *scatarroso* alarm that was waking me up every morning, but also for being there every single day of the last year, crying and laughing together and for showing me that even the strong and rude Basque men have a huge generous heart. To all of you, you will always be one of the best memories of my life. I hope we will meet often in the future.

I will never be able to thank my family enough. My sisters, for being always the example I could follow. The perseverance and the passion you put in everything you have done have always been an inspiration for me. My parents, for all the sacrifices you made in all your life in order to give me the opportunity to form myself and grow as a man. The feeling of being loved that I experienced every time when I came home, will accompany me every single day of my life. I will never be able to express my gratitude for what you have given to me.

Lastly, I would like to thank Vale. We went through many problems and difficulties and we solved everything growing stronger together. You are an example of strength that I admire. You give me joy and happiness and you showed me that even in the darkest moment, a smile can solve everything. In the last two years you have always been there, on the other side of the phone, listening to me in the good and in the bad situations. The certainty that anyhow, good and bad times, I always have someone next to me, will always accompanies me. I feel blessed of having you and I am looking forward to experience the World together with you.

Paolo Maggioni 4622731
Delft, September 2018

Contents

List of Figures

List of Tables

List of Abbreviations

η Solar cell efficiency. xiii, 58, 59, 62

ϕ Laser average fluence. 14, 39, 41, 42, 44

a-Si:H Hydrogenated amorphous silicon. 4, 5, 9–11, 31, 32, 60, 63, 64, 66, 67

a-Si:H/a-Si:H Tandem Hydrogenated amorphous silicon. x, xiii, 3, 31, 35–37, 65

a-Si:H/a-SiGe:H/nc-Si:H Hydrogenated amorphous silicon/Hydrogenated amorphous silicon germanium/Hydrogenated nanocrystalline silicon. 3

a-Si:H/nc-Si:H Tandem amorphous silicon and nano crystalline Silicon. 31

$\mathbf{A_{pulse}}$ Area of a pulse spot. 14, 15

AZO Aluminum Zinc Oxide. x, xiii, 11, 19, 20, 29–35, 48, 51, 57, 59, 61–64, 67

c-Si Cristalline Silicon. 8, 12

$\mathbf{E_g}$ Energy gap. 5

$\mathbf{E_p}$ Average energy per pulse. 14, 15

EEMCS Electrical Engineering Mathematics and Computer Science. 19

EKL Else Kooi Laboratory. v, ix, 19–21, 23, 29, 35, 47, 55, 57, 59

$\mathbf{f_{cut\text{-}off}}$ Cut off pulse repetition frequency. 41, 42, 44, 70

$\mathbf{f_{laser}}$ Pulse repetition frequency. xi, 15, 22, 23, 39, 41–46

FF Fill Factor. xiii, 7, 26, 31, 58–60

FTO Fluorine doped Tin Oxyde. x, xii, 11, 29, 31, 35–37, 57, 59, 60, 63, 65, 67

HAZ Heat affected zone. 13, 14, 45–47

ITO Indium Tin Oxide. x–xiii, 11, 19, 20, 29–32, 48, 50, 52, 53, 60–62, 64, 67

J-V Current density-Voltage. ix, xii, 6, 8, 24, 26, 57, 60, 62

$\mathbf{J_{mpp}}$ Maximum power point current density. xiii, 7, 26, 58

$\mathbf{J_{sc}}$ Short circuit current density. xiii, 6, 7, 29, 31, 57–59

Mark-loops Number of marking repetition loops. xi, 39, 41

MOPA Master Oscillator Power Amplifier. 22

n_s Number of extraction points. 35

nc-Si:H Hydrogenated nano crystalline Silicon. 31

$O_{percentage}$ Percentage of pulse overlapping. 39, 41, 42, 44, 46, 52–54

$P_{\%}$ Percentage of the laser average output power. xi, 39, 41–44, 46

P_{avg} Average power per pulse. 15, 42

p_{el} Total fractional electrical losses. 28

P_{in} Incident power. 7

P_{mpp} Power at maximum power point. 7, 26

P_{out} Average output power of the laser. 39, 41, 42, 44

P_{peak} Laser peak power. 15, 39, 44

p_s Fractional optical losses. 27

p_t Total fractional losses. 28

PECVD Plasma Enhanced Chemical Vapor Deposition. 19, 21, 55

Q_p Pulse width. xi, 14, 15, 22, 23, 39, 41–46, 70

r Spot size radius. 15

R_{sh} Shunt Resistance. xiii, 11, 58, 60

R_s Series Resistance. xiii, 58

RF Radio Frequency. 21

SEM Scanning Electron Microscopy. 23, 25, 26, 39, 49, 52

STC Standard Test Conditions. 26

T laser period. 15

T_e Electron cooling time. 13

T_i Lattice heating time. 13

T_l Laser pulse duration. 13

TCO Transparent Conductive Oxide. ix, xi–xiii, 10, 11, 19, 20, 23, 24, 29, 31–37, 48–51, 53, 55, 57–59, 61, 63, 65, 67

TLM Transmission Line Measurement. x, 24, 25, 31

V_{mpp} Maximum power point voltage. xiii, 7, 26, 58

V_{oc} Open Circuit Voltage. xiii, 7, 26, 29, 31, 56, 58, 59

v_{scan} Speed of the laser. xi, 22, 39, 41, 43, 44, 46

1

Introduction

The possibility of using energy and water has been the main driver for civilization and development. Fire, at first, pushed men to evolve: the opportunity of cooking, defending and warming up are considered among the most significant achievements of humanity, strongly improving human lifestyle [1]. Water, then, marked the moment when, from nomadic, men turned into sedentary: agriculture and breeding became common activities, and people started to aggregate in the first communities [2].

The availability of clean drinking water and of various energy sources has always been taken for granted and considered to be infinite throughout human history. However, nowadays, we have reached a historical moment in which we are overexploiting the resources Earth has provided us.

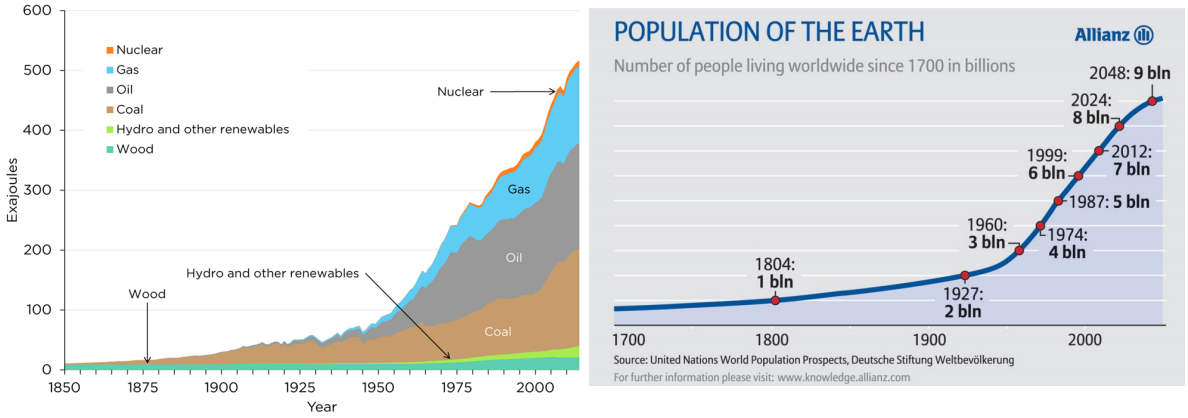

(a) **(b)**

Figure 1.1: (a) World energy consumption by source since the beginning of the 19th century (Adapted from [3]) and **(b)** World population and annual growth rate since 1750 and projections until 2100 (Adapted from [4])

Since the beginning of the 19th century, the succession of technological improvements, the industrial revolution and the electrical and electronic ages, highly increased energy demand (fig.1.1a). Fossil fuels have become in the last two centuries the main source of energy. Besides being finite resources, fossil fuels generate an enormous amount of hazardous exhaust gases that have exponentially increased the greenhouse effect. Energetic infrared light, which naturally would escape to space, are trapped in the atmosphere significantly increasing the average temperature of the Globe.

Past measurements and future predictions show that global warming will have a serious impact on the Earth, endangering human kind and several different animal species. On a long term, the progressive and gradual melting of the polar ice caps has been forecasted, leading to the increase of sea water level, of droughts in tropical countries as well as of hurricanes, tornados, heavy rains and floods in areas far from the equator. Contemporaneously, the induced higher amount of moisture in the air is among the major causes of higher diffusion of dangerous diseases [5].

Moreover, the improved life conditions originated from the technological revolution has caused a significant increase of the world population, which is now almost 8 billion people (fig.1.1b), and, as a consequence, of drinking water demand. Human activities are also responsible for the dangerous increase of water pollution that is jeopardizing human health. Ashes produced when burning fossils fuels mix with water vapor and result in acidic rains that, together with accidental oil leakages, chemical fertilizers and pesticides, are inducing a significant increase of the acidity of water basins [6]. Bad human behaviour, such as bad or absence of sewage and wastewater treatments or the thousands of tones of plastic that every year are dispersed in the oceans, are among the causes of the high level of pollution that is characterizing surface water. Nowadays, due to the continuous decrease of water quality, nearly 780 million people do not have access to drinking water and almost 2.5 billion people suffer from inadequate sanitation or diseases caused by water contamination [7].

A drastic change in human habits and a deeper penetration of renewable energy in every sector are the only solutions to guarantee a clean and safe future to the next generations. One of the main issues that has hindered the diffusion of renewable technologies in the past decades is their inconstant and unpredictable energy production: power production, in fact, highly depends on weather conditions. Moments of over production continuously alternate moments of insufficient generation. Therefore, today, efficient and clean storage solutions are one of the main issues to be solved in order to allow renewable energy to take over dangerous fossil fuels. On a long term, a deeper penetration of renewable sources in the energy production system can also cease the negative trend that drinking water quality has undertaken. On a short term, however, clean and safe water treatment technologies are urgently needed. The implementation of photovoltaic both for water splitting and water cleaning devices can generate new and clean concepts that can change the paradigm of these two technologies.

1.1. State of the art of water treatment devices

Electrolysis of water is an electrolytic phenomena that allows to split water in the two basic molecules: H_2 and O_2. Electrolysis is a redox reaction characterized by two half reactions in which water is first oxidized generating $2H^+$ and $2e^-$ (eq.1.1), which are then reduced into H_2 molecule (eq.1.2) [8].

$$H_2O \rightarrow \frac{1}{2}O_2 + 2H^+ + 2e^- \tag{1.1}$$

$$2H^+ + 2e^- \rightarrow H_2 \tag{1.2}$$

Overall, therefore, the total reaction is

$$H_2O \rightarrow \frac{1}{2}O_2 + H_2 \tag{1.3}$$

Each half reaction requires a specific potential to take place: the sum of the 2 potentials results in the total voltage needed, which is 1.23 V. In reality, however, several losses occur in a water splitting device, and an overpotential of almost 0.8 V must be applied as well.

A common device for water splitting is the *Hofmann Voltameter* system. It is formed by three different cylinders: the two on the sides are connected to the electrodes and host the 2 half reactions, while the one in the middle is necessary to refill the system with water. The whole system is connected to a voltage source that applies the correct potential to the device. Figure 1.2 shows a lab-scale Hofmann Voltameter system integrated with a PV system solution. Although the use of photovoltaic modules to supply the correct Voltage needed to split the water is a wise and sustainable option, the presence of control electronic devices introduces additional losses and costs that can reduce the appeal of such a set-up. At TU Delft, different studies have been carried out in order to implement photoelectrodes to directly activate the electrochemical reaction from solar energy without using electronic components. A triple junction a-Si:H/a-SiGe:H/nc-Si:H thin film solar cell is considered to guarantee the optimal combination of current and voltage for an efficient and effective reaction [9].

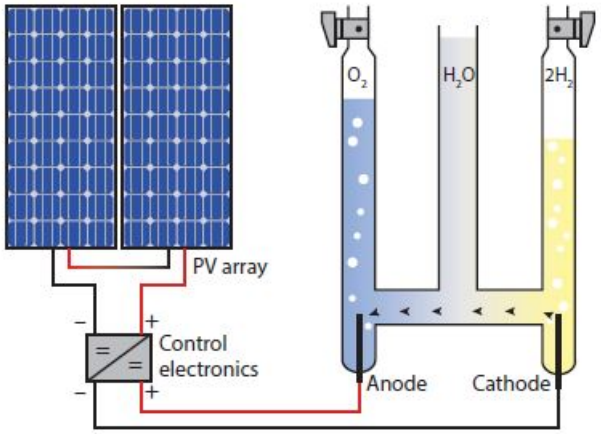

Figure 1.2: Example of a Hofmann Voltameter integrated with a PV system. Retrieved from [8].

Photoelectrochemistry can also be applied in water treatment devices to purify water from hazardous pollutants. Until now, biological, physical and chemical treatments have been the most common methods. Although being considered economically convenient, biological treatments do not allow the degradation of many toxic compounds. Physical treatments, instead, do not destroy the pollutants but only collect and transfer them. Chemical methods, lastly, offer safe solutions for the removal of a wide variety of pollutants, but requires the continuous replacement of the chemicals. Integrated indirect PV-oxidation devices, instead, allow the removal of several different toxic compounds by advanced oxidation processes that use solar energy. Polluting and dangerous chemicals are oxidized and decomposed into simpler and innocuous molecules, which are then safely dispersed in the environment. At TU Delft, studies about the removal of phenol, one of the most common water pollutants, showed that a constant voltage is needed too. An applied voltage equal to 1.6 V is the most efficient and effective value to drive the reaction. Such a voltage, however, is considerably higher than the open circuit voltage either of common single junction solar cells, or of crystalline silicon solar cells. Therefore, a-Si:H/a-Si:H resulted as the most suitable technology for this application [7].

All the experiments carried out in the previous studies, both for water splitting and for water cleaning, were based on solar cells with a total area of 16 mm^2. The goal of this thesis is to try to tackle the most common problems related to upscaling thin film solar cells.

1.2. Outline of the thesis and research questions

The process of upscaling thin film solar cells have been divided in three subparts, which are summarized in these three main research questions:

- *Is it possible to design a front contact grid to improve the charge carrier collection in a large area thin film solar cell?*
- *What are the optimal parameters for the isolation of a solar cell by laser scribing and what are the major drawbacks of using a single wavelength infrared laser scriber?*
- *Is it possible to deposit large area PIN or NIP solar cells by using the previously optimized techniques?*

In order to clearly present the steps undertaken and the theoretical background needed to carry out the experiments, this report has been divided in seven main chapters. In the first chapter the main motivations about upscaling thin film solar cells are illustrated. Chapter 2 introduces the fundamental principle of the photovoltaic effect, the structure of an a-Si:H solar cell and its main issues. The steps for a thin film module fabrication by laser scribing and the main parameters that characterize a solar cell are shown as well in this Chapter. Chapter 3 shows the most significant devices used during the execution of the experiments. In chapter 4, different front contact grid designed are analyzed in order to find the optimum for the reduction of power loss in large area thin film solar cells. Chapter 5 shows the optimization of the laser scribing process. In chapter 6 the previously optimized mask and laser process are implemented in the deposition of large area a-Si:H pin superstrate and nip substrate solar cells respectively. Lastly, in chapter 7 the main conclusions drawn during the project are summarized and some recommendation for future projects are suggested.

2

Theoretical background

This chapter provides an overview of the technologies used in this thesis and introduces the concepts required for upscaling the indirect PV-oxidation devices introduced in section 1.1. In the first part of the chapter, section 2.1 the photovoltaic effect is explained. The second part, section 2.2, explains the main parameters needed to characterize the performances of a solar cell are explained. Section 2.3, presents an overview of amorphous silicon (a-Si:H) thin film technology. Section 2.4 gives an overview of the main problems with upscaling thin film technology: shunt leakages. Finally, section 2.5 introduces the main steps needed for thin film module fabrication, with a special focus on laser ablation.

2.1. Photovoltaic effect

The photovoltaic effect is the fundamental working principle of a solar cell. It corresponds to the generation of a potential difference at the junction of two different materials when exposed to light [8].

In order to clearly explain the photovoltaic effect, a short introduction on the properties of solid state materials is needed. Solid state materials are characterized by two different allowed energy states in which electrons can move: the *valence band* and the *conduction band*. The former represents the energy levels of electrons bound in the lattice, while the latter of unbound free electrons. Depending on the relative position between the two edges of the energy levels, that is, the energy difference between the edges of the conduction and of the valence band, called *Energy gap* (E_g), solid materials can be classified in three different groups (Fig.2.1): *insulator*, *semiconductor* or *conductor* materials. The first group is characterized by a large E_g: at room temperature the energy difference is so high that are not thermally excited electrons. The valence band, hence, is fully occupied while the conduction band is empty. The second one is constituted by a slightly thermally populated valence band and by a slightly depopulated conduction band, generating a small electrical conductivity. The third group is formed by not separated valence and conduction bands: the conduction band is partially occupied leading to a high electrical conductivity [10].

Having introduced the concepts of Energy gap and of conduction and valence bands, it is now possible to explain the photovoltaic effect. The photovoltaic effect can be described by three different steps:

- **Generation of charge carriers due to the absorption of photons in the materials**:
  as introduced by Albert Einstein in 1905, the solar light can be described by well defined en-

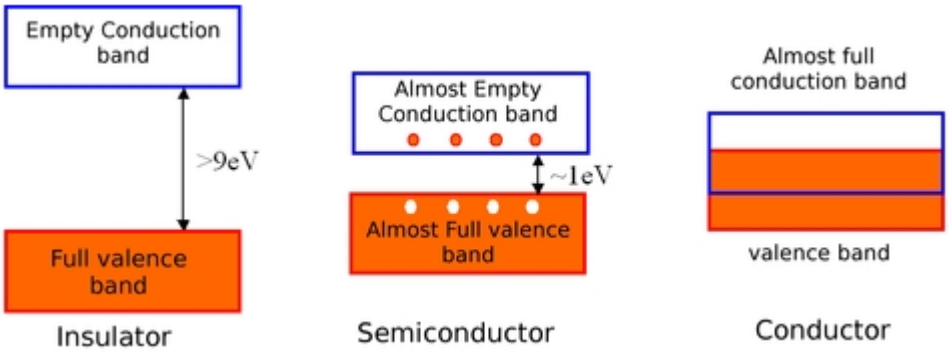

Figure 2.1: Representation of energy bands [10].

ergy quanta, the photons, each of them carrying a specific amount of energy equal to

$$E = h\nu \tag{2.1}$$

where h is the Planck's constant and ν is the frequency of the light. If the energy absorbed from a photon is enough to excite an electron from its energy level in the valence band to the conduction band, that is, if it is higher than the Energy gap, an *electron-hole* (e^--h^+) pair is generated. When moving from the valence band to the conduction band, indeed, an electron leaves a void behind that behaves like a positive particle, the so called *hole* (fig.2.2a).

- **Separation of the photo-generated charge carriers in the junction**:
once generated, electrons and holes tend naturally to recombine in order to bring the material back to the most stable condition. Therefore, two *semipermeable membranes* are used in order to avoid the natural recombination of the charge carriers and enhance their collection: one membrane allows only the transition of electrons, while the other one only of holes. In solar cell devices these membranes are p-type and n-type doped materials [8].

- **Collection of the photogenerated charge carriers**:
the two semi-permeable membranes create, therefore, two side areas where the electrons and the holes migrate. An external circuit connects them together: electrons flow from one side to the other, generating electricity, and recombine with the holes at the metal-absorber interface[8].

Figure 2.2b shows the last two steps presented above using a very simple solar cell model.

2.2. Current density-Voltage characteristic

Before introducing the characteristics of thin-film technology, the parameters used to characterize the electrical properties of a solar cell are explained. Solar cells commonly described by current density-voltage, or J-V, curves (an example is shown in fig. 2.3) that vary based on the technology used.

Several relevant parameters can be identified from the graph:

- **Short circuit current density (J_{sc})**: the short circuit current is an irradiance dependent quantity and it is strictly related to the type and dimension of the solar cell. It corresponds to the current flowing through the external circuit when the solar cell electrodes are short circuited. Commonly, in order to remove the dimension dependency, short circuit current density is

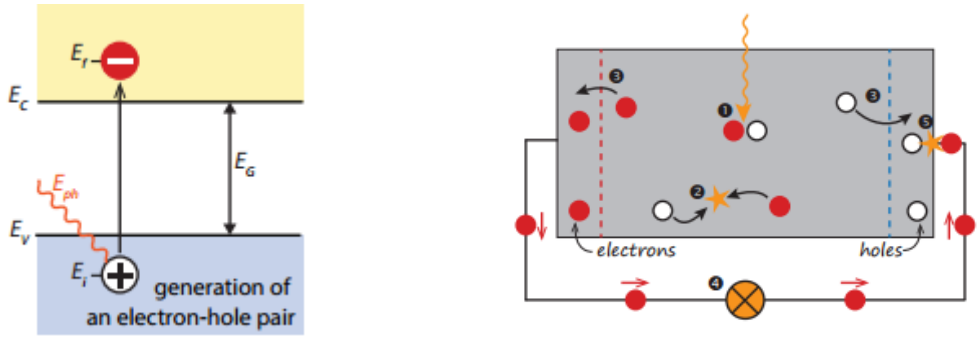

(a) **(b)**

Figure 2.2: **(a)** illustrates the excitation of an electron in a semiconductor from the valence band to the conduction band by a photon with energy E_{ph}. **(b)** shows a schematized solar cell: **1** charge carrier separation; **2** charge carriers recombination; **3** charge carriers separation due to the semipermeable membranes; **4** flow of electrons through the external circuit; **5** charge carriers recombination at the metal absorber interface [8].

used to describe the behaviour of a solar cell: it corresponds to the value of the short circuit current divided by the area of the solar cell and it is usually measured in $\left[\frac{mA}{cm^2}\right]$ [8];

- **Open circuit voltage (V_{oc})**: it is the maximum voltage a solar cell can deliver and corresponds to the potential occurring when no current is flowing. It is function of the photo generated current density (J_{ph}) and can be calculated as follow [8]:

$$V_{oc} = \frac{k_B T}{q} \ln\left(\frac{J_{ph}}{J_0} + 1\right); \tag{2.2}$$

- **Maximum power point (P_{max} or P_{mpp})**: the maximum power point (in this thesis the notation P_{mpp} will be preferred), corresponds to the operating point at which the solar cell produces the maximum amount of power. P_{mpp} is described by a corresponding voltage-current density pair: the maximum power point voltage, V_{mp} or V_{mpp}, and the maximum power point current density, J_{mp} or J_{mpp}, respectively [8];
- **Fill Factor (FF)**: it is the ratio between P_{mpp} and the maximum theoretical power that would be produced if a solar cell would be able to work at V_{oc} and J_{sc} simultaneously. Therefore, FF can be computed as follow [8]:

$$FF = \frac{J_{\text{mpp}} \times V_{\text{mpp}}}{J_{\text{sc}} \times V_{\text{oc}}}; \tag{2.3}$$

- **Conversion efficiency (η)**: it indicates the ability of the solar cell in converting incident power into electric power. Therefore, η corresponds to the ratio between P_{mpp} and the incident power (P_{in}) and can be calculated with the following equation [8]:

$$\eta = \frac{P_{\text{mpp}}}{P_{\text{in}}} = \frac{J_{\text{mpp}} \times V_{\text{mpp}}}{P_{\text{in}}} = \frac{J_{\text{sc}} \times V_{\text{oc}} \times FF}{P_{\text{in}}}. \tag{2.4}$$

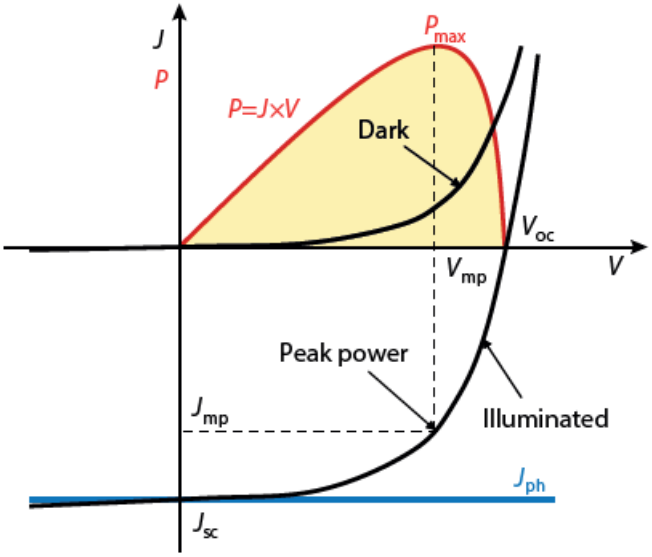

Figure 2.3: Example of a typical J-V curve of a solar cell under illumination and under dark conditions [8].

2.3. Thin film solar cell technology

Different solar cell technologies exist on commercial scale. In water treatment and water splitting devices thin film technologies are usually used.

The reduction of production costs was, at first, the major concern that pushed photovoltaic to invest in thin film technology: compared to crystalline silicon (c-Si), it requires less and cheaper materials [11]. Beside the lower production costs, thin film solar cells offer also a higher flexibility that allows the implementation in many different applications.

Several different thin film technologies are nowadays fabricated on commercial scale: III-V technology, thin-film silicon based technology, chalcogenide technology and organic photovoltaic solar cells technology. For the purpose of this thesis hydrogenated amorphous silicon (a-Si:H) is used.

The following subchapters describe the properties and the characteristics of a-Si:H and of all the single layers that constitute a thin film solar cell.

2.3.1. Amorphous silicon

Amorphous is a term originating from ancient Greek, ($\alpha\mu o\rho\phi\omega\zeta$), which literally means "without definite shape" (fig.2.4). The atomic structure of amorphous silicon is, indeed, characterized by a continuous random network (CRN) and by a not defined structure [8]. Compared to crystalline silicon, which is defined by an ordered lattice, the orientation and structure is not repeated identically in every direction: in amorphous silicon, the silicon bond angles and the silicon-silicon bond lengths are irregular and distorted. Figure 2.5a is a schematic representation of the typical amorphous silicon lattice. The figure shows also the presence of different types of defects: compared to crystalline silicon, in which defects are due to the absence of atoms in the crystal lattice, in amorphous silicon they are due to anomalies in the covalent bonds and to the fact that not all the Si atoms are surrounded by a quartet of atoms, generating the so called *dangling bonds* [12]. This in-

duces a relatively high defect density, in the order of 10^{16} cm^{-3}, which leads to a high recombination rate, as well as to a short lifetime and diffusion length of the excited charge carriers. *Shockley-Read-hall recombination* is, indeed, the main limiting phenomenon: the presence of impurities and dangling bonds creates allowed energy level between conduction and valence band, where electrons are trapped and recombine before without generating any power.

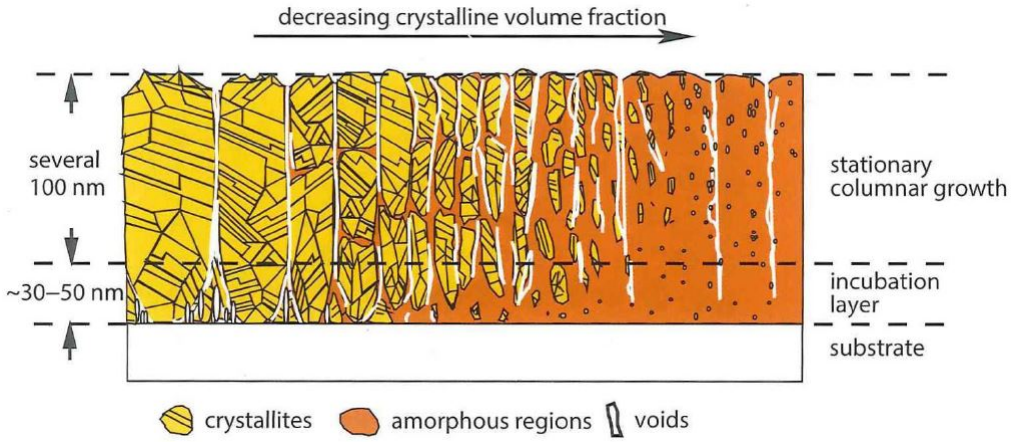

Figure 2.4: Representation of the crystalline phase of thin-film silicon, with a high crystalline phase on the left and a completely amorphous phase on the right. Retrieved from [8].

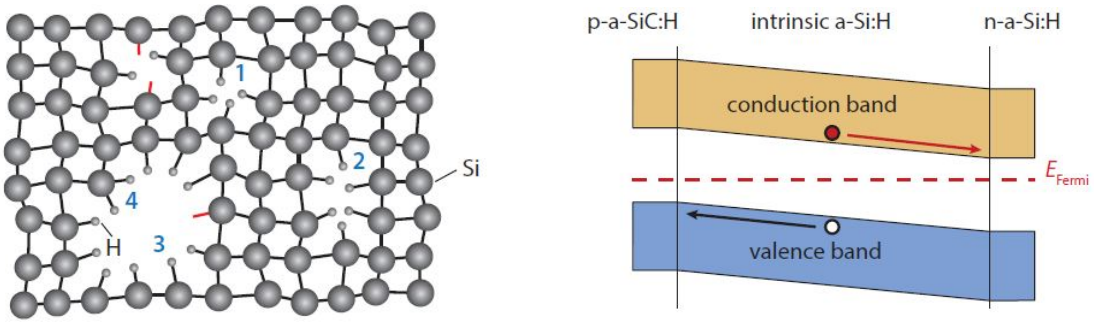

(a) **(b)**

Figure 2.5: (a) shows a representation of the amorphous structure and of its characteristic defects: (1) monovacancies, (2) divacancies, (3) nanosized voids with monohydrides (one hydrogen atom in the bond) and (4) dihydrides (two hydrogen atoms in the bond). Adapted from: [8].**(b)** shows the typical band diagram of an amorphous silicon solar cell. Adapted from [8]

.

Because of the aforementioned high defect density, a-Si:H could not be used in its base form to manufacture efficient solar cells. The discovery that it could be doped even though it is a disordered material, opened a new window of opportunities for the development of thin film solar cell technology. Hydrogen can be used in order to passivate the free valence electrons of Si atoms, highly reducing recombination problems [13]. The generated alloy, hydrogenated amorphous silicon (a-Si:H), is characterized by a direct bandgap which varies from 1.6 eV to 1.8 eV, depending on the percentage of hydrogen in the alloy. Compared to crystalline silicon, which is defined by an indirect bandgap, the absorptivity of a-Si:H is considerably higher in the visible spectrum. Much thinner layers can, therefore, be used to produce a solar cell [8].

Due to the short charge carrier lifetime and to the poor hole mobility, thin film a-Si:H solar cells can not be manufactured by simply connecting a p-doped silicon layer with an n-doped silicon

layer, as conventionally done in the p-n junction. An induced electric field needs to be generated to improve the charge carrier mobility. Therefore, an intrinsic undoped layer (*i* in Fig.2.6) several hundred nanometers thick, is added in between the p and n layer in order to enhance the *drift transport process* rather than the *diffusion transport process*. This latter process is, indeed, limited by the high defect density. The generated electric field between the p and n layer prevents the recombination of electrons and holes pushing them towards the doped layers of the photoactive stack [13]. Once the charge carriers reach the p and the n side, diffusion transport becomes dominant again: hence, p and n doped layers are usually few nanometers thick. An illustration of the band diagram of an a-Si:H solar cell is shown in figure 2.5b.

Depending on the deposition sequence, thin film a-Si:H solar cells are called *pin* or *nip*: in the first case, the p-doped layer is deposited first, in the latter the n-doped layer. Solar cells, moreover, can be deposited in superstrate or substrate design: the former indicates that the top layer of the solar cell, the one that is impinged first by the light, is deposited first, while the latter indicates that the first deposited material is the bottom layer of the solar cell. Commonly, being the carrier lifetime of holes significantly smaller the the electrons one and being most of the carriers generated close to the front of the device, p-doped silicon layers are deposited in front of the n-layer. Therefore, superstrate configuration is usually used also to indicate the pin design of a solar cell, while substrate to indicate the nip design of a cell.

Although the composition of the layers can be similar and the only difference seems to be the deposition order, *nip* solar cells are more prone to shunts (See par.2.4) than *pin*. The reasons behind this phenomenon, however, are still not clear nowadays [13].

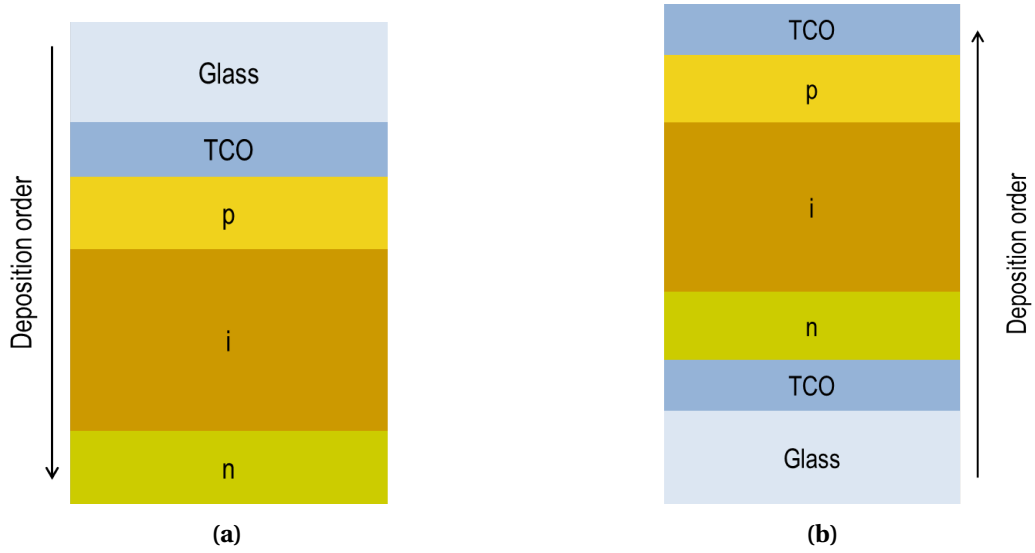

Figure 2.6: **(a)** *pin* structure of a solar cell. **(b)** *nip* structure of a solar cell. TCO stands for transparent conductive oxide

2.3.2. Transparent conductive oxide (TCO)

Compared to c-Si solar cells, the front contact of thin film solar cells is not characterized by a metal grid but by a transparent conductive oxide layer. TCOs are deposited on top of the p-layer to enhance the lateral transmission of charge carriers and to allow their collection. Regardless of the design of the solar cell, TCOs are usually optimized to minimize the reflected part of the incident light and to enhance transmission. Overall, therefore, TCOs must be characterized by high conductivity and transparency[8], they must be easy to deposit and they must guarantee a long chemical

and thermal stability [14]. The optimal combination of conductivity and transparency can not be usually met with stoichiometric oxides. TCOs are, hence, usually either doped or not stoichiometric materials and their compositions are studied to maximize the aforementioned properties.

For the production of thin film solar cells, Indium Tin Oxide (ITO) ($In_2O_3 : Sn$) is usually used as TCO, since it combines low electrical resistivity and absorption coefficient together with a high optical band gap. However, due to the scarcity of indium and its high price, several alternatives have been analyzed to substitute it. Approximately, for a good TCO material, the electrical resistivity should be lower than $\sim 10^{-4}\Omega\cdot$ cm , the absorption coefficient lower than 10^4 cm^{-1} in the near-UV and VIS range and the optical band gap bigger than 3 eV [15].

One of the alternatives that satisfies these requirements is Aluminum-doped Zinc oxide (AZO). AZO layers deposited at a temperature between room temperature and 300 °C, guarantee sheet resistance equivalent or even better than ITO, together with high transmission values. These values are maintained even when the deposition temperature changes from room temperature to 300 °C, hence AZO can be used also for temperature-sensitive technologies. Moreover, AZO is made of Earth abundant materials characterized by a low level of toxicity and low costs[14].

Fluorine doped Tin Oxide (FTO) ($SnO_2 : F$) is the TCO that has been widely used in the photovoltaic industry until today. The production of SnO_2 is cheaper than AZO and ITO. However, its conductivity is usually lower than of ITO. Additionally, fluorine is characterized by a high level of toxicity, which leads to significant environmental issues. Similar to FTO is also Cadmium doped Zinc Oxide which shows the same pros and cons as FTO [14].

Few other TCOs technologies are used on industrial scale, such as Indium Zinc Oxide, Hydrogenated Indium Oxide or Zirconium doped Indium Oxide. These technologies have not been studied during this Master Thesis project.

2.4. Shunt leakage

The electrical behaviour of a solar cell is usually represented by a simple equivalent electric circuit in which a diode and a current source are connected in parallel (fig. 2.7(b)). The diode represents the p-n junction, while I_{ph} represents the photogenerated current density. The two major parameters that influence the performance of a solar cell, clearly visible in the variation in the Fill Factor (see par. 2.2), are the series resistance and the shunt resistance (R_{sh}). The former represents the resistance that the current meets to reach the external circuit, while the latter represents some current leakages caused by defects in the junction of the solar cells or at its edges [8]. Figure 2.7(a) shows how an increase of shunt current affects the performances of a solar cell [16].

The generation of shunts is a crucial problem in thin film solar cells: due to the infinitesimal thickness of the deposited layers, in the order of nanometer range, even the presence of dust or small particles can cause inhomogeneties and shunts. Additionally, shunts can form also from diffusion of Al into a-Si:H doped layers. Indeed, at high temperatures Al can counter-dope the silicon layers creating, for example, a symmetrical pip structure which represents a point of charge carriers recombination. The application of a reverse bias for a certain period of time can counteract this phenomenon by diffusing out the undesired metal from the Silicon layers.

Since shunts depend on localized defects, the magnitude of leakage current can vary significantly and unpredictably from one cell to another, even when fabricated under the same conditions. Therefore, it is arduous to predict the output of modules/cells in advance, especially when evaluating large area solar cells or modules [16].

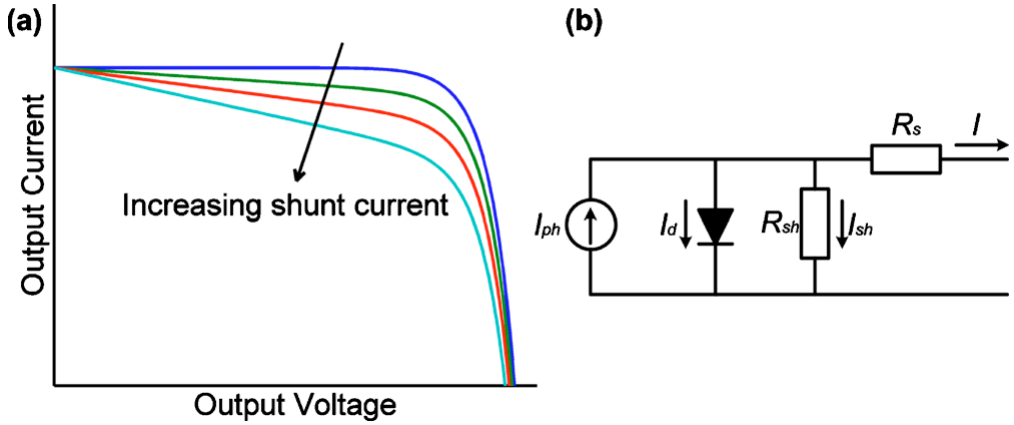

Figure 2.7: (a) Schematic of the variation of the Current-Voltage curves when the shunt current varies. (b) Equivalent circuit model for a solar cell. Adapted from [16].

2.5. Thin film module fabrication

Thin film materials for solar application introduced a new approach to module production in the photovoltaic industry. Compared to c-Si technology, in which the production of cells and modules consists of two completely different steps, for thin film materials the production of cells and modules can not be separated. Depositions of solar cell layers and laser scribes are performed alternately in order to series interconnect different cells in series. Because of this, the substrate (or superstrate) on which the layer is deposited can easily exceed a surface area of 1×1 m^2 [8].

For the sake of simplicity, a superstrate configuration on glass is taken into account to explain the process used to manufacture a thin film silicon module:

- at first, a transparent front contact is deposited on top of a glass wafer (fig. 2.8a). A first laser scribing step, called P1, is then performed in order to create gaps and divide the deposited layer in multiple strips (fig. 2.8b).
- secondly, the photoactive layer is deposited covering the transparent front contact and filling the previously generated gaps with the absorber layer (fig. 2.8d). The latter is then also ablated with a second process of laser scribes (P2). The laser is transmitted through the front transparent contact and absorbed only by the second layer(fig. 2.8d).
- lastly, the back metal is deposited and a similar process to the previous ones is performed by a third laser ablation (P3).

The whole area, is therefore divided along its length into narrow cells, almost 1cm wide and long as the width of the substrate. This process prevents the formation of electrical losses that would occur if the deposition is made on the whole glass wafer area. A deposition on a large area without laser patterning would, indeed result in a large area solar cell with a high current density: due to the extremely thin front and back contact (in nanometer range), very high resistive losses would be generated across the module. Moreover, this configuration allows the reduction of the effects related to shunts current leakages (explained in par 2.4).

Figure 2.8f shows the created series connection between two neighbouring cells: the current can flow from the back contact of one cell to the front contact of the subsequent one connecting them together. The figure illustrates, moreover, the existence of a *dead* area, the *interconnection width*, in which power is not generated and that varies from few hundreds micrometers to one millimeter. Figure 2.9 shows a microscopic view of the interconnection width[8] [17].

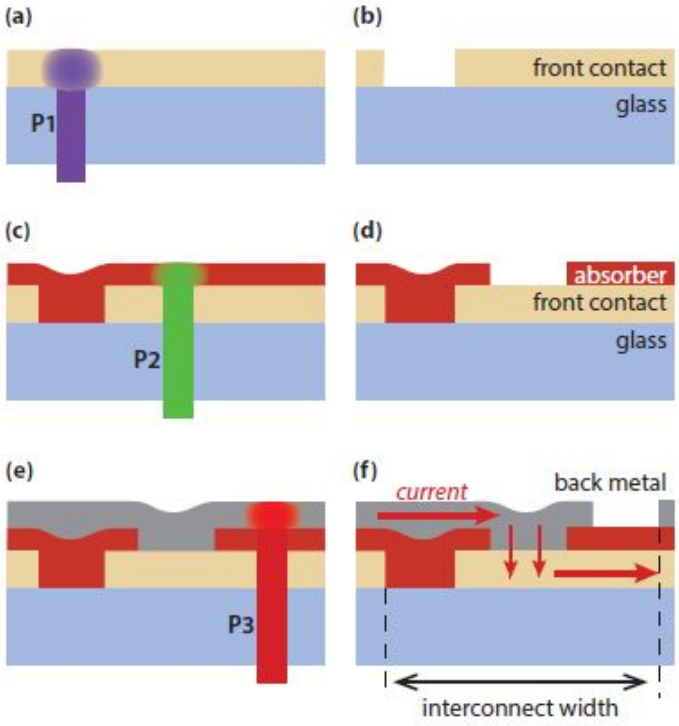

Figure 2.8: Representation of the interconnection technique for a thin film solar module [8]

.

2.5.1. Laser ablation principle

Laser scribing is a complex process that involves several different physical phenomena depending on the parameters that are used. When the leaser beam hits the material surface, the energy carried by the photons is immediately absorbed by the electrons in the conduction band and propagates through the material. To deeply explain the ablation process of the material, three characteristic time scales must be introduced: the electron cooling time (T_e), which is in the order of 1ps, the lattice heating time (T_i), which is proportional to its heat capacity and is larger than T_e, and the duration of the pulse laser (T_l). Depending on the timescale of T_l the mechanism of material removal changes (Fig2.10):

- when T_l is in the order of milliseconds, melting is the primary material removal mechanism. T_l is considerably longer than T_e and T_i and heat can easily propagate through the material by heat transfer. Matter does not evaporate, but it is removed and transferred to the sides. Heat transmission, moreover, is responsible of damages and microcracks that can affect the physical properties of the material itself.
- When T_l is in the order of nanosecond, the laser energy absorbed by the electrons can be transmitted to the lattice. Due to the fast pulse, thermal equilibrium between the electrons and the lattice can be easily reached. Melting is still the main phenomenon for material ablation, but, if enough energy is transmitted from the laser pulse, the material can immediately evaporate. Since the laser pulse is three orders of magnitude faster than the previously mentioned one, the heat affected zone (HAZ) is usually significantly smaller.
- When T_l is in femtosecond scale, the duration of the pulse laser is considerably shorter than T_e. Electrons can be heated up individually and instantly, and they transmit their energy to their positive lattice ions. If the energy is high enough, lattice structure bonds can be broken,

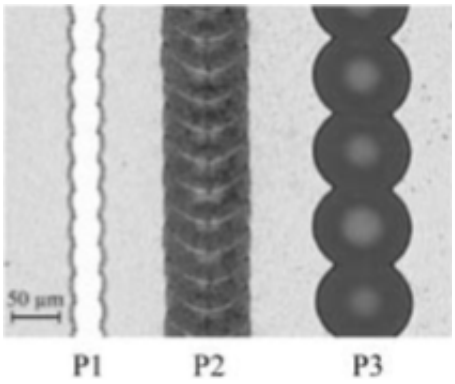

Figure 2.9: Microscopic view of an interconnection region with optimized laser parameters [17].

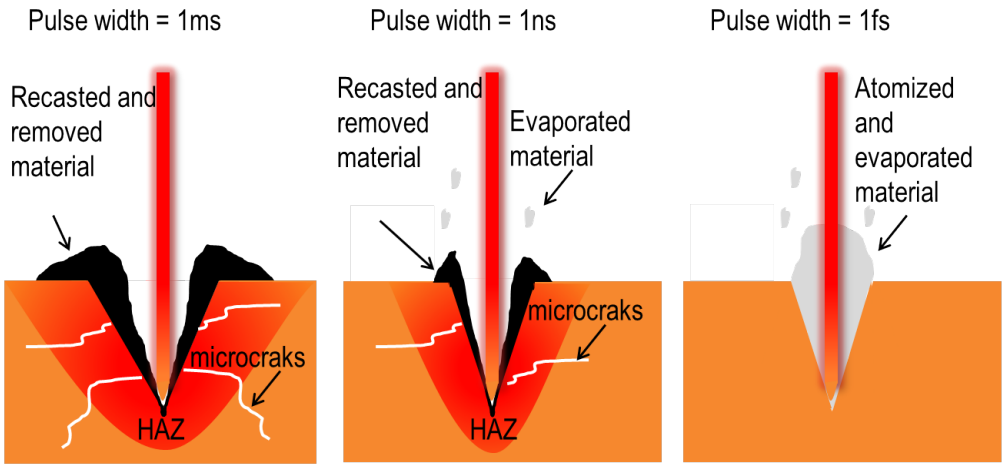

Figure 2.10: Schematic of the incidence of pulse width on laser ablation. The pulse width reduces by a factor of 10^{-3} from left to right

leading to a solid-vapor transition. The overall phenomenon in the order of femtosecond, hence, heat can not diffuse to the neighbouring atoms. A HAZ free cut is therefore available. Ultrafast lasers, however, are adopted only for a few applications, due to the high cost of this technology [18].

The material ablation process, therefore, does not only depend on the total energy [J] per focal area [cm^2] given at every single pulse, the *laser fluence*. It also depends on the pulse width: different pulses with different laser settings can transmit the same amount of energy to the same area, but in case of really different pulse widths (Q_p) the ablation phenomenon changes significantly (Fig. 2.10).

The average laser fluence (ϕ) can be easily computed from the laser ablation parameters [19]:

$$\phi = \frac{E_p}{A_{pulse}} \tag{2.5}$$

where:

- E_p corresponds to the average energy per pulse and can be calculated by dividing the average laser power (P_{avg}) by the pulse repetition rate (f_{laser}), which is equal to 1/T (in which T corresponds to the period between 2 consecutive pulses)

$$E_p = \frac{P_{avg}}{f_{laser}} \tag{2.6}$$

- A_{pulse} is the area on which one single pulse is incident

$$A_{pulse} = \pi r^2 \tag{2.7}$$

  in which r is the spot size radius

From E_p, it is also possible to evaluate the peak power transmitted in every single pulse, by simply dividing the energy per pulse by the length of the pulse itself (Q_{pulse})

$$P_{peak} = \frac{E_p}{Q_p} \tag{2.8}$$

Figure 2.11 illustrates a schematic of the previously mentioned parameters.

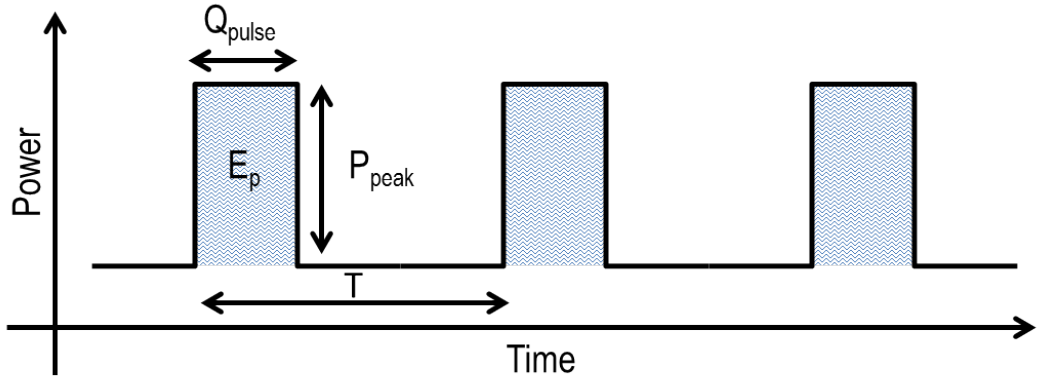

Figure 2.11: Schematic of pulse laser working principle in time.

In addition to the parameters affecting the intensity of the pulse itself, the shape of the designed line depends also on the percentage of pulse overlapping (fig. 2.12). Too low repetition rates can result in individual spots disconnected from each others while, in case of too high repetition rates, problems related to lifting of the surrounding material can arise.This is, for example, a problem for thin film series connections, as it will be explained in section 2.5.2.

Pulse overlapping can be analytically analyzed as follow:

$$O_{percentage}[\%] = \left(1 - \frac{v_{scan}}{2r \cdot f_{laser}}\right) 100\% \tag{2.9}$$

in which:

- $O_{percentage}$ is the percentage of pulse overlapping
- v_{scan} is the movement speed of the laser in mm/s [20].

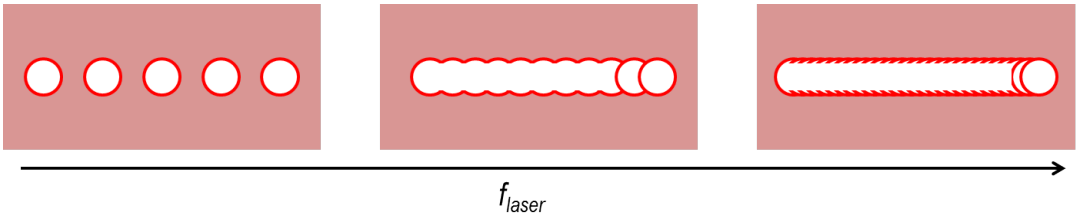

Figure 2.12: Schematic of pulse overlapping with increasing repetition rate.

2.5.2. Laser scribing parameters

As previously introduced, in the photovoltaic market lasers have been employed for series interconnection in thin film solar modules. Different lasers are used in order to perform the three P1, P2 and P3 scribes.

P1 is usually executed with an infrared laser, width a wavelength of 1064 nm. Depending on the intensity of the laser power, the quality of the cut varies. For a peak power between 10 kW and 11 kW a complete removal of the front layer can be achieved [17].

The choice of the laser to perform P2 is more complex: because the beam must be transmitted through the TCO layer and absorbed only in the photoactive stack. A green laser with a wavelength in the range of 532 nm is usually used with peak power in between 500 W and 1000 W. For not high power densities a smooth and clear removal of the absorber layer can be performed without cracking the TCO layer.

The most critical step is the back contact patterning. In principle, the laser type had to be chosen with the same criteria as for P2: it has to travel through the first two layers without cutting the material and remove only the back metal. Different types of lasers have been used in literature, both in the green [17] and red [8] wavelength range, showing however a similar issue: the formation of flakes (fig 2.13b). These residual metal particles can easily short circuit two neighbouring cells or connect the front to the back contact introducing local shunts at the laser scribes. The main cause of flakes generation is pulse overlap. Figure 2.13 shows clearly the difference between a well defined laser ablation 2.13(a) in which the different laser spots are clearly visible and in which flakes are not created, and a line engraved with a laser whose parameters were out of the optimal range and in which laser spots overlap generating a significant amount of imperfections (2.13b). Moreover, the larger the pulse overlap is, the smaller the other parameters become influential in the flakes generation. During the experiments carried out at the Research Centre Jülich, Haas et al. [17] found that the flake formation can be determined according to the angle α between the tangents to the two subsequent laser spots at their contact point, as shown in figure 2.14. If α is larger than 90° the dashed area indicated in figure 2.14(a) is removed and flakes are generated [17]. In case the angle is lower than 90°, the tear of the new ablated area reaches the edge of the previous spot without leading to a new flake formation.

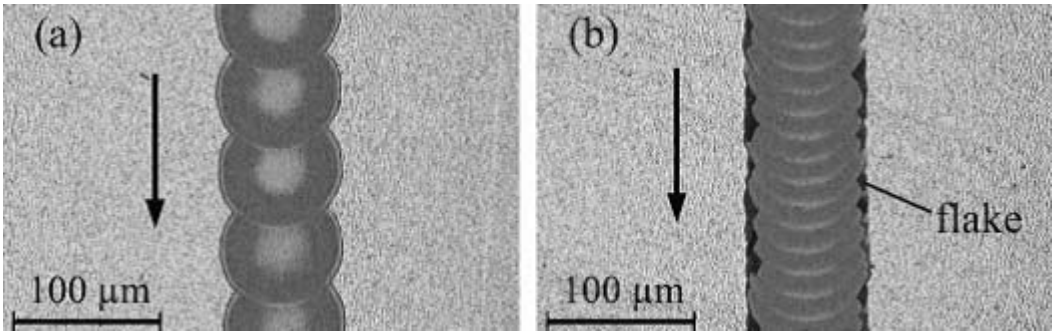

Figure 2.13: (a) Optical micrographs of a well defined laser ablation. **(b)** and common representation of flakes formation in case of wrong patterning parameters. Adapted from [17].

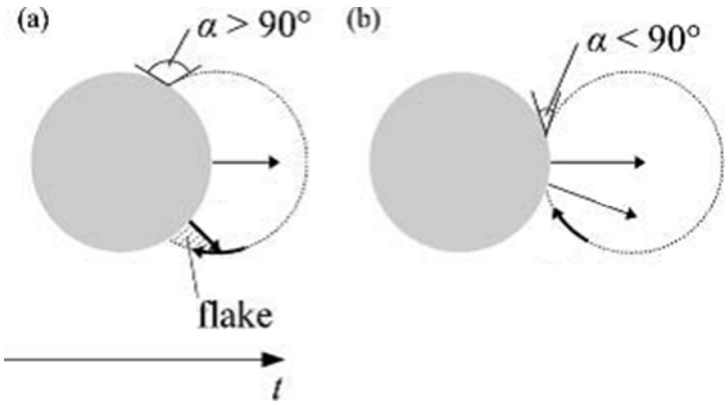

Figure 2.14: Mechanism of the flakes formation at the back contact of the solar cell. Adapted from [17].

3

Methodology

In the first part of this chapter, all the manufacturing and fabrication processes of the solar cells deposited during this project, together with the theory on which they are based, are presented and explained in detail. In the second part the laser scriber setup is shown. The last part of the chapter consists of a detailed discussion of all the setups used for the measurements.

3.1. Deposition techniques

In the first part of the thesis, different TCO layers have been deposited in order to analyze their sheet resistances, while at the end of the project thin film solar cells have been manufactured. In the following subsections, magnetron sputtering for the deposition of ITO and AZO layers, electron beam and thermal evaporation for the deposition of the front and back contacts and plasma enhanced chemical vapor depositions (PECVD) are described. All these processes have been performed at the Else Kooi Laboratory (EKL) of the Electrical Engineering, Mathematics and Computer Science (EEMCS) faculty of TU Delft.

3.1.1. Magnetron sputtering deposition

Magnetron sputtering is a physical vapor deposition technique based on the adhesion of excited atoms onto a substrate. First, plasma is generated by maintaining inert argon gas (Ar) under vacuum and inside an electromagnetic field. The superimposed electromagnetic field leads to the dissociation of positively charged ions, which are then accelerated by potentials ranging from few hundreds to few thousands electron volts [21]. The positively charged argon ions (Ar^+) bombard the target material, which evaporates and deposits onto the substrate [8].

At EKL, magnetron sputtering is carried out in two different chamber systems: during this thesis project, ITO has been deposited in a multi-chamber machine from Polytechnik (ZORRO), while for the deposition of AZO a multi-chamber system from Elettrorava S.p.a (AMIGO) has been used. For both systems, depositions could be controlled by varying the following parameters:

- Deposition pressure
- Heater temperature
- Deposition time
- Deposition power
- Input gas flows

For the deposition of the two TCO layers, two different target materials have been used. ITO is made bombarding a 10% SnO_2 and 90% In_2O_3 target, while for AZO a ZnO and 2% Al target is used [8].

3.1.2. Metal Evaporation

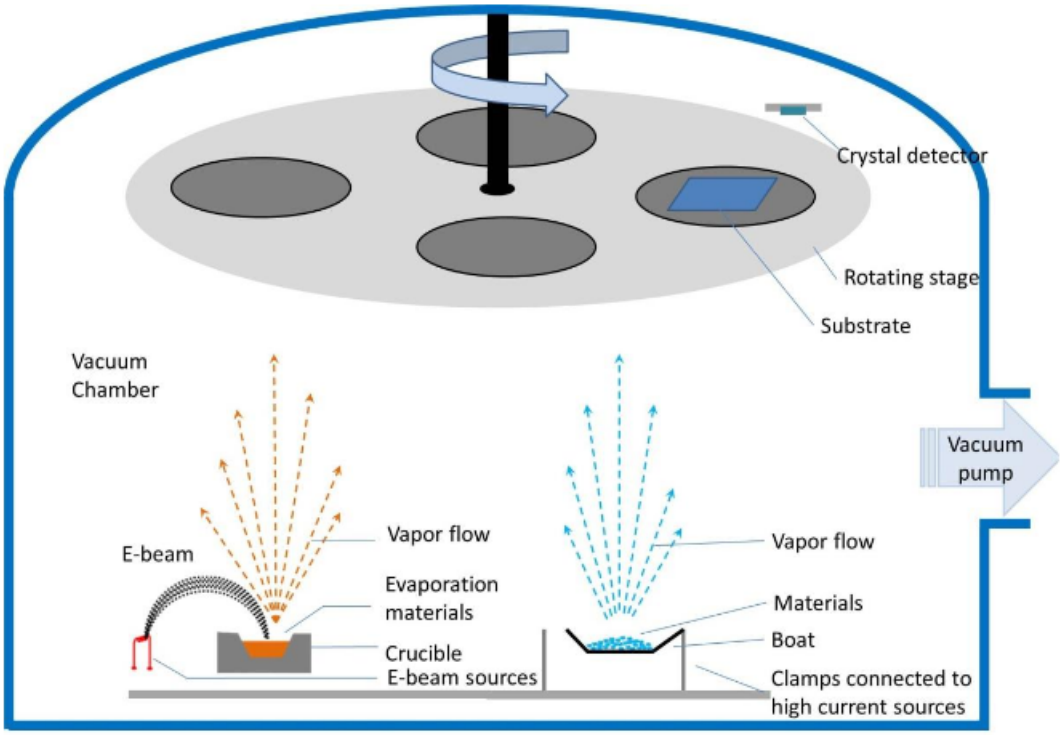

Figure 3.1: Schematic of the PRO500S Provac evaporation system at EKL. The e-beam evaporation system is represented on the left hand side, while the thermal evaporation system is represented on the right hand side. Adapted from [11]

Metal evaporation techniques are adopted for the deposition of the front and back contacts. The Provac PRO500S system is employed at EKL for both thermal and electron-beam evaporation. The two methods are based on similar processes: a vacuum is generated in a chamber, the primary material is evaporated and atoms transfer from the source material to the substrate where they condense.

Thermal evaporation is preferred for materials with low melting point temperature: in Provac this methodology is used for the deposition of Silver (Ag). Silver is placed in a tungsten boat which is then heated up by resistive heating with high current sources [11].

Electron-beam evaporation, on the other hand, is preferred for materials with high melting point temperature. Current flows through a tungsten filament leading to electron emission which are then accelerated by applying a high voltage between the filament and the earth, and focused into a uniform beam with a controlled electromagnetic field [22]. When the e-beam collides with the target material, electrons energy is transferred to the target as heat. The material, as a consequence, evaporates and deposits onto the substrate. For the deposition of different materials, Provac is equipped with a rotating table with four independent ceramic crucibles that allow the deposition of Al, Cr, Ti and SiO_2. Particular is the case of aluminum: although it has a low melting point, it is melted

through e-beam to prevent the formation of alloys with the tungsten boat [11].

At the top of the vacuum chamber, Provac is provided with a rotating plate with four separate slots for samples. The full process is automated and software-controlled [11]. Figure 3.1 shows a schematic overview of the metal evaporation system of the group.

3.1.3. Plasma Enhanced Chemical Vapour Deposition

All the silicon layers deposited for this thesis project have been fabricated using Plasma Enhanced Chemical Vapor Deposition (PECVD). The same multi-chamber system introduced in section 3.1.1, AMIGO, has been used for these processes. Figure 3.2 shows a schematic overview of the machine.

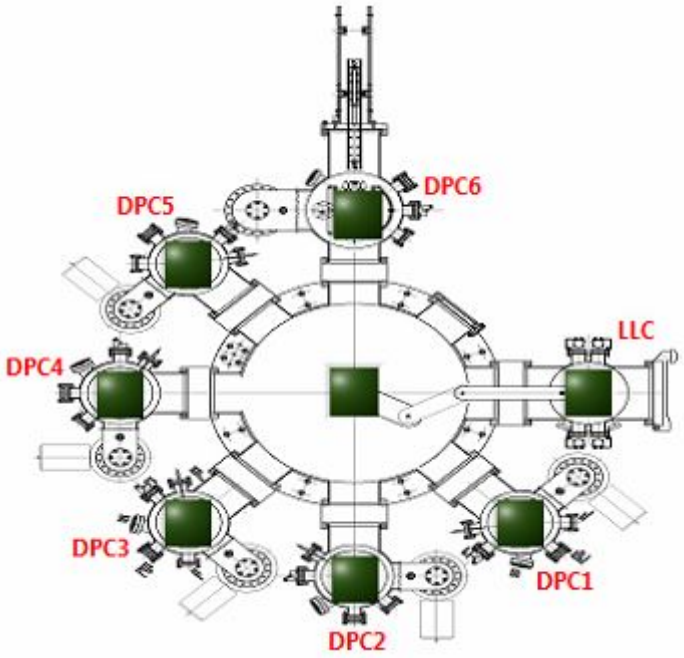

Figure 3.2: Schematic overview of the AMIGO multi-chamber system at EKL. This figure corresponds to the user-software interface. *DPC* stands for *Deposition Processing Chamber* while *LLC* for *Load Lock Chamber*

PECVD is based on the formation of plasma from various gas mixtures. Silane (SiH_4), methane (CH_4), hydrogen (H_2) and carbon dioxide (CO_2) are mixed in different quantities, depending on the parameters of the required material, in an ultrahigh vacuum reaction chamber. An electromagnetic field is then induced between two conductive electrodes through an RF signal. The interaction between the electromagnetic field and the gas particles allows the ignition and formation of the plasma. From the plasma, reactive particles are then released and transported by diffusion or drift onto the substrate [11]. The difference in potential between the particles and the substrate allows the deposition of the material and the formation of the thin film layer [8].

The whole system can be used in full automation and can be controlled remotely with a computer. The material properties of the deposited films can be controlled through the variation of the deposition parameters: pressure, temperature, time, power and gas flow ratio. The choice of the excitation frequency is also fundamental for the properties of the plasma: for all the thin film silicon depositions in AMIGO, it has been kept at a constant value of 13.56 MHz.

3.2. Laser scriber

In the second part of the thesis, solar cells have been laser scribed in order to isolate the edges and to design the innovative nip configuration.

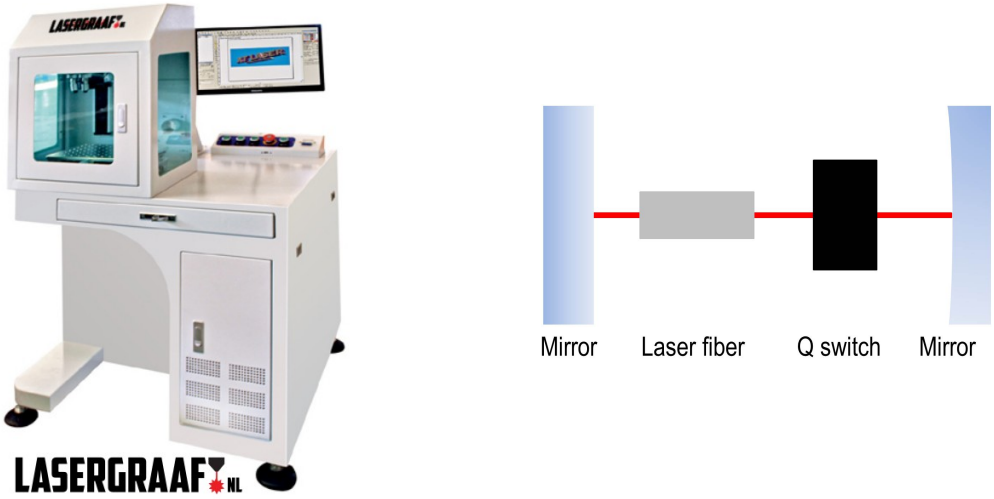

(a) **(b)**

Figure 3.3: (a) Mopa Fiberlaser working station, retrieved from [23]. **(b)** Scheme of Q-switch laser system.

At TU Delft, a Master Oscillator Power Amplifier (MOPA) fiber laser from Lasergraaf (fig. 3.3a) is used. MOPA is a new laser technology that consists of a single frequency laser, namely the master laser, and an optical amplifier to increment the output power. The system, moreover, is based on a Q-switching technology. Q-switching consists in the generation of short intense pulses, typically between tens and hundreds of nanoseconds [24]. Compared to a continuous wavelength laser, a Q-switch laser is excited without a continuous feedback by blocking the reflection from one of the end mirrors by using a switch (fig. 3.3b). When the switch opens, a rapid and significant population inversion is generated, meaning that the atoms in excited state become suddenly the majority in the active medium, resulting in a really short pulse with a significant high peak power [25]. Compared to the more common continuous wavelength lasers, the device used at the faculty guarantees more flexibility allowing to control the pulse width (Q_p), the repetition rate (f_{laser}), the average power intensity (P) delivered and the speed of the laser movement (v_{scan}).

The working station is equipped with a 30Watt Ytterbium Pulsed fiber laser [26]. The test data of the adopted laser are shown in table (tab.3.1)

Moreover, the repetition rate can vary from 50 kHz to ~1000 kHz and the pulse width from 2 ns up to more than 200 ns.

Lastly, the working station is fully controlled with the EzCad2.10UNI software. This software has a CAD-user interface for the drawing of all the desired features. The software, moreover, allows the control of all the introduced parameters.

Table 3.1: Test data of the laser used at the faculty [26]

Characteristic	Test Conditions	Min	Typ	Max	Test Results	Unit
Mode of operation			Pulsed			
Nominal Average Output Power	f_{laser}=75kHz Q_p=200ns	30.5	31		31	W
Central Emission Wavelength	P_{out}=P_{nom} f_{laser}=75kHz Q_p=200ns	1055	1064	1075	1061.3	nm

3.3. Measurements

In order to measure the results obtained with the different experimental activities, different measurement equipment have been used. In the following subsections, **1)**the sheet resistance measurement system, **2)** the contact resistance measurements, **3)** the Scanning Electron Microscopy (SEM) and **4)** the class AAA Wacom WXS-156S-10,AM1.5G continuous solar simulator are described.

3.3.1. Sheet resistance measurement

For the design of the front contact of the solar cell carried out in chapter 4, sheet resistances of different TCOs were required. The four-probe measurement system *CMT-SR2000N-PV Sheet Resistance/Resistivity Measurement System* from Advanced Instrument Technology at EKL has been used to perform the measurements.

A four-probes measurement systems consists of four different equally separated probes: the two external probes (probe 1 and 4 in fig. 3.4) are connected to an ammeter and a constant current power supply, while the two central probes (2 and 3) are connected to a high impedance voltmeter.

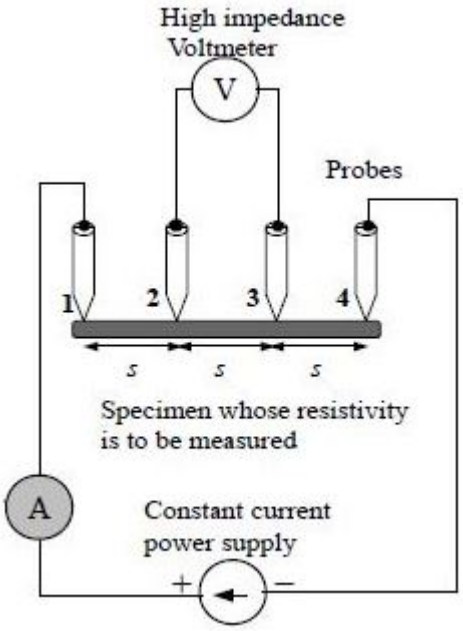

Figure 3.4: Scheme of the 4 probes measurements setup [27]

By measuring the voltage difference between the two inner probes and knowing the input current,

it is possible to measure the volume resistivity of the material with the following formula:

$$\rho = \frac{\pi}{\ln 2} \times \frac{V}{I} \times t \times k \tag{3.1}$$

in which ρ is the volume resistivity [$\Omega \cdot$ cm], V is the measured voltage difference [V], I is the input current [A], t is the thickness of the sample [m] and k is a correction factor.

Dividing ρ by the thickness of the layer, it is possible to calculate the sheet resistance (σ) of the sample [28]

$$\sigma = \frac{\pi}{\ln 2} \times \frac{V}{I} \times k. \tag{3.2}$$

The advantage of calculating the sheet resistance of a material, which is measured in Ω/sq (or $\Omega/\square$), is that sheet resistance is size independent and is only related to the properties of the material.

3.3.2. Contact resistance measurement

For the analysis carried out in chapter 4, electrical contact resistance measurements were required. Contact resistance is, by definition, the resistance that occurs between two surfaces when they are put in contact. For the first type of large area thin film cell designed in this thesis, therefore, the contact resistance between aluminum, the front contact, and the different types of TCOs have been measured.

One of the most common methods for the evaluation of contact resistances is the Transmission Line Measurement (TLM). This technique is based on the fact that the resistance occurring between two electrical contacts, deposited on top of a semiconductor, is equal to the sum of the electrical resistances generated at the contact-semiconductor interface and of the intrinsic resistance of the semiconductor itself. Therefore, theoretically, reducing the distance between the two deposited contacts to zero, the total resulting resistance should be equal to twice the metal-semiconductor interface resistance. Therefore, eight small aluminum contacts of the same size but separated by increasing distance have been deposited on top of the TCOs (fig. 3.5a). The resistances occurring between each couple of subsequent contacts have been then linearly interpolated. Half of the value occurring at the intersection between the interpolated line and the y-axis corresponds to the resistance between the contact and the layer below. Figure 3.5b shows an example of the aforementioned method.

These measurements were carried out with the dark J-V curve measurement setup. The setup is formed by the 6517A Electrometer from Keithley [29], to effectively measure the resistances, and by the TP03000A Thermal Inducing Vacuum Platform from Temptronic [30], to fix the sample and keep it at a constant temperature. The whole system, lastly, is software controlled to easily show an overview of the obtained results.

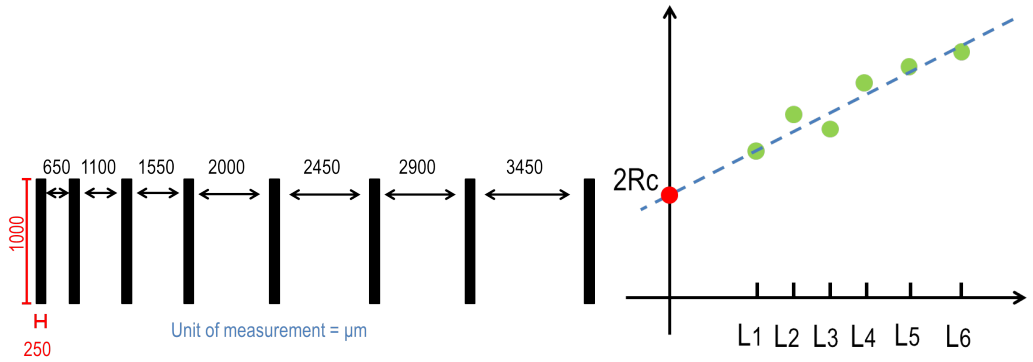

(a) **(b)**

Figure 3.5: (a) Schematic of the mask used for the deposition of the contacts needed for TLM measurement designed by dr. Yang G [11]. **(b)** Schematic of the mathematical method used for the calculation of the contact resistance

3.3.3. Scanning Electron Microscopy

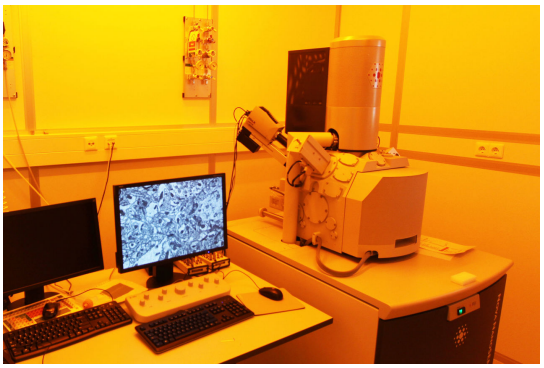

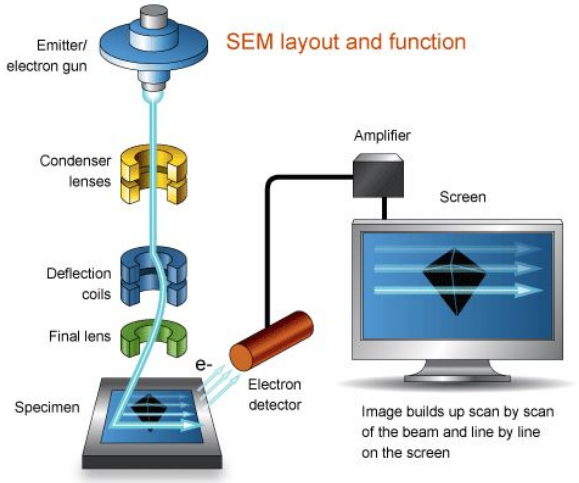

(a) **(b)**

Figure 3.6: (a) Nova Nanosem. **(b)** Schematic of the working principle of the SEM microscopy [31]

Scanning Electron Microscopy has been used for the inspection of the samples' surface and the evaluation of the designed features. *Nova NanoSEM 450* from FEI Company [32] has been used at Kavli Nanolab of the Applied Science faculty of TU Delft.

SEM images are made by scanning the inspected surface with a convergent electron beam. The electron beam is generated with an electron gun, which can be based on either thermoionic emission or field emission. The beam is then focused onto the specimen by electromagnetic lenses to maximize the efficiency. The generated image is the result of a point-by-point line-by-line scanning: the two pairs of electromagnetic coils are used to deflect the electron beam along the whole surface of the specimen. The first one deviates the electrons out of the optical axis of the microscope, while the second one bends them back onto the axis to the intended coordinates. An electron detector collects then the electrons, which are transformed into photons via a scintillator and amplified by a photomultiplier to generate the final image on the screen (figure 3.6b shows the components of a SEM microscope) [31]. Since the electron beam is very sensible to deflection by particles, the a

vacuum is generated in the inspection chamber [33].

When the beam-sample interaction occurs, the kinetic energy of the accelerated electrons is converted and dissipated, inducing the emission of X-rays, primary backscattered electrons, secondary electrons and Auger electrons. Primary backscattered electrons and secondary electrons are then captured by an electron recorder which converts the signal into three-dimensional images [33].

The primary backscattered electrons are high-energy electrons (>50 eV) that the sample emits back in response to the excitation as a result of the incident beam. They highlight the different material composition of the sample and give an indication of the average atomic number of the sample. Secondary electrons, on the other hand, are low energy electrons (<50 eV) due to inelastic scattering of the incident electrons [31]. Overall, therefore, scanning electron microscopy provides information not only on the external morphology of the specimen, but also on the chemical composition and the crystalline structure and orientation of the elements that constitute the sample [34].

One of the fundamental parameters that affects the generation of an image is the chosen acceleration voltage. Theoretically, a higher accelerating voltage leads to a higher signal and a lower noise in the final image. The interaction volume increases and the electron beam penetration would is higher, raising the number of backscattered electrons and allowing a deeper analysis of the morphology of the sample. However, an increase in accelerating voltage can may also lead to some drawbacks:

- it can lead to an image with lower surface details;
- in insulated samples, charging artefacts can build up, leading to the generation of not existent features;
- a higher voltage produces a more energetic beam that can result in increase heating, which can damage the sample.

Commonly, SEM microscopes are characterized by voltages ranging from 0 to 30 kV.

In addition to the normal operating mode, Nova Nanosem 450 allows the use of the microscope in immersion mode, by the use of a magnetic immersion lens. Immersion mode, permits magnification above 50000x, allowing to obtain detailed, high resolution images.

The whole system is computer-controlled in order to optimize the focus and the magnification of the taken images as well as to prevent damages of the microscope hardware.

3.3.4. Current density-voltage measurements (J-V curves)

Current density-voltage measurements are performed to characterize the solar cell performances and to measure the output power of the cell under Standard Test Conditions (STC) (Air Mass 1.5, solar spectrum equal to 1000 W/m^2 and temperature equal to 25°C). Measurements were performed using a Wacom WXS-90S-L2, class AAA, dual lamp solar simulator. The system is equipped with two different Halogen and Xenon lamps that are able to create conditions really close to STC. The whole system is calibrated using two mono-crystalline silicon reference cells which were manufactured at the Fraunhofer Institute for Solar Energy System. The measurement stage, moreover, is temperature controlled in order to avoid heating of the sample in response to the lamps irradiation.

In order to trace the J-V curve of the solar cell under analysis, a resistive DC load is varied sweeping the whole cell's voltage range, from zero to the V_{oc}. The P_{mpp}, the J_{mpp}, the V_{mpp} and the FF can then be measured to characterize the solar cell. The measured values are also elaborated by a connected software which draws the J-V curve and calculates the series and parallel resistance of the device.

4

Optimization of the front contact

This chapter is meant to answer the first research question introduced in chapter 1.2:

Is it possible to design a front contact grid to improve the charge carriers collection in a large area thin film solar cell?

As introduced in chapter 2, charge carrier lifetime is considerably shorter in thin film silicon alloys than in crystalline silicon because of the high defect density. Large area thin film modules are, therefore, characterized by multiple, narrow solar cells connected in series.

The series interconnection, however, generates thin film solar modules with a relatively high output voltage. As introduced in chapter 1.1, the reactions occurring in water treatment applications need a constant operational voltage lower than 2 V. The most simple and straightforward approach, for the development of a large area thin film solar cell with this voltage level, is the design of a front contact grid able to minimize the power losses and the negative effects commonly occurring during the upscaling processes.

This chapter is structured in three main different parts. At first, the Matlab code written and developed by a former TU Delft student, Georgios Papakonstantinou [35], is presented and explained. An analysis of the inputs is then carried out. Lastly, the optimization process for the actual design of the front contact grid is shown.

4.1. Introduction to the Matlab code

The losses introduced by the addition of the metallization pattern on top of a solar cell can be divided in two main groups: *optical losses* and *electrical losses*. The Matlab optimization tool loops continuously and calculates the sum of the two components for different possible designs: the optimal condition is the minimum value found.

The introduction of a front grid on top of the solar cell, shadows part of the total surface, preventing a fraction of the incident light from being absorbed. Therefore, to calculate the fraction of optical losses (p_s) the area of the metal grid is divided by the total area of the solar cell, resulting in the following equivalence:

$$p_s = \frac{W_f l_f + D W_b}{2 n_f D^2} \tag{4.1}$$

in which W_f is the width of the finger, l_f is the length of the finger, D is the half finger pitch, W_b is the busbar width and n_f is the number of fingers. Compare Figure 4.1 for a graphical illustration of these parameters.

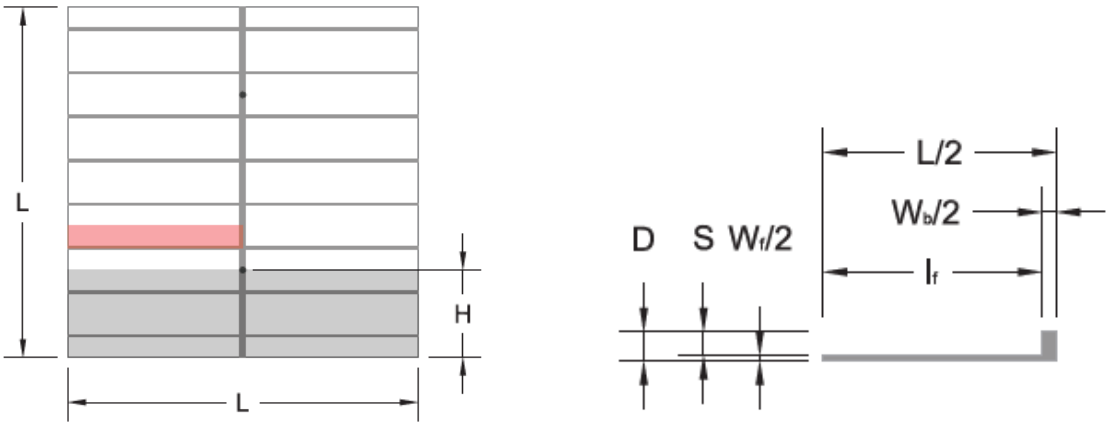

(a) **(b)**

Figure 4.1: (a) Schematic of a front contact grid, in which L corresponds to the side length of the solar cell, H to the half current extraction distance and the black dots to the current extraction points. **(b)** shows the characteristic dimensions of the elementary geometry used for the metallic pattern optimization. Figures retrieved from [35]

Electrical losses, on the other hand, are due to the series resistance of several components: the resistance of the ITO front layer, the resistance due to the flow of electricity in the fingers and in the busbars and the contact resistance generated at the metal-semiconductor interface. Figure 4.2 shows a schematic overview of the aforementioned losses.

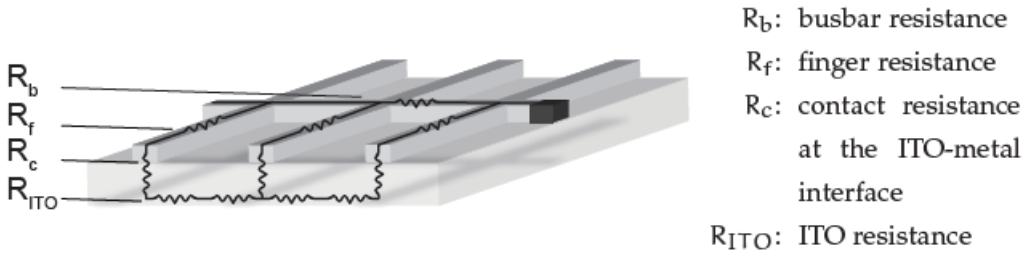

Figure 4.2: Schematic of the cross section of the top part of the solar cell with a simplified illustration of all the added losses

Therefore, the total fractional sum of electrical losses p_{el} is equal to

$$p_{el} = \frac{J_{mpa}}{V_{mpa}} R_T (1 - p_s)^2 A_T \tag{4.2}$$

in which J_{mpa} and V_{mpa} are respectively the current density and the voltage at maximum power point of an ideal lossless solar cell while R_T is the total electrical resistances introduced by the front mask.

Therefore, the total fractional losses p_t, which are the objective function of the minimization process, are equal to:

$$p_T = 1 - \frac{P_{mpp}}{P_{mpa}} = p_s + p_{el} \tag{4.3}$$

To study the optimal design of the front contact grid of the thin film solar cell, inputs are varied in order to find the right combination of busbars and fingers that minimizes the induced losses [35].

The inputs of the Matlab code are:

- number of busbars
- dimension of the solar cell edge
- sheet resistance of the TCO layer
- sheet resistance of the metal front contact
- J_{sc} and V_{oc} of the considered solar cell technology

The outputs obtained from the optimization process describe the geometry of the grid and are:

- number of fingers
- fingers width
- busbars width
- number of extraction points, which is the number of soldering points between the busbar and additional metallic strips. These points are used to extract the current
- finger spacing
- total power losses

4.2. Analysis of the inputs

The simulations for the optimization process require some experimental data for input. To that end some materials are deposited and measured at the EKL laboratory.

First, sheet resistance of the available TCOs is measured. As introduced in chapter 3.1.1, ITO and AZO can be deposited by magnetron sputtering deposition. Additionally, at TU Delft, already textured glasses with FTO on top from Asahi Glass Company [36] are available for the deposition of solar cells in superstrate configuration. Different layers with different thicknesses for each TCO technology are deposited, with the exception of the FTO whose properties are already fixed by the company. The deposition parameters for AZO and ITO are shown in table 4.1.

Table 4.1: Deposition parameters for AZO and ITO

	Power (W)	Temperature (°C)	Pressure (mbar)	Argon flow (sccm)
ITO	200	485	1.20e-02	40
AZO	400	400	2.50e-05	20

AZO is deposited with thicknesses ranging from 100 nm to 700 nm, while ITO from 75 nm to 95 nm: the thickness range is chosen considering the previously acquired knowledge at the faculty. From the taken measurement, similar trends are recognized: by increasing the thickness of the TCO, the sheet resistance decreases following an hyperbolic trend. For AZO thicknesses in the range between

400 nm and 700 nm, the improvement in sheet resistance starts to become less significant and values begin to stabilize (Fig. 4.3a). In the case of ITO, a further decrease of the layer thickness results in unstable depositions that do not provide any significant result. Although fewer samples are considered than for AZO and the two previously described trends are not fully defined, comparing the results obtained from the three dimensions measured to other studies found in literature ([37],[38]), similar considerations seem to be reasonable: the curve, indeed, flattens and the difference between two consecutive thickness values decreases (Fig.4.3b).

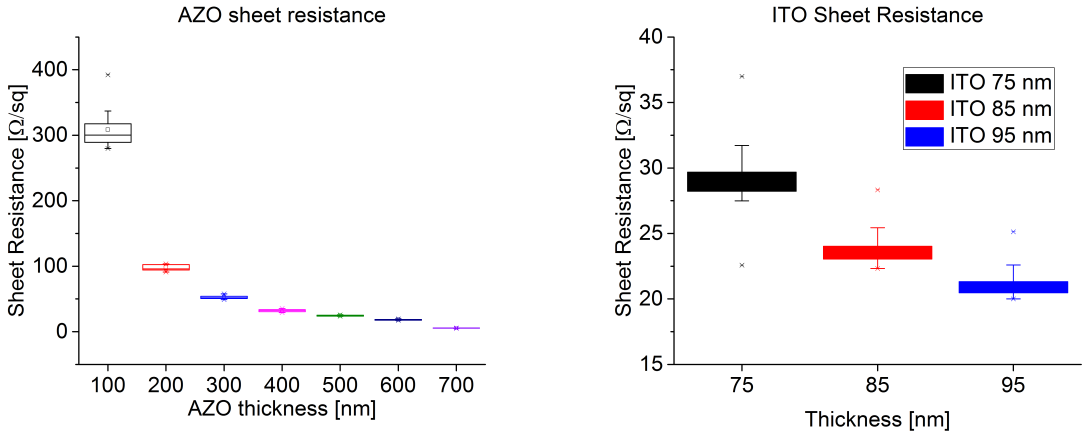

(a) **(b)**

Figure 4.3: **(a)** Sheet resistance values for different AZO thicknesses. **(b)** Sheet resistance values for different ITO thicknesses. Measurements carried out with the 4 probes measurement technique.

The two graphs in figure 4.3, in particular figure 4.3a, show also that, together with the decrease in sheet resistance, a reduction of thickness also generates layers in which the thickness is less uniform. Since only one thickness value can be used input for the simulation, an average value is taken and layers are assumed to be perfectly homogeneous. Hence, inputs with high fluctuations are undesired, since they can lead to imprecise and not realistic results.

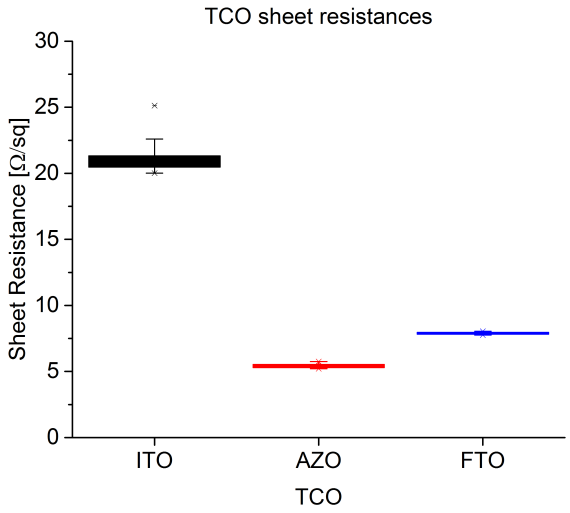

Figure 4.4: Comparison among the sheet resistances for different layers with 100 nm ITO, 700 nm AZO and of FTO of Asahi company

Figure 4.4 shows the lowest measured sheet resistance values for each of the TCO's. These were obtained at 100 nm ITO, 700 nm AZO and FTO. For the available recipes at the time, AZO guarantees the best sheet resistance achievable. FTO, on the other hand, gives better properties of homogeneity even though it has a slightly higher resistance. Finally, from the carried out experiments, ITO is the worst performing TCO material.

As aforementioned, the deposition of a metal grid on top of a semiconductor introduces losses at the metal-semiconductor interface. Therefore, another fundamental parameter to be studied is the contact resistance between the aluminum, that is the evaporated material used for the front grid, and the TCO layers. In order to have a complete overview of the possible mask designs, 500 nm of Al, with the design shown in figure 3.5a to carry out the TLM measurement method, has been deposited on top of the following semiconductor layers: 500 nm AZO, 600 nm AZO, 700 nm AZO, 75 nm ITO, 85 nm ITO, 100 nm ITO and FTO.

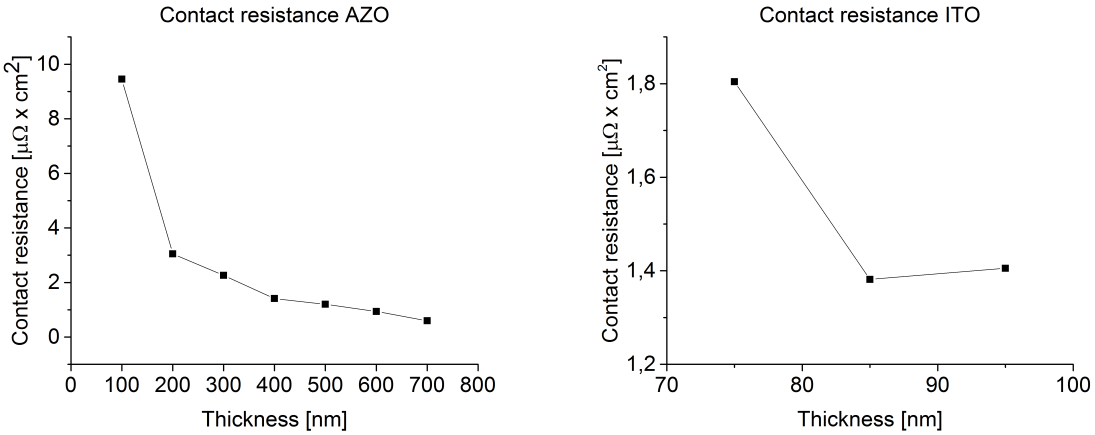

Figure 4.5: **(a)**Sheet resistance values for different AZO thicknesses. **(b)**Sheet resistance values for different ITO thicknesses. Measurements carried out with the TLM method

Just like the sheet resistance, the contact resistance strongly depends on the thickness of the semiconductor layers and follows a similar hyperbolic trend: thick layers lead to lower contact resistances. Above 500 nm, the curve starts to take a constant value. Figure 4.5b does not show a well defined trend. Similar to the sheet resistance analysis, this is mainly due to the small variation in thickness that can be deposited.

Lastly, different thin film solar cell technologies are analyzed varying J_{sc} and V_{oc} considering optimized values for different solar cells technologies: amorphous silicon (a-Si:H), nano-crystalline silicon (nc-Si:H), tandem amorphous silicon (a-Si:H/a-Si:H) and tandem amorphous silicon and nanocrystalline silicon (a-Si:H/nc-Si:H).

Table 4.2 shows the values used during the simulations.

Table 4.2: Values of J_{sc}, V_{oc} and FF used in the simulations for the optimization process

	a-Si:H [39]	nc-Si:H [39]	a-Si:H/nc-Si:H [39]	a-Si:H/a-Si:H [7]
Jsc [mA/cm^2]	14.8	32.9	16.45	5.64
Voc [V]	0.883	0.552	1.453	1.67
FF [%]	0.718	0.77	0.77	0.77

4.3. Optimization of the front contact grid

The optimization process is carried out by varying the number of busbars, from 1 to 8, the length of the side of the solar cell, from 6.5 cm to 9.5 cm with 1 cm step increase, the TCO type, and the type of solar cell. For a complete overview of the possible front grid designs and for the analysis of the variation in performances with respect to some fluctuations during the measurements, not only the best performing thickness for each TCO is taken into account: AZO layers, indeed, are varied from 500 nm to 700 nm and ITO from 75 nm to 95 nm. For the sake of simplicity, only the optimization process for a-Si:H with 700 nm AZO is shown in this section. Conclusions and results are anyhow valid also for ITO, for which the variation of inputs leads to similar trends. It must be mentioned, moreover, that for each of the configurations analyzed the Matlab code also optimizes the dimension of the fingers and of the busbars which are not constant.

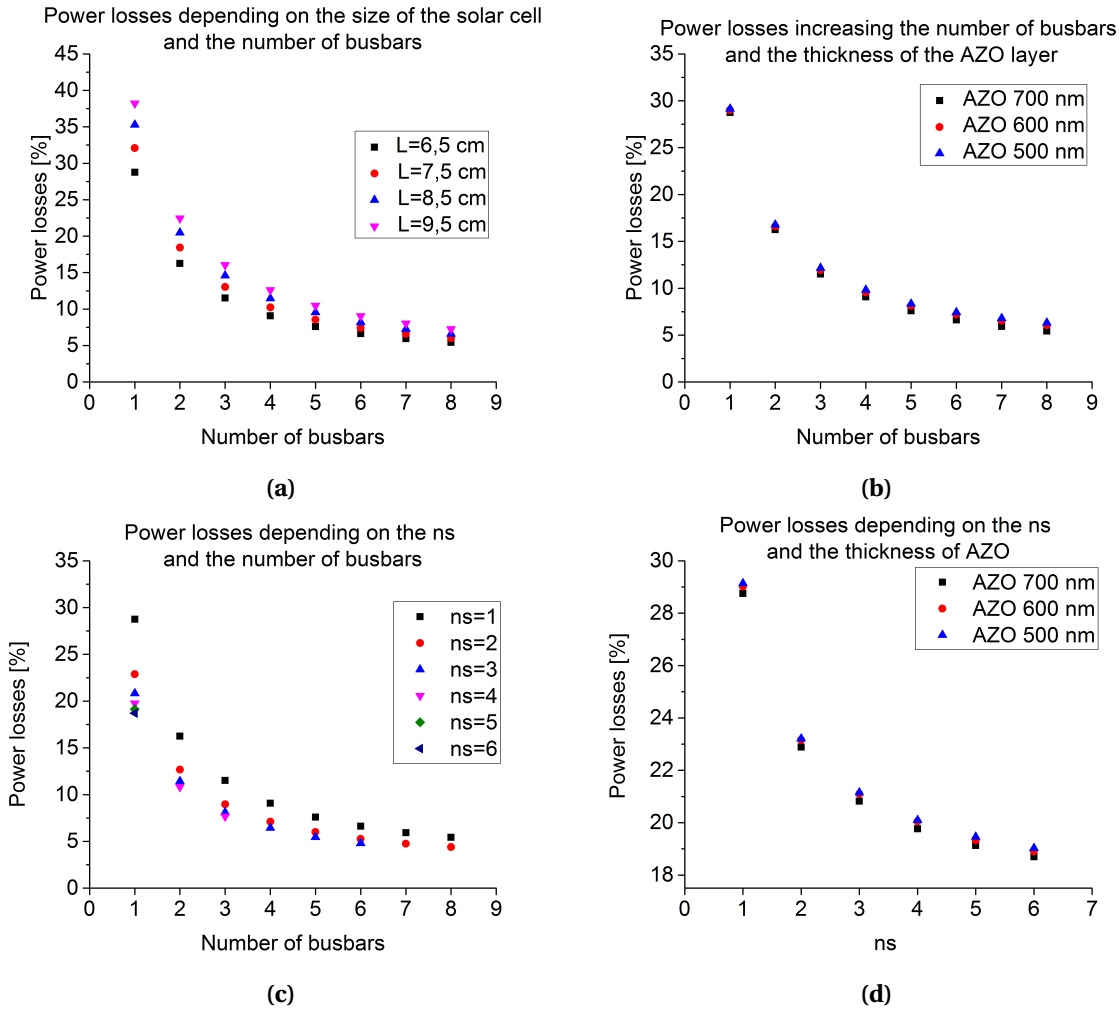

Figure 4.6: Total fractional power losses analyzed by varying the inputs. Figure **(a)**: increase of the number of busbars and of the length of the side. The AZO layer is 700 nm thick and the number of extraction point is 1. Figure **(b)**: increase of the number of busbars and of the thickness of the AZO layer. The side of the solar cell is 6.5 cm long and the number of extraction point is 1. Figure **(c)**: increase of the number of busbars and of the number of extraction points. The AZO layer is 700 nm thick and the side of the solar cell is 6.5 cm long. Figure **(d)**: increase of the number of extraction points and of the thickness of the AZO layer. Only one busbar is considered and the side of the solar cell is 6.5 cm long.

Figure 4.6 shows decreasing hyperbolic trends while increasing the number of busbars or the number of extraction points, which are all similar to each other. Unexpectedly a minimum value, that is, the optimal design of the front grid, can not be found considering only the performance losses. A change in thickness of the AZO layer (Figg. 4.6b and 4.6d), moreover, does not introduce relevant added losses to the total fractional ones. This shows that the majority of the introduced electrical losses are not due to the flow of charge carriers in the TCO layer but to the current flowing in the aluminum layers of the front contact. This is clearly shown also in figure 4.6c: while decreasing the number of busbars and of current extraction points, indeed, the power losses increase significantly. Current is extracted in less points throughout the front contact grid its value increases significantly due to the continuous adding up of current collected by the fingers.

Considering the geometrical properties, finger and busbar width and finger length, optimized by the code for the different analyzed combination of inputs, hyperbolic trends are clearly visible when increasing the number of busbars. Figures 4.7a and 4.7b show two interesting relationships. The number of fingers (black labelled numbers in figure 4.7a) does not depend on the number of busbars; except for the design with one single busbar in which only 9 fingers are needed, in the remaining designs analyzed 10 fingers per busbar are always the optimum number. Although the number of fingers per busbar does not change with the increase of the number of busbars, the total covered area continuously decreases due to the reduction of fingers and busbars width.

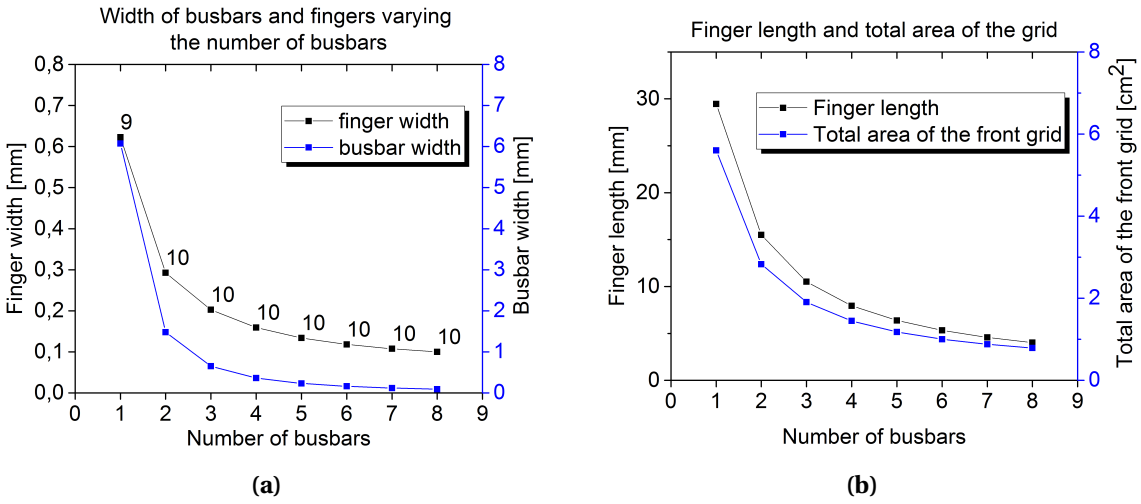

Figure 4.7: (a) Busbars and fingers width obtained by varying the number of busbars. The black labelled numbers on top of the finger width data show the number of fingers designed by the Matlab code. **(b)** Fingers length and total area the front grid obtained by varying the number of busbars.

Figure 4.8a illustrates a simplified schematic of a solar cell with a 2 busbars front grid: area **A** corresponds to the charge collection area of each finger, which theoretically corresponds to half of the space between two consecutive fingers. A complex and dense front grid with a high number of busbars and of fingers, together with a considerably high number of extraction points, results in the best possible configuration with the lowest possible losses. Ideally, a front grid with an infinite number of busbars and fingers of infinitesimal dimension, and an infinite number of extraction points, would result in the optimal configuration to minimize the losses. Indeed, the higher the number of extraction points, the lower the induced electrical losses, as a result of the minimization of the *current path* through the metallic contact. An ideal design with an infinite number of extraction points would lead to the immediate extraction of each and every charge carrier as soon as it reaches the contact, practically reducing the losses to zero. An infinite number of fingers, on the other hand,

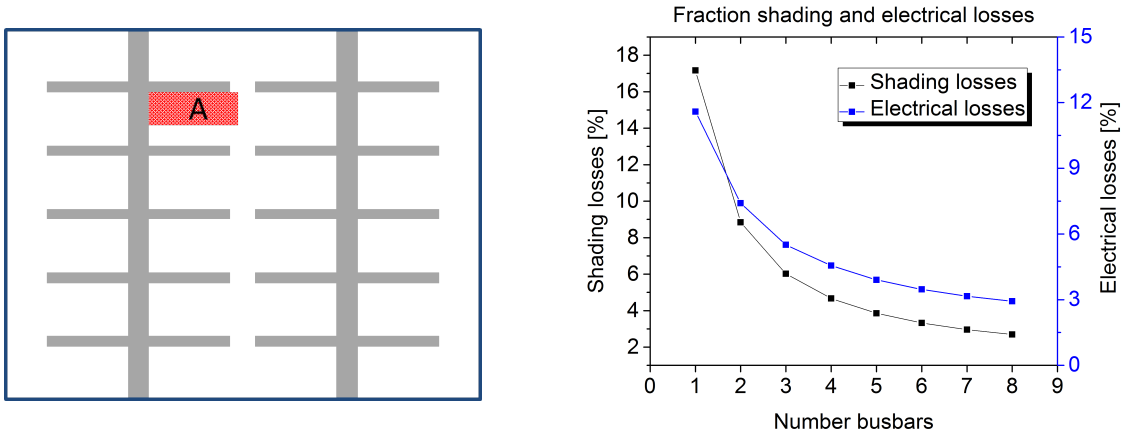

(a) **(b)**

Figure 4.8: (a) Schematic of a front grid design with two busbars. Area **A** shows the area delimited by one finger and half of the finger spacing. **(b)** Electrical and shading fractional losses depending on the number of busbars

would significantly reduce the electrical losses in the TCO: the relevant dimension the charge carriers have to cross laterally is reduced approximately to zero, and only the transverse resistance due to the thickness of the TCO is influential.

Lastly, in figure 4.9 power losses show a linear increasing trend when incrementally increasing the length of the side of the solar cell, both for varying the AZO layer thickness (Fig. 4.9a) and varying the number of extraction points (Fig. 4.9b). However, it has to be considered that the Matlab code considers perfectly homogeneous layers and does not take into account that during real depositions there are high chance of creating defects and shunts that highly change the performances of the solar cell.

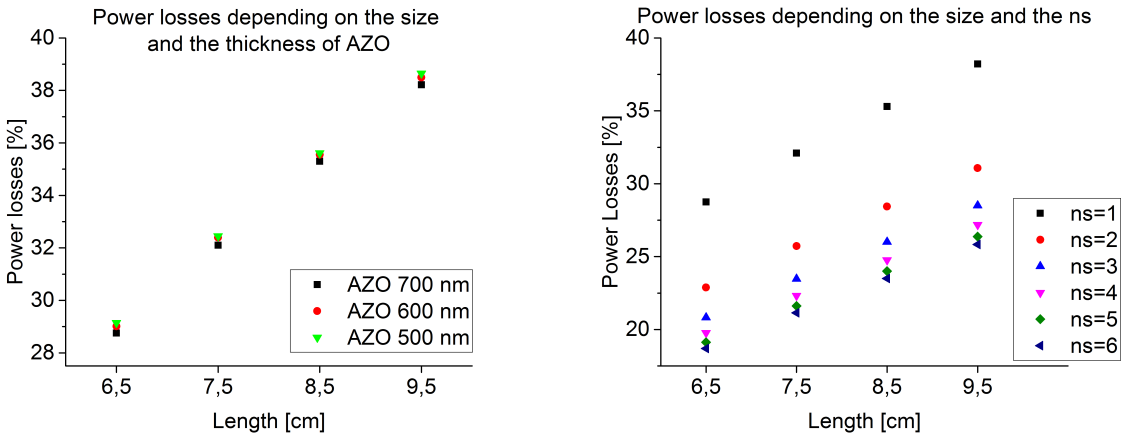

(a) **(b)**

Figure 4.9: (a) Fractional power losses obtained by varying the side of the solar cell and the thickness of the AZO layer. **(b)** Fractional power losses obtained by varying the side of the solar cell and the number of extraction points. Geometrical dimensions of the front grid are optimized for each of the configurations analyzed.

4.3.1. Variation of the TCO type and the solar cell technology

The second part of the optimization process consists of repeating of all the steps introduced in the previous part of the chapter, but now for different types of TCO and of solar cell technology. Similar trends to the ones already illustrated are found for all the combinations of settings. As a consequence, therefore, only the final results are shown and compared. Results, moreover, are based only on two different dimensions: 6.5 cm, which corresponds to the size of the silicon wafers used at the EKL laboratory, and 9.5 cm, which is the biggest possible dimension at the faculty in case of glass substrates.

The main conclusion that can be drawn from the simulation process is the absence of an optimal design when evaluating only the reduction power loss. Therefore, mechanical and technological limits are considered as boundary conditions for the choice of the optimal front grid design. Two main limitations are set:

- busbar width has to be thicker than the finger width. While increasing the number of busbars and of extraction points, the Matlab code continuously decreases the busbars thickness, reaching a point when fingers becomes wider than the busbars. This highly depends on the number of extraction points. For for the final purpose of this thesis, the application of a solar cell in a water treatment device, n_s does not represent a limit and it is chosen based on the optimal design.
- metal evaporation is also limited by the minimum possible thickness that can be deposited. For dimensions lower than 0.2 mm, the evaporated aluminum can clog the mask holes preventing the deposition onto the superstrate.

With everything taken into account, the optimal front mask designs are shown in table 4.3 for different solar cell technologies.

Table 4.3: Optimized values for the front grid design in case of 700 nm of AZO and varying the type of solar cell technology

Type	a-Si		nc-Si		a-Si:H/nc-Si:H		a-Si:H/a-Si:H	
TCO [nm]	AZO 700	AZO 700	AZO 700	AZO 700	AZO 700	AZO 700	AZO 700	AZO 700
L[cm]	6.5	9.5	6.5	9.5	6.5	9.5	6.5	9.5
W_f [mm]	0.202	0.268	0.222	0.248	0.277	0.205	0.227	0.243
W_b [mm]	0.217	0.392	0.241	0.343	0.314	0.211	0.337	0.320
l_f [mm]	10.725	11.679	8.005	7.745	16.093	9.394	16.081	15.673
nf_L	10	12	14	18	9	11	6	8
nt_L	3	4	4	6	2	5	2	3
P_t [%]	8.11	9.86	12.13	13.25	9.32	7.05	6.20	6.10

L is the length of the solar cell side, W_f is the width of the finger, W_b is the busbar width, l_f is the finger length, nf_L is the total number of fingers, nt_L is the total number of busbars and P_t is the total fractional power loss. Common designs can not be found probably because of the high difference in current and voltage among the technologies chosen: it has been decided, therefore, to focus the deposition of the solar cells on the a-Si:H/a-Si:H solar cell, which was designed for the degradation of phenol in the water treatment device in a previous master student thesis [7].

The last step to design the optimal grid for a a-Si:H/a-Si:H solar cell is the choice of the TCO. Table 4.4 shows the results of the optimization process that has been carried out.

The use of AZO or FTO as TCO leads to similar final design, with the same number of busbars and comparable total fractional losses. FTO, however, is already deposited on the textured glasses from

Table 4.4: Optimized values for the front grid design in case of a-Si:H/a-Si:H solar cell obtained by varying the type of TCO

Type	a-Si:H/a-Si:H		a-Si:H/a-Si:H		a-Si:H/a-Si:H	
ITO [nm]	AZO 700	AZO 700	ITO 95	ITO 95	FTO	FTO
L[cm]	6.5	9.5	6.5	9.5	6.5	9.5
W_f [mm]	0.227	0.243	0.300	0.244	0.196	0.217
W_b [mm]	0.337	0.320	0.689	0.364	0.225	0.320
l_f [mm]	16.081	15.673	32.155	23.568	16.137	15.673
nf_L	6	8	9	12	7	9
nt_L	2	3	1	2	2	3
P_t [%]	6.20	6.10	10.07	7.73	5.61	6.15

Asahi company: this leads to a easier reproducibility and ease the deposition process. The most suitable design considering the facilities of TU Delft and the scope of the thesis is, therefore, a-Si:H/a-Si:H solar cells on FTO. Figure 4.10 shows the final design used for the production of the masks. It has to be highlighted that the length of the fingers has been slightly reduced to guarantee enough robustness to the masks.

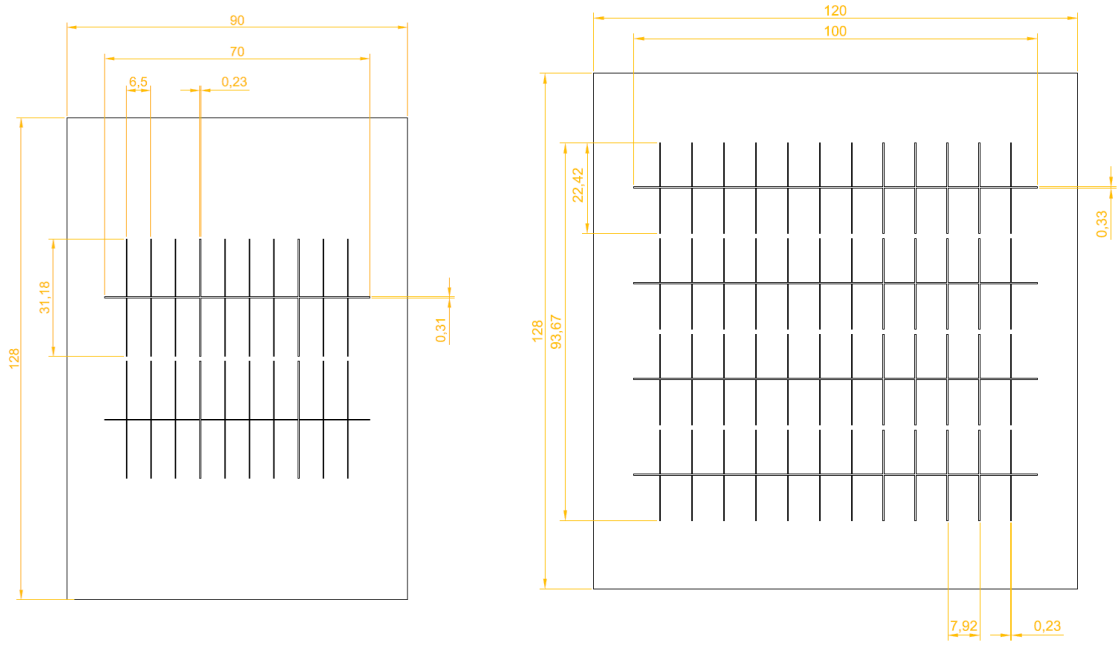

(a) **(b)**

Figure 4.10: **(a)** Mask design for a-Si:H/a-Si:H solar cell deposited on FTO with a side length of 6.5 cm. **(b)** Mask design for a-Si:H/a-Si:H solar cell deposited on FTO with a side length of 9.5 cm

4.4. Conclusions

In order to minimize the power losses on large area thin film solar cells, a front contact grid has been designed through simulations of the optical and electrical power losses. Different masks have been analyzed by varying the number of busbars, the type of TCO, the solar cell technology and the dimensions of the solar cell. Unexpectedly, an optimal design with respect to the total fractional losses could not be found: a progressive increase of the number of busbars and fingers, together with the decrease of their width, continuously reduces the performance losses and enhance the charge carrier collection. Ideally, a front grid with infinite busbars and fingers with infinitesimal length would reduce the total power loss to approximately zero. Technical and mechanical constraints, therefore, have been considered as boundary conditions for the final mask design. Taking also into account the facilities of the faculty, an optimized mask for a-Si:H/a-Si:H solar cells deposited on samples of 6.5 and 9.5 cm with FTO as TCO has been produced. The homogeneity of the depositions played a fundamental role in the choice of the TCO type: FTO, indeed, guarantees more uniform layers, a characteristic that is important both to guarantee reliable results from the simulations and from the depositions of the solar cells.

5

Laser scriber optimization

In this chapter a deep analysis of the laser scribing technique is carried out, in order to answer the second research question introduced in chapter 1.2

What are the optimal parameters for the isolation of a solar cell by laser scribing and what are the major drawbacks of using a single wavelength infrared laser scriber?

Experiments are carried out to analyze the ablation of the photoactive layer both for pin and nip solar cells respectively.

The research is divided into two parts, which also correspond to the two main subchapters of this paragraph. At first, a visual optimization is carried out: the trends resulting from the variation of the laser parameters are analyzed. Then, the lines scribed with the previously optimized settings are analyzed with a scanning electron microscope (SEM). In the last part of the chapter the main conclusions are summarized and illustrated.

In this chapter several parameters are mentioned and varied. For the sake of simplicity the parameters are here introduced and explained. Two categories are distinguished:

- **Parameters that can be manually controlled**
  - Pulse repetition frequency (f_{laser}), which is the number of pulses emitted per second
  - Pulse width (Q_p), which is the duration of a single pulse
  - Percentage of the laser average output power ($P_{\%}$)
  - Speed of the laser (v_{scan})
  - The number of marking loops (Mark-loops), which is the number of times the laser repeats the same pattern
- **Parameters that are calculated** (see par. 2.5.1)
  - Pulse overlapping rate ($O_{percentage}$)
  - Average laser fluence (ϕ)
  - Pulse peak power (P_{peak})
  - Average output power in the first region of the laser curve (P_{out}) (see Fig.5.3)

5.1. Visual optimization

The optimization process in case of pin superstrate or nip substrate solar cells are similar: in both cases the laser impinges on the silicon side, that is, the n-doped layer in the first case and the p-doped layer in the latter, allowing the evaporation of the ablated material.

Therefore, in pin configuration the deposited layers are removed in the following order: n-SiOx:H, i-a-Si:H and p-SiOx:H (Fig. 5.1a). The front metal contact deposited in between the glass and the p-layer have to remain intact to guarantee the extraction of charge carriers. Therefore, the goal of the optimization process is to find the correct parameters that allow the removal of the photoactive stack leaving the metal untouched. Experiments are carried out on a solar cell with front Aluminum contact 500 nm thick. A full contact is deposited to have the opportunity to carry out on the same sample more than one experiment and obtain a complete analysis of the change in ablating performances.

In nip configuration, instead, the silicon layers are removed in the opposite order: p-SiOx:H, i-a-Si:H and n-SiOx:H (Fig. 5.1b). The material must be removed up to the full back metal contact, that has to remain undamaged in order to guarantee the electrical connection at the back.

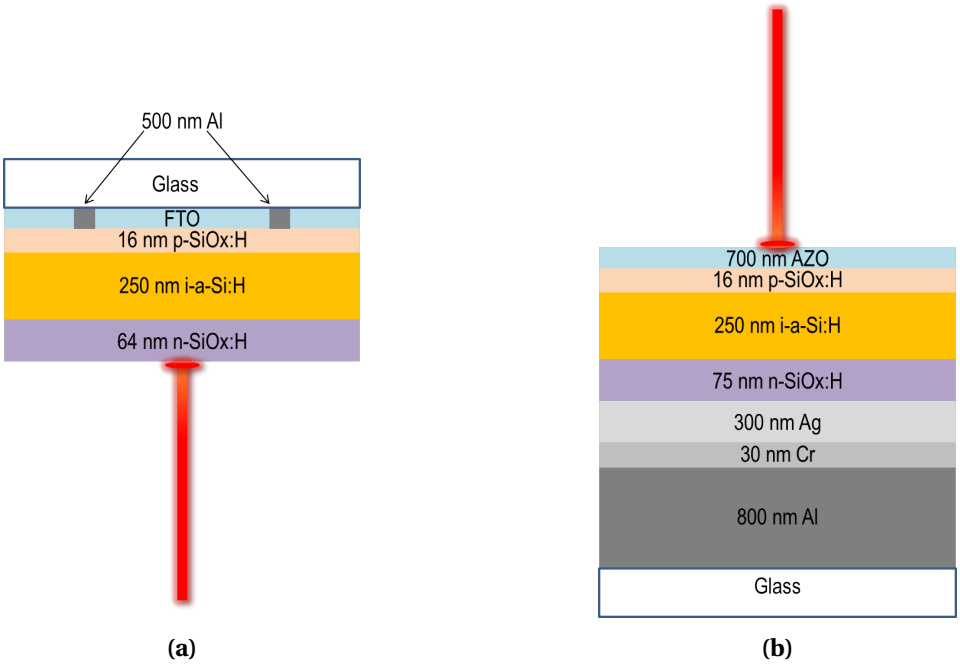

Figure 5.1: Laser impinging orientation depending on the solar cell configuration. **(a)** pin solar cell. Silicon layers are removed in the following order: n-SiOx:H, i-a-SiOx:H and p-SiOx:H. **(b)** nip solar cell. p-SiOx:H, i-a-SiOx:H and n-SiOx:H is the order of layers removal.

Although the aim of the laser ablation process is to scribe thin and sharp lines on the solar cells, squares are used during the visual optimization analysis in order to have a better understanding of the influence of each of the parameters. Effects due to the variation of the frequency of the pulses, of the average output power, of the length of the pulse and of the velocity of the laser are analyzed and illustrated in detail. Electrical conductivity is measured, for a select few squares, in order to verify both the complete removal of the silicon layers and the presence of the back metal contact.

5.1.1. Variation of the system frequency and of the average output power

In the first part of the optimization process the performance of the laser is analyzed as a function of the pulse repetition frequency (f_{laser}) and the percentage of the laser average output power ($P_{\%}$).

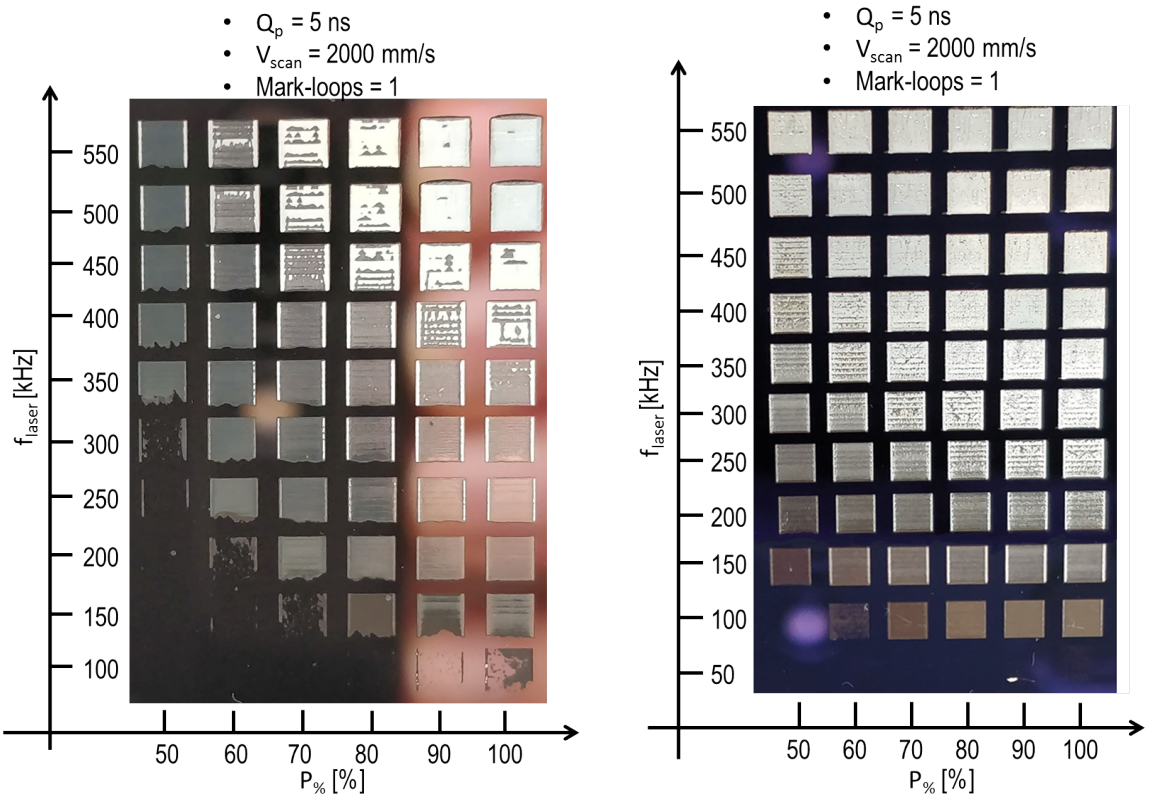

Figure 5.2: Pictures of the ablated squares varying frequency and average power of the laser pulse for **(a)** the nip solar cell and **(b)** the pin solar cell. The remaining parameters are kept constant: the pulse width (Q_p) is equal to 5 ns, the laser velocity (v_{scan}) is constant at 2000mm/s and only one marking loop (Mark-loops is performed

Figure 5.2 shows similar trends both for nip and pin configuration. The white squares on the top right side of both the cells indicates the complete removal of all the deposited layers, that are both the photoactive stack and the metal deposited on the back. By reducing $P_{\%}$ the metal removal progressively reduces and only the photoactive stack evaporates. The same happens when f_{laser} is reduced, even for fixed values of power. For really low values of f_{laser} and $P_{\%}$ the laser does not manage to remove the photoactive stack. It can also be noted that, with the decreasing of f_{laser}, the material appears less homogeneous.

The average laser fluence (ϕ) and pulse overlapping rate ($O_{percentage}$) (see par.2.5.1) are then computed, in order to perform a quantitative analysis of the effect of the two parameters during the ablation process. Before introducing these values, however, a further characteristic of the used laser has to be explained. The laser used in the faculty, indeed, is characterized by two working regions depending on f_{laser} and on the pulse width (Q_p). For every Q_p, a cut-off frequency ($f_{cut\text{-}off}$) exists: below $f_{cut\text{-}off}$, the average power output of the laser (P_{out}) is linearly reduced. On the other hand, above $f_{cut\text{-}off}$ the laser works at a constant average power (Fig.5.3).

Therefore, P_{out} below $f_{cut\text{-}off}$ can be calculated as follow (eq. 5.1):

$$P_{out} = \frac{P_{avg}}{f_{cut\text{-}off}} \times f_{laser} \tag{5.1}$$

in which P_{avg} corresponds to the average power of the laser above $f_{cut\text{-}off}$, namely 31 W.

Combining equation 5.1 and equation 2.9, it results that the average output energy delivered by every single pulse is constant and equal to $P_{avg}/f_{cut\text{-}off}$ in the first region of the curve (red area in Fig.5.3) at a fixed Q_p. Therefore ϕ (assuming almost constant the area on which a single pulse is incident, which has a radius of almost 130μm) varies only changing $P_{\%}$ (Fig.5.4a).

Values of ϕ and $O_{percentage}$ are calculated and shown in figure 5.4. Conclusion and results are valid for both pin and nip configuration.

The amount of energy sent in each pulse plays a fundamental role in the ablation process: while decreasing $P_{\%}$ (that is, while moving from the left of the graphs in figure 5.2b to the right), the amount of ablated material reduces. The energy transmitted to the surface becomes gradually insufficient to remove all the deposited material. Moreover, the ablation process is strongly related to $O_{percentage}$: whith decreasing f_{laser}, indeed, even for the same ϕ (that is, while moving vertically in figure 5.2), the quantity of removed material changes significantly. This is mainly due to the fact that at high f_{laser}, that corresponds to high $O_{percentage}$, after each pulse the material does not have enough time to cool down before absorbing the energy delivered by the subsequent pulse. Therefore, the material is still in a molten state when receiving the following pulse, significantly increasing the possibility of material evaporating.

Based on these results, f_{laser} equal to 200 kHz for nip and 100/150 kHz for pin, seem to be optimal and will be used in the following optimization.

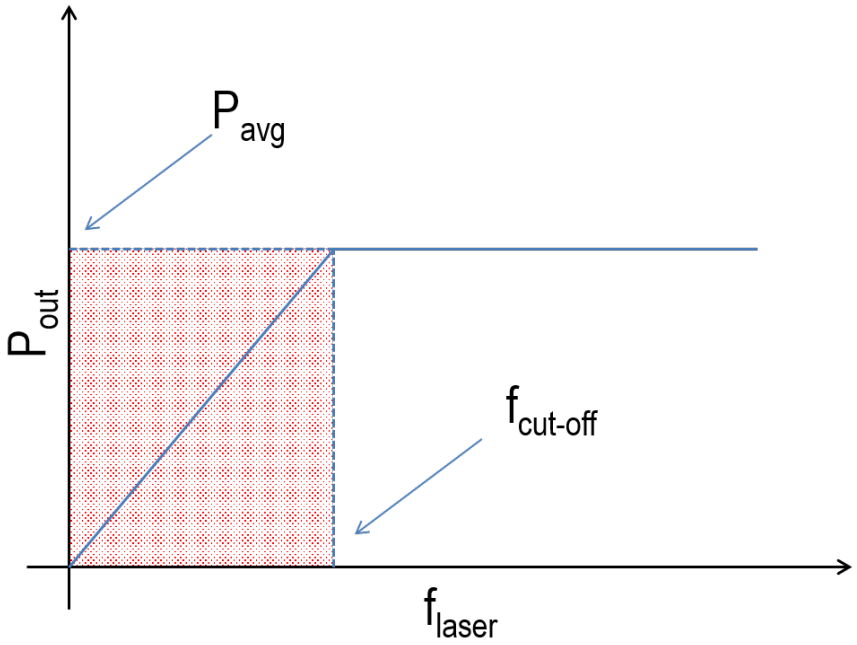

Figure 5.3: Schematic of the laser power output depending on the frequency. The red area corresponds to the working region that has been explored.

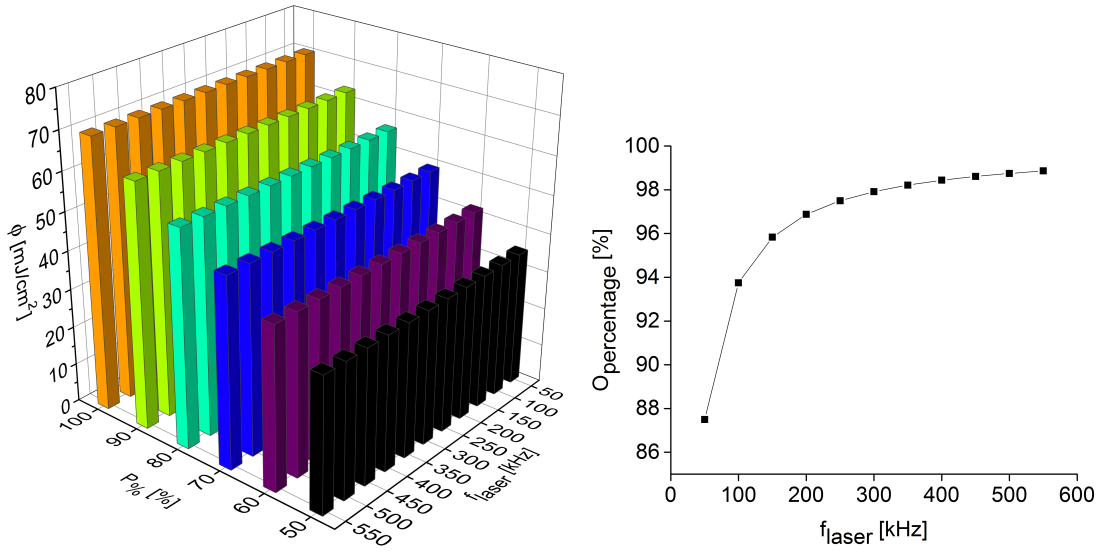

(a) **(b)**

Figure 5.4: **(a)** Laser fluence as a function of f_{laser} and $P_{\%}$. **(b)** Percentage of pulse overlapping by varying f_{laser} and the percentage of input power. The remaining laser settings are kept constant: v_{scan} is equal to 2000 mm/s and Q_p is equal to 5 ns. Values at 50 kHz are valid even though they are not shown in figure 5.2a.

5.1.2. Variation of the laser pulse width

In the second part of the optimization we investigate the influence of the pulse width (Q_p) and of the percentage of the laser average output power ($P_{\%}$). The other parameters are kept constant at the values optimized in section 5.1.1.

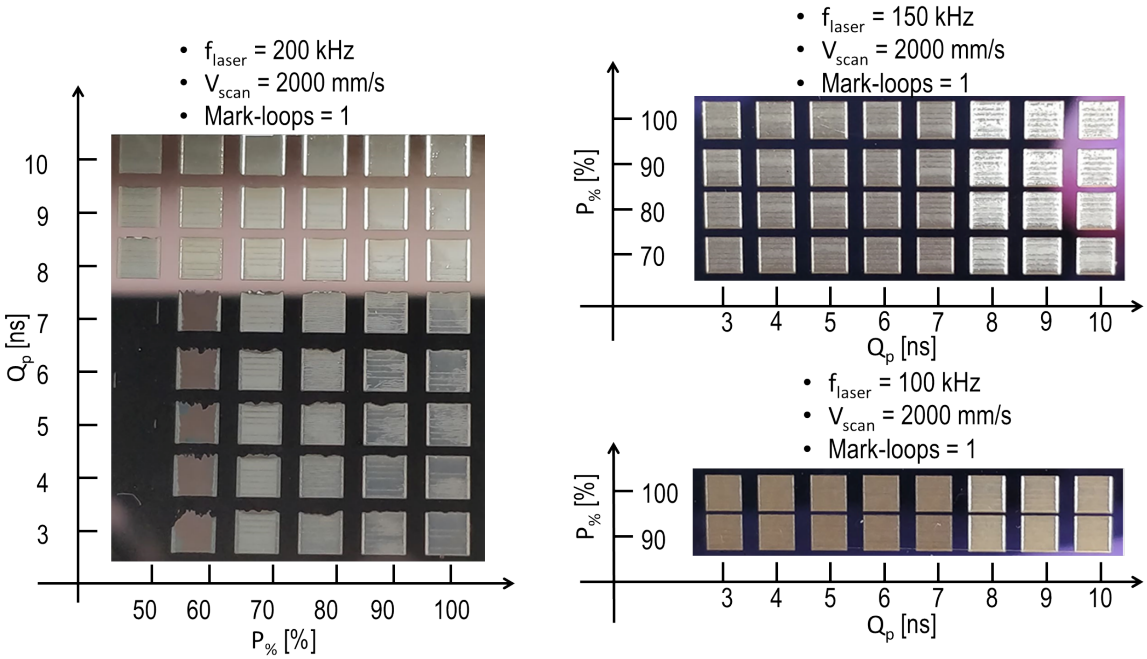

(a) **(b)**

Figure 5.5: Pictures of the ablated squares varying pulse width and average power of the laser pulse for **(a)** the nip solar cell and **(b)** the pin solar cell. The remaining parameters are kept constant depending on the type of solar cell. The pulse repetition frequency (f_{laser}) is equal to 200 kHz for nip, to 150 kHz for the top graph of pin and to 100 kHz for the bottom graph of pin. The laser velocity (v_{scan}) is constant at 2000mm/s and only one marking loop is performed for all the graphs.

Unlike the analysis carried out in section 5.1.1, the laser fluence (ϕ) is not only affected by the decrease of $P_{\%}$, but also by the fact that by varying Q_p the curve shown in figure 5.3 changes, hence the average output power (P_{out}). Figure 5.6 shows qualitatively how the pulse width influences the P_{out}: for a fixed frequency below the cut off frequency, the larger Q_p, the higher the average output power P_{out}. The variation in Q_p, assuming a rectangular pulse shape, also generates a considerable variation in the pulse peak power (P_{peak}). The ablating process, therefore, is driven both by the variation in ϕ and P_{peak}, since the pulse overlapping rate ($O_{percentage}$) is constant. Assuming that $f_{cut\text{-}off}$ varies with Q_p following equation A.1, it is possible to calculate the ϕ and the P_{peak} for every combination of settings. Figure 5.7 shows the obtained results.

Comparing the computed values to the experimental results, the energy delivered per unit area ϕ is the most dominant parameter for material ablation, while the peak power per pulse achievable P_{peak} has a secondary role. The square where the highest amount of material is removed, indeed, corresponds to the settings that lead to the highest fluency. These settings are 100% $P_{\%}$ and 10 ns pulse. The increase in P_{peak} due to the reduction in pulse width, on the other hand, is not enough to allow a change in the way the material is removed. A reduction of Q_p to fs, for instance, would have

changed the dominant phenomenon from melting to sublimation (see par.2.5.1). In the case of the sample analyzed, Q_p decreases only from 10 ns to 3 ns: the power to reach the sublimation of the material is not achieved, and melting remains the dominant phenomenon. Short pulses lead only to smaller heat affected zone (HAZ), which hinders the material removal.

In pin configuration (Fig. 5.5b), two different values of f_{laser} are tested. Results obtained at 150 kHz show less homogeneous squares than the ones obtained in the nip configuration. At 100 kHz, instead, the overlapping rate diminishes and better results are immediately obtained.

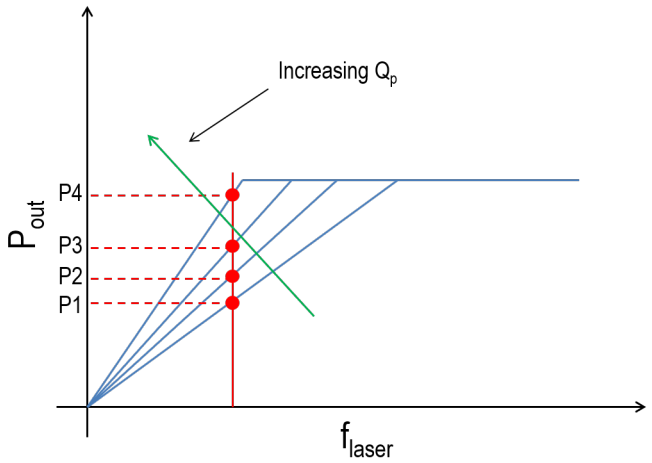

Figure 5.6: Schematic of the variation of output power depending on the laser pulse width. The higher it is, the lower is the cut off frequency. P1 corresponds to the average output power for the lowest Q_p, P4 to the average output power for the largest.

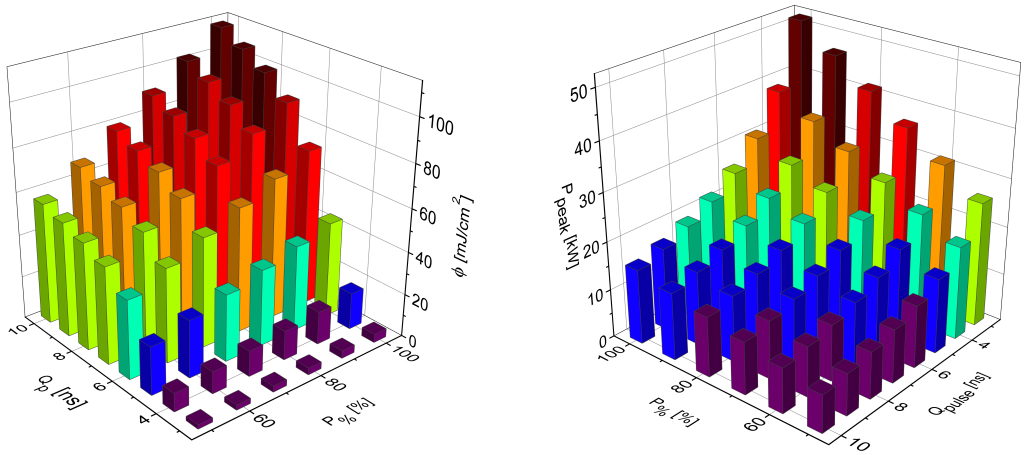

(a) **(b)**

Figure 5.7: **(a)** Laser fluence by varying the pulse width and the power percentage. **(b)** Laser peak power by varying the the pulse width and the power percentage

5.1.3. Variation of the laser speed

The last parameter visually optimized is the laser speed (v_{scan}). Figure 5.8 clearly shows that the reduction of the laser speed strongly increases the material removal process. Moreover, figure 5.8a shows that under a certain velocity threshold, that for nip is equal to 700 mm/s, even the metallic layer on the back is removed.

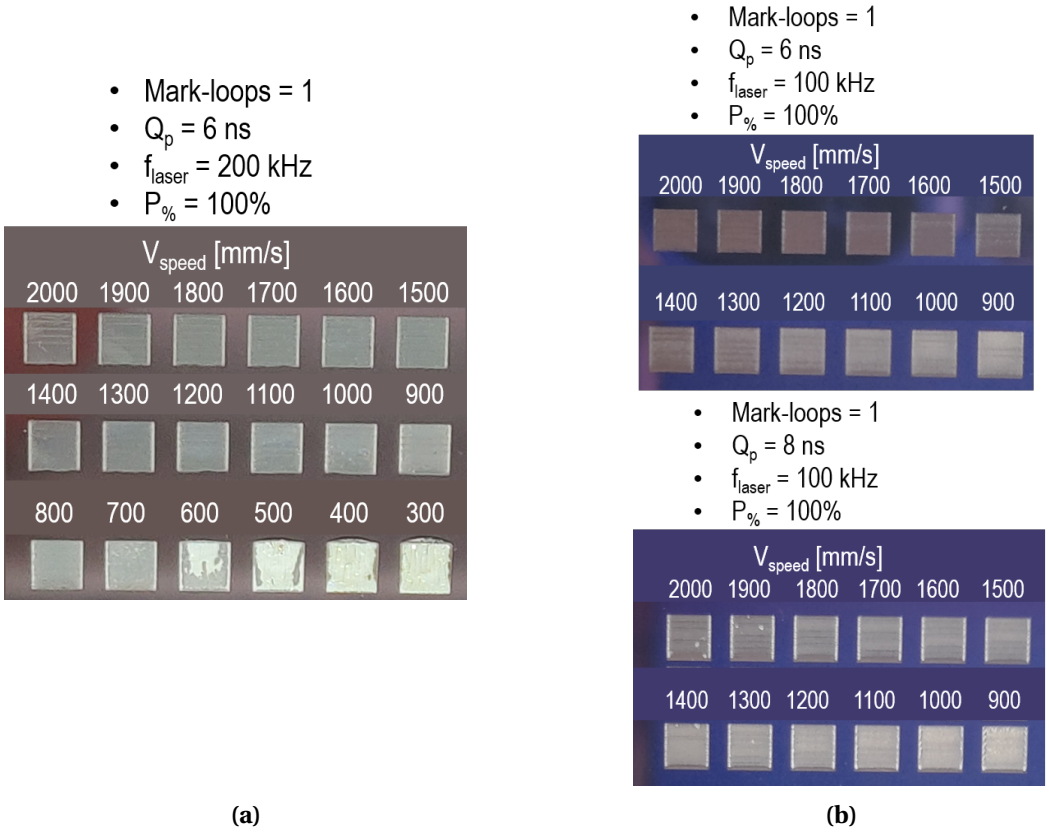

Figure 5.8: Pictures of the ablated squares varying the laser speed for **(a)** the nip solar cell and **(b)** the pin solar cell. The remaining parameters are kept constant depending on the type of solar cell. The pulse repetition frequency (f_{laser}) is equal to 200 kHz for nip and to 100 kHz for pin. The pulse width (Q_p) is constant at 6 ns fot nip, at 8 ns a for the top graph of pin and at 6 ns for the bottom graph of pin. The power attenuation rate is kept constant at 100% in all the cases. Only one marking loop is performed for all the graphs.

Since all the laser parameters except for v_{scan} are fixed (Q_p, f_{laser} and $P_{\%}$), the only driving phenomenon is the pulse overlapping rate.

Figure 5.9 shows a linear decreasing trend of $O_{percentage}$ while increasing the speed of the laser. As it was also concluded in paragraph 5.1.1, the variation in the material removal process is mainly due to the percentage of overlapping which occurs between two consecutive pulses: if a pulse hits the sample surface in the HAZ of the previous pulse, the material removal is increased and even the back metal can be removed. On the other hand, if the laser velocity is increased, the relative distance between the impinging points of the two different laser pulses is larger and the material removal is reduced.

Considering the whole optimization process introduced in the previous part of the chapter, the optimized laser settings are shown in table 5.1.

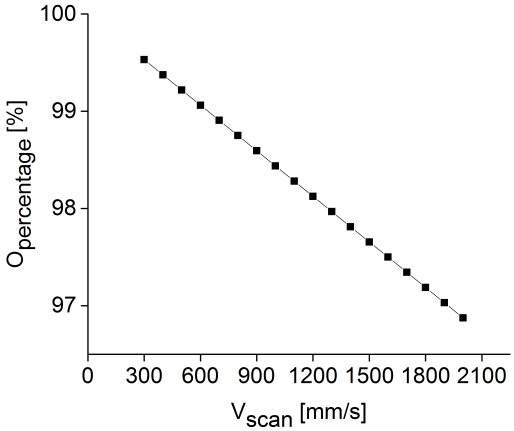

Figure 5.9: Rate of overlapping by varying the speed of the laser. Values are computed considering the settings used for the nip configuration.

Table 5.1: Optimized settings for laser cutting

	nip	**pin**
Laser speed [mm/s]	2000	2000
Power [%]	100	100
Pulse Frequency [kHz]	200	100
Pulse width [ns]	6	8

5.1.4. Phenomena related to material properties

Although the laser settings have been optimized by varying the parameters as shown in the previous steps, the ablation effect changes slightly when the shape of the cut is varied. From squares to lines, indeed, the ablation process differs and a continuous line is not always guaranteed. This is due to the pattern the laser follows to remove the material: during the drawing of squares, indeed, the laser tracks parallel adjacent lines as schematized in figure 5.10. For every line scribed in a square, indeed, the surrounding material is also affected by the generated heat. Therefore, material is more easily evaporated when it follows the ablation of an adjacent line. This does not happen when scribing single lines.

The discontinuity of the lines, moreover, is also due to the imperfect homogeneity of the deposited layers due to the limitations of the machines used at EKL laboratory. The sides of the samples, indeed, are generally slightly thicker than the central area of the sample. This, together with the absence of an HAZ, hinders the removal process. An increase in marking loops, especially on the side of the sample, is the solution adopted to completely evaporate the material.

Reflection, both at the front and at the rear side of the cell, is another important phenomenon that affects the material removal process. When metal is deposited at the back of the solar cell, the laser pulse is reflected back into the absorber layer, increasing the removal of the photoactive stack (Fig.5.11). With this feature, hence, a single pulse travels through the photoactive stack twice. On the other hand, in the case of glass on the rear side of the absorber layer, the intensity of the reflected part of the laser pulse is significantly lower than with the metal contact, and considerably less energy can be absorbed. The reflection of the pulse into the absorber material, however, does not really affect the thickness of the line scribed: the thickness of the material is indeed in the order of micrometers and it is possible to consider that the incident point of the laser is equal to the one

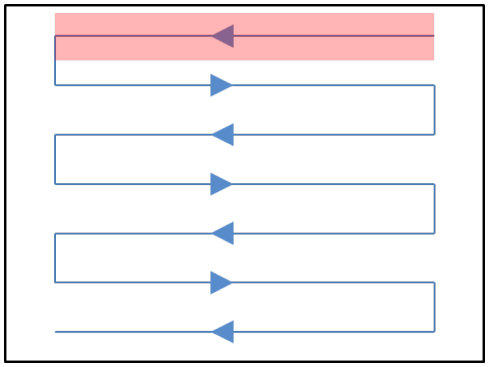

Figure 5.10: Schematic of the laser principle for the scribing process of a square

where it leaves the sample.

The difference between samples with metal on the back and without it is of significant relevance when analyzing the pin configuration. The visual optimization process previously described, indeed, has been performed using a full area front contact. In reality, when the laser ablation is performed on a working devices (see Chap:6.1), the front contact grid covers a minimal part of the front area of the sample. Therefore, for the most part of the designed lines the laser pulse is not reflected back in the absorber layer. An increase in the number of marking loops is one of the possible solutions in this case also. The several carried out experiments show that a high number of marking loops (even up to 50) guarantees the removal of the photoactive stack without removing the front contact on top.

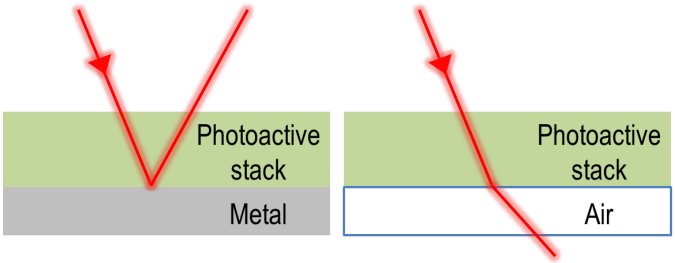

Figure 5.11: Schematic of the laser path with or without metal on the back of the photoactive stack

Lastly, the reflection induced at the front layer is also another relevant phenomenon. During the experiments carried out in the nip configuration, laser parameters had to be changed when varying the front TCO of the solar cell from AZO to ITO. In the laser wavelength range, indeed, the refractive index of the AZO layer is higher than for ITO, 1.81 and 1.73 respectively. Considering the case of perpendicular laser rays, since the real angle of incidence of the laser is unknown, from the *Fresnel equation* (eq.5.2) it is possible to deduce that the greater the refractive index mismatch with that of air is (n_{air}=1), the higher the reflectivity (R) of the material [8]. The higher the reflected part of the laser light is, the lower the energy absorbed, the more difficult the removal of the material is.

$$R = \left(\frac{n_1 - n_2}{n_1 + n_2}\right)^2 \tag{5.2}$$

in which n_1 is the refractive index of the first medium, air in the case of the carried out experiments, and n_2 is the refractive index of the second medium, the TCO layer. Experiments done using the settings found for pin show better cutting performances when ITO is used as front layer.

5.2. Analysis with the scanning electron microscope

In the second part of the laser scribing optimization process, an analysis of the ablated lines is carried out with a scanning electron microscope (SEM), in order to verify the effects of the laser pulse at microscopic level. Tens of pictures are taken with the microscope available at the faculty, and only the relevant ones are shown in this chapter.

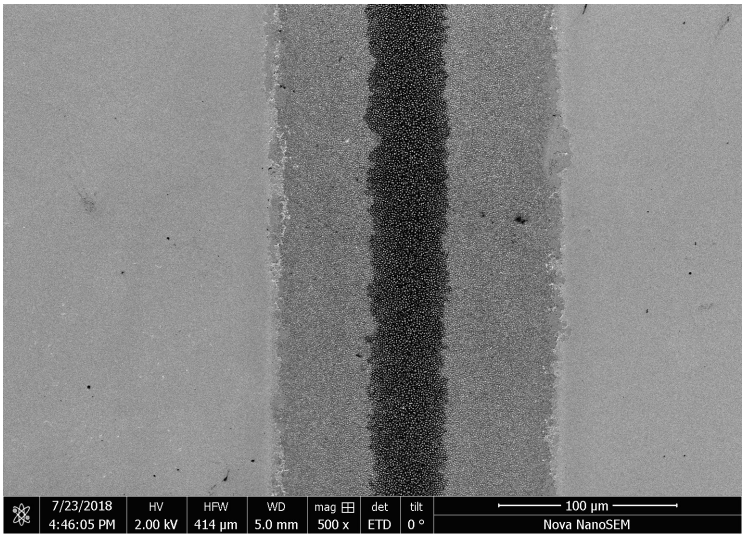

Figure 5.12: Example of a microscopic top view of a laser scribed line

If we zoom on the sides of the scribed lines (Fig.5.13), the defects due to heat conduction are clearly visible. The deposited layers are damaged and cracked, due to the high amount of heat that is delivered at every pulse. The expansion coefficients of the TCO and of the silicon layers underneath differ, and therefore, mechanical stress is induced by the different expansion rates. The creation of defects and cracked areas, moreover, is enhanced by the use of multiple marking loops: the materials, indeed, undergo multiple cycles of heating up and cooling down. The continuous expansion and shrinkage of the material intensifies the negative stress effects.

Moreover, figures 5.13a and 5.13b show the re-crystallization of the removed material on the side of the line. When the metal on the back is removed and deposited on the side of the line, the re-solidification of the metal could theoretically link the front to the back of the solar cell, strongly reducing the performances of the device.

Comparing figures 5.13b and 5.13c it is also possible to notice how the Gaussian shape of the laser pulse affects the ablating performances of the laser. The red circle of figure 5.13c shows the dimension of one laser pulse: the peak of energy delivered is focused in the centre of the line while the energy absorbed on the sides is less. Therefore, as shown in figure 5.13b, more material is evaporated in the centre than on the side, as it is clearly visible from the difference in color between the inner and the outer part of the line.

As aforementioned, moreover, heat diffusion represents an important problem in the laser cutting process. Figure 5.13d shows how the energy absorbed by the sample can even affect glass underneath the photoactive stack. The deposited material is in the order of 1.5 µm, while the depth of the affected material reaches around 17 µm. It is clear, comparing also the top and the bottom parts of the glass, how its crystalline properties change: melting and re-solidification processes occur successively with each marking loop. With that taken into account, it is likely that also part of the material that is not directly evaporated can melt due to the heat transmitted by the laser and

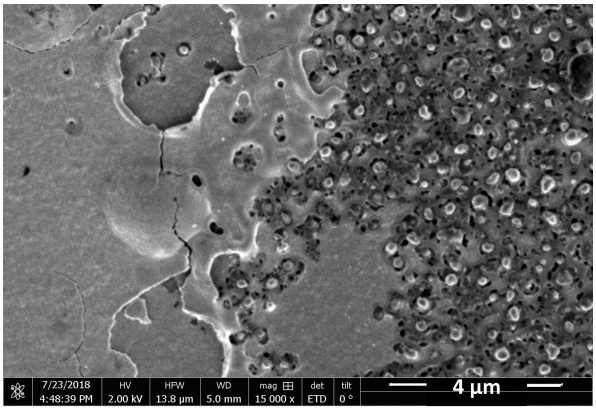

(a)

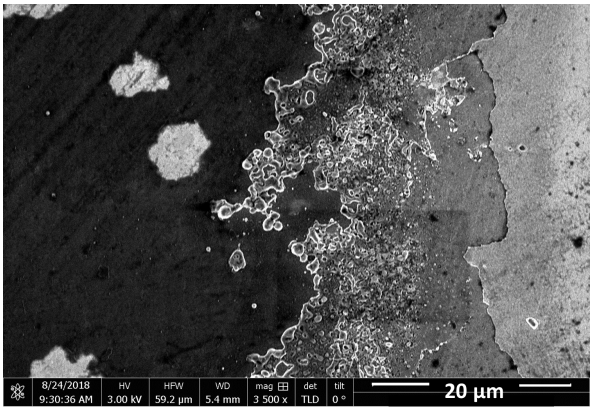

(b)

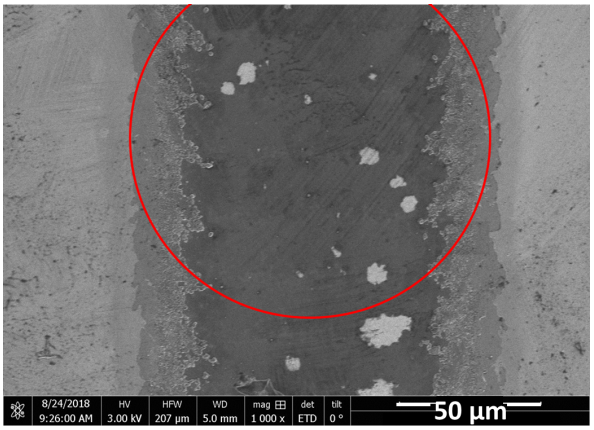

(c)

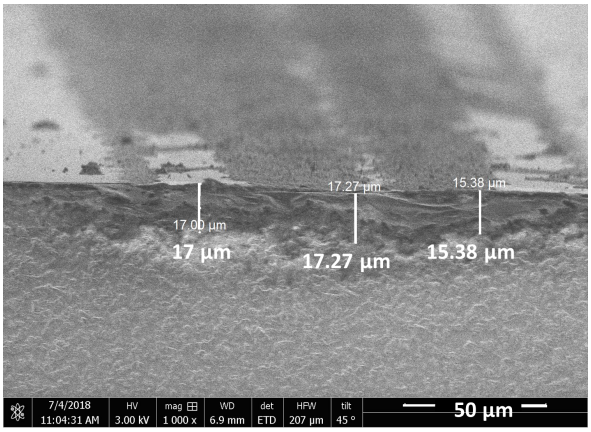

(d)

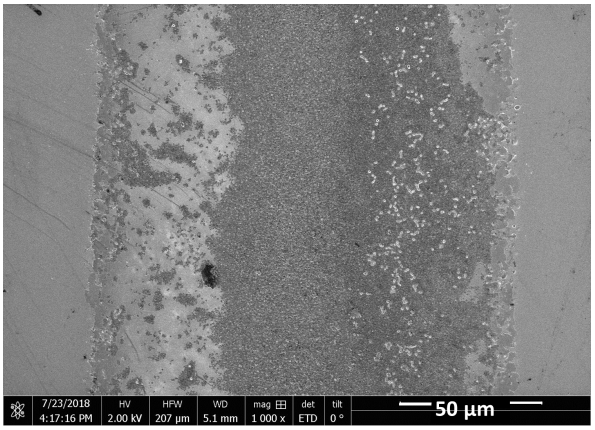

(e)

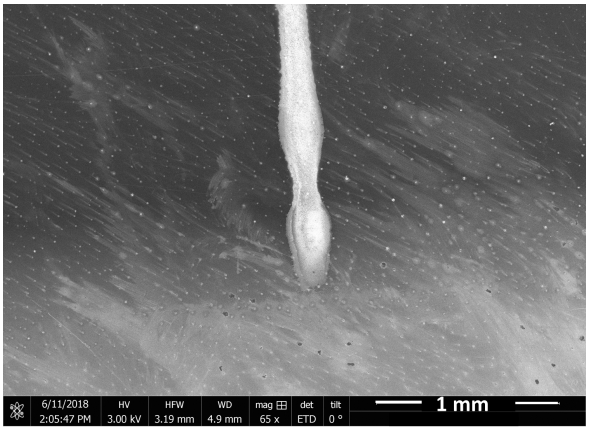

(f)

Figure 5.13: **(a)** Side of a laser scribed line from the top view. The solar cell is in nip configuration and 5 marking loops are performed. **(b)** Side of a laser scribed line from the top view. The solar cell is in nip configuration, with ITO as TCO in front, 1 marking loop is performed using the optimized settings of pin. Effects due to heat conduction and to material recasting are clearly visible on the right hand side. **(c)** Top view of the same laser scribed line as the one shown in figure **(b)**. The red circle shows the dimension of a single pulse. **(d)** Picture of the cross section of a ablated line. The effect of the heat transmitted by the laser pulses is shown. **(e)** Effect due to the not perpendicularity of the impinging laser rays from a top view. **(f)** Effects due to the change in thickness on the side of the ablated sample from a top view.

alloy with the surrounding material during re-solidification. For the visually optimized settings, however, we strongly suspect that the photoactive layers are completely removed, since the values of resistance measured with a multimeter are in the same range of the ones obtained for pure metals.

Figure 5.13e shows defects related to the position of the sample with respect to the fixed angle of the laser. The effect of the ablation does not seem symmetrical, even though the Gaussian shape of the laser is. This is due to the fact that, when the laser does not hit perpendicularly the sample, one side of the line is more affected by the impinging rays than the other, leading to a disparity in the resulting line.

Lastly, figure 5.13f shows how the change in thickness of the deposited layers on the side of the sample generates a variation in the width of the scribed line. The line widens and shrinks in succession. For the complete ablation of the edges to obtain a complete and continuous line, as already mentioned.

The number of marking loops and the speed of the laser are, therefore, parameters that must be optimized for each type of device in order to obtain sharp and neat cuts and to avoid short circuiting problems.

The following two paragraphs are meant to show the variation in performances by varying the aforementioned parameters.

5.2.1. Optimization of the marking loops

For the sake of simplicity only a few samples are shown. These are the samples with optimized scribes, performed on nip solar cells with AZO layer as front TCO (Fig.5.14). Conclusions and results are valid also for the other configurations taken into account.

Two significant trends are immediately clear when the number of marking loops increases: the laser scribed lines widen and the depth of ablation increases. Figure 5.14c clearly show that at 5 marking repetition loops not only the photoactive layer is ablated, but also part of the metal underneath.

Comparing the width of the lines of figure 5.14a, 5.14b and 5.14c the increasing trend of the width of the lines is evident. The lines, indeed, increase from almost 125 μm at 1 marking loop up to almost 160 μm at 5 marking repetition loops. As mentioned earlier, an increase in marking repetition loops increases the chance of material removal. The continuous absorption of energy on the sides due to the increase in marking loops allows a deep lateral removal too, even though, as already shown in figure 5.13b, the material removal on the side of the line is lower due to the Gaussian shape of the laser intensity.

The increase of crystallization of the generated debris is another significant effect of the increase in marking loops. The heat absorbed by the removed and partially removed material is sufficient to melt the re-deposited particles that then solidify and crystallize. When the number of marking loops increases above a certain threshold, however, the material can evaporate and deposit on the side of the lines, as shown in figure 5.14d. In view of the formation of a thin film mini-module, the just mentioned re-deposited material can form a conductive link between the back contact of the solar cell and the front TCO, thereby short circuiting the solar cell.

Considering the experiments carried out, both for the nip and pin configuration of the single junction amorphous silicon solar cell, a safe range of repetition marking loop is below 5/6 marking repetition loops. This can be considered an important limitation when the sides of the sample have

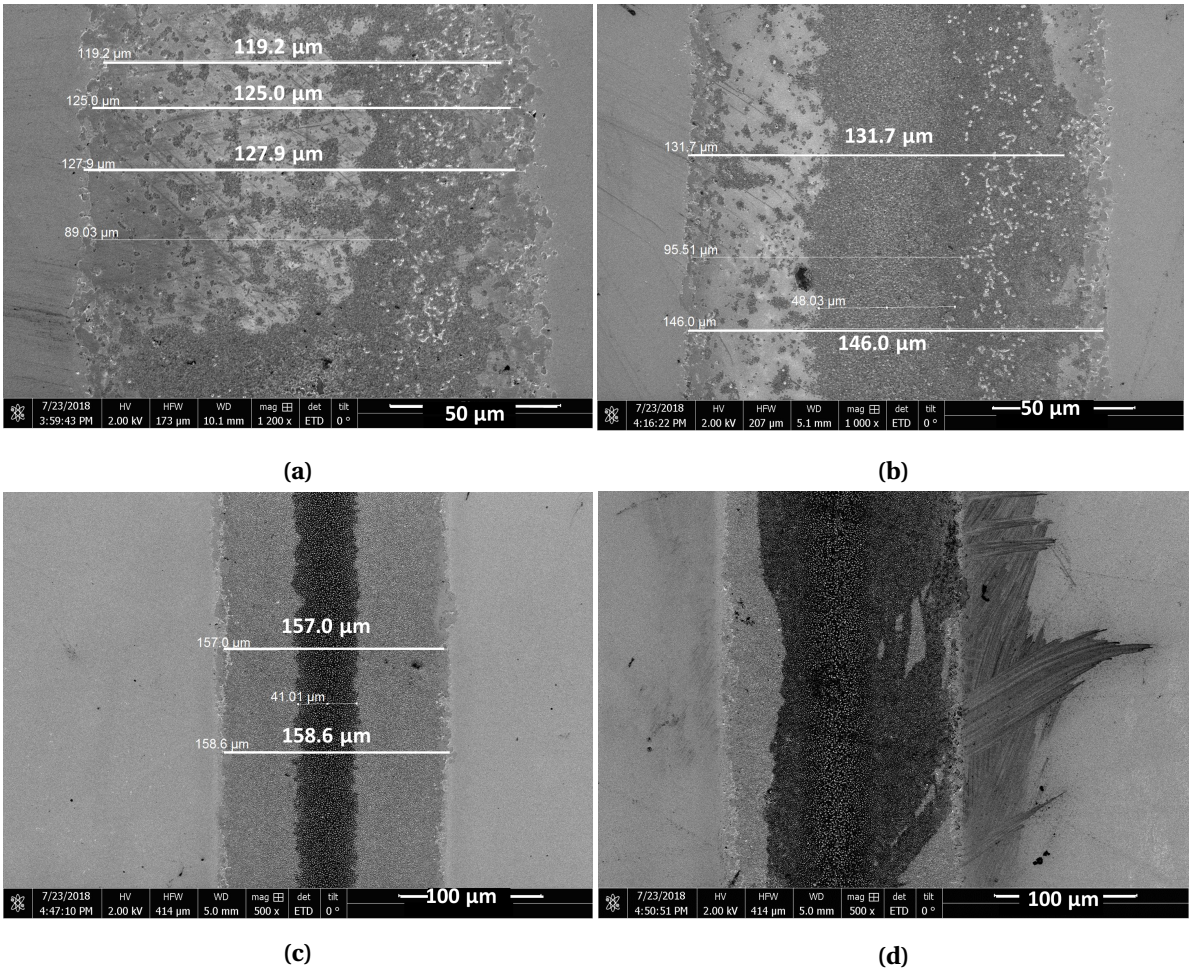

(a) **(b)**

(c) **(d)**

Figure 5.14: Laser ablated lines with parameters optimized for nip configuration (see table 5.1) and with increasing marking loops: **(a)** 1 marking loop, **(b)** 2 marking loops, **(c)** 3 marking loops, **(d)** 10 marking loops

to be removed: as previously mentioned in 5.1.4 in order to achieve a complete cut of the thicker layers a higher number of marking loops is needed. Therefore, alternatives to laser ablation have to be found to isolate the side of the solar cell.

5.2.2. Optimization of the laser speed

In the last part of the optimization process, the effect of the variation of the laser speed, that corresponds to the variation in $O_{percentage}$, is analyzed using the SEM. Figure 5.15 shows the result of four different experiments carried out on a nip solar cell. The optimized settings for the pin configuration shown in table 5.1 are used, since ITO is used as top layer of the cell.

The variation of laser velocity does not introduce a change in the width of the ablated lines: the total width, indeed, remains equal to almost 128 μm, and even the inner part of the scribed lines, that is the darker area shown in figure 5.15, is almost constant at around 93 μm.

However, a significant debris reduction on the side of the lines is clearly visible while increasing the speed of the laser. As already introduced in section 2.5.2, a high level of pulse overlapping can generate debris and undesired particles. The experiments carried out show that even the reduction

of 1.25% of $O_{percentage}$, due to the increase in velocity from 2000 mm/s ($O_{percentage}$ = 97.75%) to 2500 mm/s ($O_{percentage}$ = 96.25%), can induce a clear improvement in the sharpness of the cut. Compared to the laser scribing process in the series connected thin film modules, in which a clean and neat cut without flakes is fundamental to avoid the formation of shunts, the complete absence of particles and flakes is not needed in the parallel connected configuration designed in this thesis (see chapter 6.2). In the first case material is deposited on top of the laser scribed lines to interconnect two cells as shown in figure 2.8, and the presence of particles can lead to defects and shunts. In the second case, on the contrary, material is not deposited on top of the ablated lines and the laser scribing process is performed only to isolate two different cells. Hence, it is considered acceptable to ablate the desired lines with parameters that lead to a slightly high overlapping rate. The complete removal of the photoactive stack has to be guaranteed, despite the fact that the resulting cuts are not completely clean. Therefore, a higher velocity than the one written in table 5.1 is needed. 2500 mm/s can be considered an optimized value to reduce the formation of defects still guaranteeing the removal of the photoactive stack.

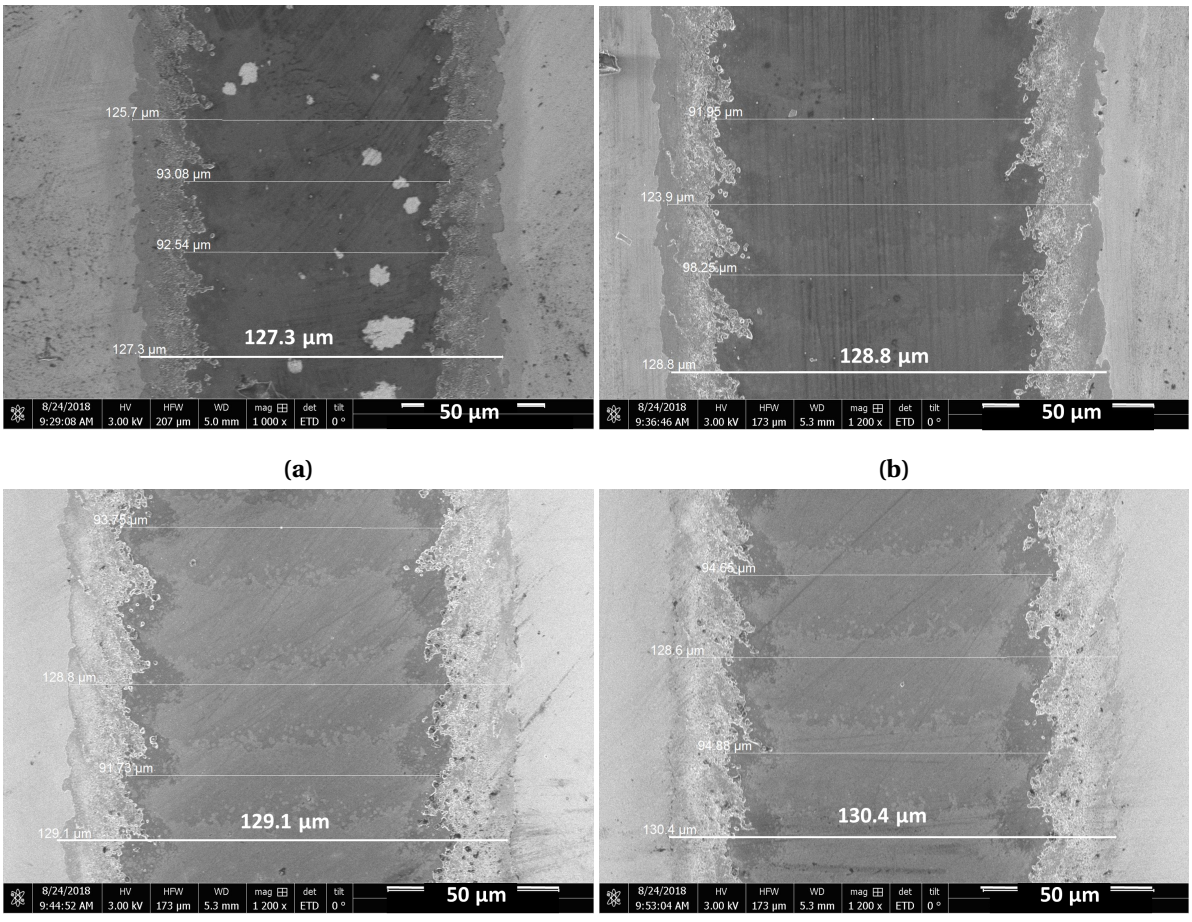

Figure 5.15: Laser ablated lines with parameters optimized for pin configuration (see table 5.1) on a nip solar cell with ITO as TCO and one single marking loop. Laser speed is increased progressively to check the effect of decreasing pulse overlapping: **(a)** 2000 mm/s, **(b)** 2100 mm/s, **(c)** 2200 mm/s, **(d)** 2500 mm/s.

5.3. Conclusions

In order to deposit large area solar cells in nip substrate and pin superstrate configuration a laser scribing process must be performed to isolate the solar cells. Laser parameters have been optimized in two different steps, a visual optimization first and an analysis using a scanning electron microscope later.

During the first part of the optimization process small squares are scribed by varying two parameters at a time, so to understand the influence of each setting during the ablating process. It is clear that the percentage of pulse overlapping plays a fundamental role in the ablating process, and not only the amount of energy absorbed is crucial. The material, indeed, does not have sufficient time to cool down at high values of $O_{percentage}$, and the material evaporation is strongly increased. This effect is apparent both by varying the speed of the laser and by varying the laser repetition frequency. The variation in pulse width, on the other hand, induces a change both in the laser fluence and in the pulse peak power delivered. A reduction in the pulse width increases the peak power per pulse, which can theoretically lead to better and sharper ablated lines. When the pulse width changes from nanoseconds to femtoseconds the material is removed by sublimation, and debris-free lines can be scibed. During the experiments carried out the pulse width is varied in the range between 10 ns and 3 ns, and melting remains the primary process for material removal. Therefore, a larger heat affected zone generated by a larger pulse width is preferred to a higher peak power, which would result from short pulses. The reflectivity of the material and the pattern followed by the laser, moreover, highly influence the material removal performances.

In the second part of the laser optimization analysis, pictures were taken using a scanning electron microscope in order to analyze the microscopic defects induced by the laser. Heat is the major cause both for the generation of cracks and other defects that can reduce the performances of a solar cell. In addition to the already mentioned dependency on the laser fluence and on the pulse overlapping rate, the the effects of the heat also increment with the increase of the marking loops. Therefore, a low number of marking loops is necessary in order to avoid an excessive production of particles that can short circuit the solar cell.
Debris and particles, moreover, are also generated at high pulse overlapping rate. With increasing laser speed, that is, with decreasing overlapping rate, the edges of the ablated lines start to become neater and sharper, reducing the risk of shunting. 2500 mm/s has been considered a safe speed level to obtain the absence of shunts while the removal of the photoactive stack can be achieved.

The optimized parameters to laser scribe a pin and nip solar cell are shown in table 5.2:

Table 5.2: Optimized settings for laser cutting

	nip	**pin**
Laser speed [mm/s]	2500	2500
Power [%]	100	100
Pulse Frequency [kHz]	200	100
Pulse width [ns]	6	8

6

Solar cell depositions

This chapter is meant to answer the last research question introduced in chapter 1.2:

Is it possible to deposit large area pin or nip solar cells by using the previously optimized techniques?

Solar cells have been deposited both in pin superstrate and in nip substrate configuration in order to analyze and compare the results obtained from the implementation of the front contact grid optimized in chapter 4 and the laser scribing process optimized in chapter 5. The deposition of the front contact grid is indeed a straightforward solution in pin superstrate configuration to mitigate the detrimental effect of the shunting problems. A front contact grid reduces the charge carrier movement distance to the metallic contact, decreasing the chances of charge carriers being attracted by shunts. A similar reasoning is applied to the use of the laser scribing process in a nip substrate solar cell: the subdivision of the sample in small cells reduces the chances that shunts become dominant. Moreover, by connecting the cells in parallel a mini-module with low voltage and high current can be obtained.

In this chapter, the results of the numerous experiments carried out are divided in two main sections, depending on the type of solar cell considered: in the fist subchapter pin solar cells are analyzed and the results following the introduction of a front grid are shown, while in the second part of the chapter the nip solar cells are discussed.

6.1. Pin solar cell

One of the main goals of the thesis project is to deposit a large area 10 × 10 cm^2 solar cell in pin superstrate configuration. The structure of the solar cell is the following: 16 nm p-SiOx:H, 250 nm i-a-Si:H, 65 nm n-SiOx:H and 300 nm Ag/30 nm Cr/500 nm Al as back contact (Fig. 6.1). The TCO is varied and studied during the experiments, as explained further in the chapter.

Unfortunately, even the introduction of the front metal grid optimized in chapter 4 does not allow the immediate deposition of a working large area pin solar cell: shunt leakages are prevalent and the solar cells show resistive behavior. Several manufacturing problems have to be addressed to reduce the risk of defects and shunts.

The isolation of the edges is one of the major problems related to the deposition of a solar cell on a large surface. The homogeneity of the layers deposited by plasma enhanced chemical vapor deposition (PECVD) is limited by mechanical constraints of the equipment of the EKL. Because of the inhomogeneity of the layers and the presence of pinholes and surface defects, localized points of

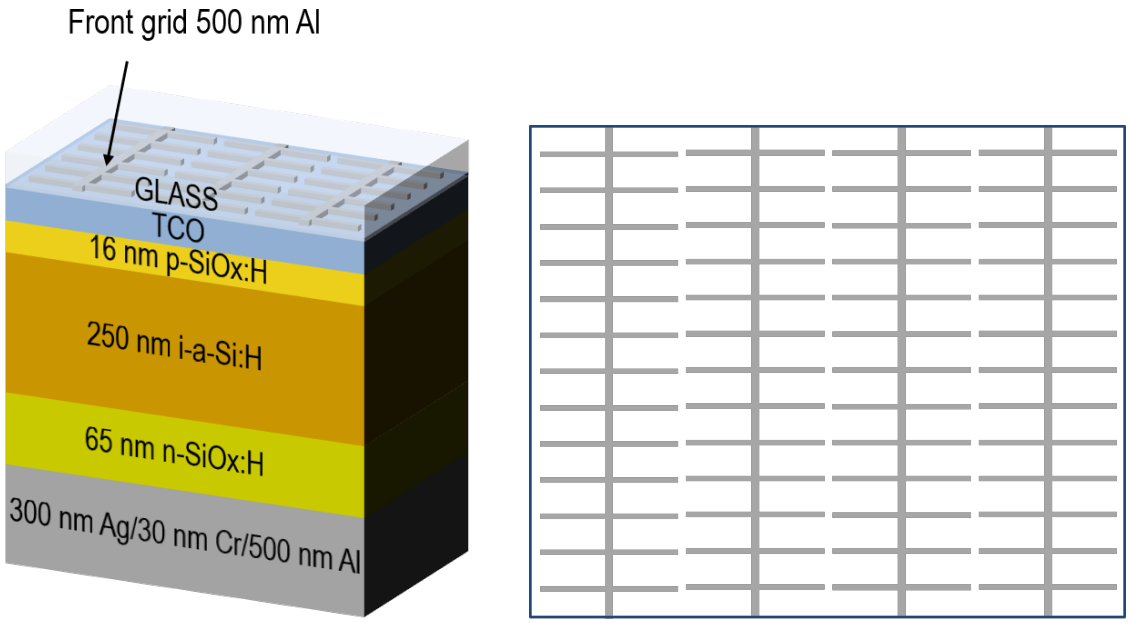

Figure 6.1: **(a)** 3D schematic of the pin superstrate solar cell. **(b)** Schematic of the top view of the solar cell.

shunts are likely to be generated at the edge of the solar cell. Two different options are tested in order to isolate the edges from the inner part: laser ablation and physical isolation by using heat resistant Kapton tape prior to the deposition of the photoactive stack.
The edge isolation by laser scribing the sides of the sample is a difficult process with several drawbacks. For this sake experiments are carried out both impinging on the front and on the rear side of the solar cell. The presence of a full metal back contact hinders the ablation of the material from the back: the high reflectivity of the layer, indeed, significantly reduces the absorbed laser intensity. High energy pulses are therefore needed to successfully draw the desired line. High energy pulses, however, lead to high melting rate: the possibility that the back metal melts and alloys together with the photoactive stack increases significantly, and shunt leakages are very likely. On the other hand, when the laser ablation is performed from the front side, it is possible to avoid the removal of the back metal. The evaporated material, however, is trapped in between the front glass and the back contact and deposits on the sides of the scribed lines. Also in this case, problems related to shunt leakages are likely to be generated. Physical isolation by Kapton tape is, therefore, the preferred option to isolate the edges. Kapton tape is put on top of the front glass after the deposition of the front grid and prior to the deposition of the photoactive stack. Silicon layers, hence, deposit on top of the tape: when the tape is removed, perfect isolation is guaranteed. Small pieces of aluminum foil, moreover, are used in order to prevent the front aluminum contacts from peeling off when the tape stripes are removed.

Compared to the samples deposited without isolation on the edges, in which no electrical properties are found, an open circuit voltage (V_{oc}) around 0.8 V is measured for different samples of different dimensions: 2.5 × 9.5 cm^2 ($\frac{1}{4}$ of the large front contact grid), 6 × 6 cm^2 and in others with a smaller dimensions. The dimension of the solar cell is varied in order to verify its influence on the occurrence of shunting defects. Unexpectedly, however, although V_{oc} can be measured, the efficiency of all the deposited cells remains negligible.

An analysis of the front contact design on the solar cell performances is then carried out to understand the influence of the addition of a front grid.

6.1.1. Influence of the front contact design

The analysis of the influence of the design of the front contact on the solar cell performances is carried out in order to verify if the introduction of a front grid does not generate localized irregularities that can lead to shunt leakages.

Usually, indeed, at the EKL the front metal busbar to extract the charge carrier is deposited next to the area where the back metal contact is located and the TCO is used to enhance the lateral conduction of charge carriers. In the configuration designed in this project to deposit the large area pin solar cell, the front contact grid and the full back metal contact are aligned in the growth direction (Fig.6.1a). That is the reason why the effect of the presence of a 500 nm thick aluminum layer is studied.

Experiments are carried out depositing 16 mm^2 solar cells varying the order of deposition of the TCO and of the front metal grid. For the sake of simplicity the three different configurations are named as follow (Fig. 6.2):

- **conf 1** corresponds to the solar cells in which the front grid contact is deposited on top of the FTO;
- **conf 2** corresponds to the solar cells in which the front grid contact is deposited on flat glass and the AZO layer 700 nm thick afterwards;
- **conf 3** corresponds to the solar cells in which the front grid contact is deposited on top of the previously deposited AZO layer 700 nm thick.

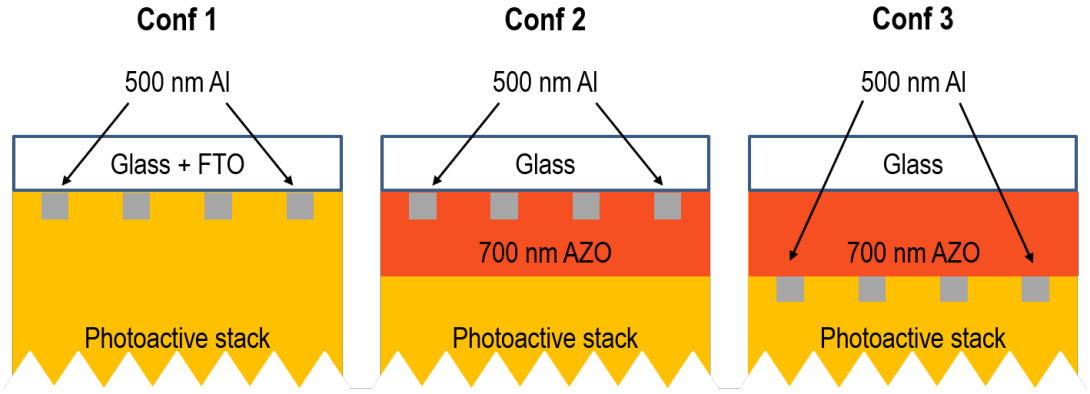

Figure 6.2: Schematic of the three front contact configurations analyzed.

Since the back contacts are equally distributed along the length of the sample, some of the back contacts are in the same transverse line of the front metal grid (Fig. 6.3b). An analysis of the difference occurring among the solar cells that are transversely aligned with the back contact and the ones that do not is therefore possible.

Figure 6.3a shows the J-V curves of the best performing solar cells deposited. It is clear how the introduction of a front grid affects the short circuit current density of the solar cell (J_{sc}). In all the three configurations analyzed, indeed, J_{sc} is lower when the back metal overlaps the fingers of the front grid. This is due to the fact that the front contact shades the solar cells preventing part of the impinging rays from being absorbed. In theory, considering the designed size of the fingers of the

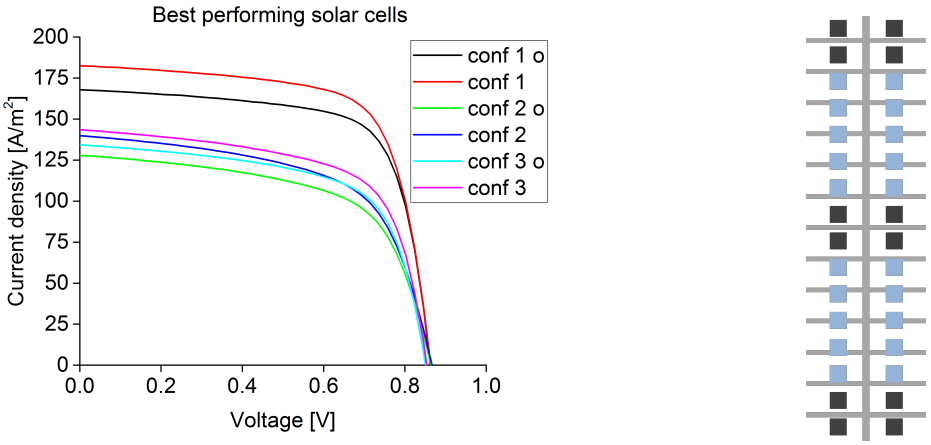

(a) **(b)**

Figure 6.3: **(a)** JV curves of the best performing solar cell in different configurations depending on the configuration used. **o** indicates the curve related to the cells in which the back contact is overlapping the front grid. **(b)** Schematic of the difference between overlapping (light blue) and not overlapping solar cells (black)

front grid (which is 0.23 mm), fingers cover almost 5% of the total area of the solar cell. In practice, even a larger area is shaded, since the front contact fingers and the busbars slightly widen because of the deposition technique. The imperfect adhesion of the sample to the front grid mask allows part of the evaporated metal to deposit in between the front mask and the sample even in the not designated area, slightly increasing the dimension of the fingers and of the busbars.

Apart from the variation in J_{sc}, comparing the solar cells with the front and back contacts aligned with the ones that do not of the same configuration, the introduction of the front grid does not really affect the performance of the solar cell: table 6.1 shows the values of J_{sc}, open circuit voltage (V_{oc}), current density at maximum power point (J_{mpp}), voltage at maximum power point (V_{mpp}), series resistance (R_s), shunt resistance (R_{sh}), fill factor (FF) and efficiency (η) of the deposited solar cells.

Table 6.1: Values of J_{sc}, V_{oc}, J_{mpp}, V_{mpp}, R_s, R_{sh}, FF and η of the best performing deposited solar cells

	conf 1 o	**conf 1**	**conf 2 o**	**conf 2**	**conf 3 o**	**conf 3**
J_{sc} [A/m²]	167.9	182.5	128.0	139.9	134.3	143.6
V_{oc} [V]	0.862	0.864	0.864	0.867	0.851	0.854
J_{mpp} [A/m²]	143	158	100	108	105	113
V_{mpp} [V]	0.714	0.692	0.670	0.670	0.692	0.692
R_s [Ω·m²]	10.8	15.3	39.5	41.5	18.1	16.1
R_{sh} [Ω·m²]	5237	4955	3457	2983	3421	3017
FF [%]	70.4	69.4	60.3	59.5	63.6	63.8
η [%]	10.2	10.9	6.67	7.21	7.27	7.82

In addition to the variation in J_{sc}, figure 6.3a also illustrates that the order of deposition of the front grid and of the TCO does not have a notable influence on the performances of the solar cell. The curves of **conf 2** and **conf 3** do not indeed differ significantly. Moreover, the average values obtained by measuring all the 30 cells deposited are really close, as shown in table 6.2.

Table 6.2: Average values of η, FF, J_{sc} and V_{oc} for **conf 2** and **conf 3**, in order to analyze the influence of the order of deposition of the front metal grid and the TCO

	conf 2 o	**conf 2**	**conf 3 o**	**conf 3**
η **[%]**	5.89	6.55	6.7	7.5
FF [%]	57.51	58.17	52.78	61.85
$\mathbf{J_{sc}}$ **[A/m^2]**	120	130	130	142
$\mathbf{V_{oc}}$ **[V]**	0.87	0.87	0.85	85.28

On the other hand, the type of TCO and of glass used (FTO is deposited on top of a textured glass by Asahi company, while AZO is deposited on flat corning glass) leads to a remarkable difference in the performances measured. The difference in efficiency between the samples of **conf 1** and the others is indeed around 3.5%. J_{sc} is also significantly higher than in the configurations with AZO as TCO. The increase in performance is mainly due to the textured surface of the glass, which enhances the absorption of light.

The experiments carried out by the deposition of the 16 mm^2 solar cells also show that the difference in the configurations does not introduce a significant change in the number of not performing solar cells: except for the cells at the edges of the samples, which are affected by the change in thickness of the layers due to the not homogeneous depositions, all the remaining cells for each configuration show similar performances, and only few cells (maximum 2) per samples are not working.

6.1.2. Progressive upscaling of the solar cells

After having analyzed the influence of the front contact on the solar cell performance, pin solar cells have been gradually upscaled. As explained in paragraph 6.1.1, a difference in the configuration of the first layers induces a variation in the performances of the 16 mm^2 solar cells, but not in the number of working cells. Therefore, solar cells of different dimensions are deposited both with FTO and AZO as TCO. However, only **conf 1** and **conf 2** are considered. The difference in performances between **conf 2** and **conf 3** is indeed not relevant. An additional transfer step, however, needs to be introduced in order to manufacture **conf 3**, which increases the possibility that some particles might attach to the surface of the sample itself. The samples must be indeed transferred from the magnetron sputtering deposition machine (AMIGO), to the metal evaporation chamber (PROVAC) and then to AMIGO again. At each transfer a vacuum break occurs. During a vacuum break there is a risk of contamination or growing an oxide layer, which might have adverse effects on the cell performance. Samples are transferred only once when the metal is deposited first and AZO later, which simplifies the whole process and reduces the risks of particles contamination.

Figure 6.4a shows the three sizes of back contact deposited. The photoactive stack is deposited on the full area of the sample, while the back contact defines the cell area. The three sizes deposited are: a rectangular solar cell of 0.5 × 2 cm^2, a squared solar cell of 1 × 1 cm^2 and a rectangular solar cell of 3 × 2 cm^2.

A relevant result is immediately noticed from the measurements: the type of configuration used not only does affect the performances of the solar cell but also the process of upscaling. None of the cells deposited in **conf 2** show important performances. On the contrary, some of the solar cells deposited on the glass provided from Asahi company work properly with significant performances. The AZO layers deposited at the EKL are characterized by a higher irregularity of the surface compared to the FTO ones, which are industrially obtained by the Asahi company. The higher irregularity of the surface leads to higher chances of having defects, hence of shunted solar cells (see par.2.4).

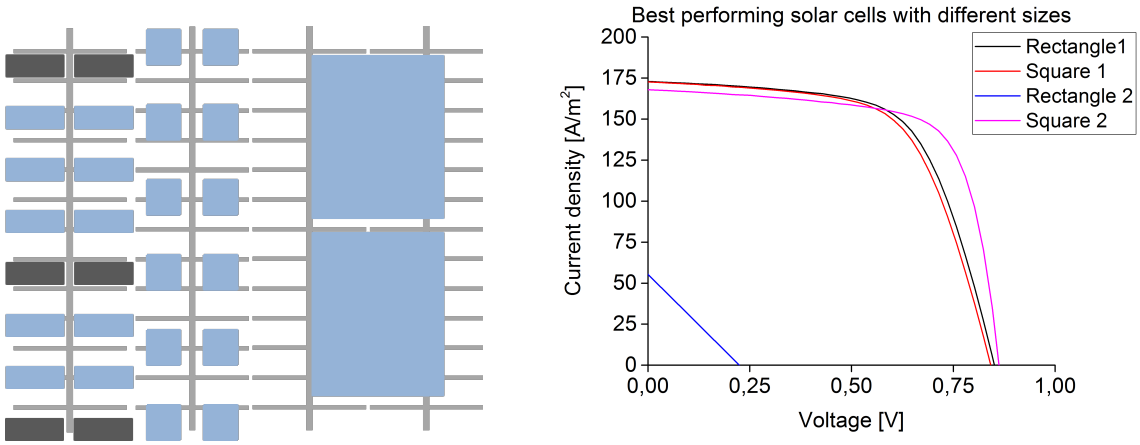

Figure 6.4: (a) Schematic of the solar cells with different size and shape. **(b)** J-V curves of the best performing solar cells deposited on FTO. **Rectangle 1** represents the 0.5 × 2 cm^2 solar cell. **Square 1** corresponds to the 1 × 1 cm^2 squared solar cell. **Rectangle 2** is the 2 × 3 cm^2 rectangular solar cell. Lastly, **Square 2** corresponds to the best performing solar cell of 4 × 4 mm^2 solar cell.

Figure 6.4b shows the J-V curves of the best performing solar cells of different dimensions deposited on the Asahi glass. It is evident that the introduction of the front grid does not solve the issues related to the increase in dimension of the solar cells. Comparing the curve of the squared 16 mm^2 solar cell to the rectangular and squared ones of 1 cm^2 the decrease in shunt resistance of the solar cells is evident. As a matter of fact it passes from 5236.85 $\Omega \cdot m^2$ of the smallest size, to the 876 $\Omega \cdot m^2$ and 742.99 $\Omega \cdot m^2$ of the bigger rectangle and square respectively. This is also reflected in a decrease in FF, which decreases by almost 10%, from 70.37% of the small cells to 63.12% and 61.99% for the larger rectangles and squares, respectively. The drop in R_{sh} can be mainly attributed to the increased possibility of having defects in the active area of the solar cell when the solar cell size is larger. This is especially clear when analyzing the 6 cm^2 solar cell: the almost complete absence of performance indicates, indeed, that the reduction of the charge carrier movement distance to the metallic contact by the implementation of the front grid is not sufficient to solve the problems due to the high defect density of the a-Si:H material. Shunts are actually still dominant when the solar cell size is increased.

The design of another front grid with a higher number of fingers, that would further reduce the space charge carriers have to travel, can be one of the solution to improve the charge carrier collection and overcome the problems related to upscaling solar cells. The use of a different or thicker absorber layer is another option that should be investigated to verify whether a front grid can be a solution in upscaling processes.

6.2. Nip solar cell

Experiments to upscale thin film solar cells in nip configuration are also carried out. A novel thin film mini-module concept is designed in order to create devices with an open circuit voltage that can be suitable for water treatment devices, as explained in chapter 1.1. The structure of the solar cell is the following: 75 nm n-SiOx:H, 250 nm i-a-Si:H, 16 nm p-SiOx:H and 200 nm ITO (Fig. 6.1). The back contact is varied and analyzed during the experiments (Fig.6.5)

The total surface of the sample is divided by a laser scribing process into small solar cells of 1 cm

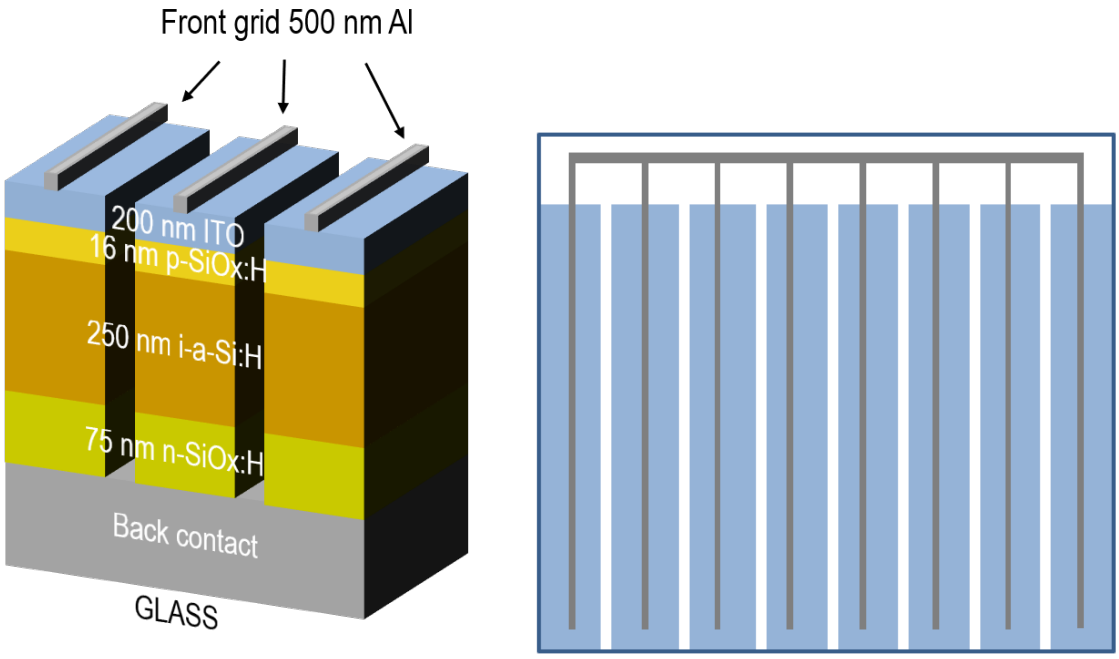

(a) **(b)**

Figure 6.5: (a) Schematic 3D structure of the nip mini-module. **(b)** Top view of the nip mini module. The light blue area corresponds to the nip solar cells. At the top of the sample busbars are connected in order to allow the parallel connection of the cells at the front

width. One busbar per cell is then deposited on top of the solar cells in order to extract the generated charge carriers. A new mask is designed to deposit the front contact busbars by metal evaporation (Fig.B.1).

Similar to the pin solar cell (Chapter 6.1), the implementation of a laser scribing process together with the deposition of the designed busbars does not immediately lead to a working solar cell. Also in this configuration the isolation of the more homogeneous central part of the sample from the edges is of significant importance. The change in thickness of the deposited layers can affect the performances of the solar cells and of the whole mini-module. Unlike in the pin configuration where Kapton tape must be placed to isolate the edges prior to the deposition of the silicon layers, in the nip configuration laser ablation can be used: the laser, indeed, is incident on the front side of the sample and the removed material, that is, the TCO and the photoactive stack, can easily evaporate without being trapped between the front glass and the back contact. However, in nip substrate solar cells the isolation of the edges does not lead to significant performance improvements of the mini-module. Therefore, as for pin configuration, an analysis of the configuration of the back contact is performed in order to evaluate its influence on the performances of the solar cell.

6.2.1. Influence of the back contact on the solar cell performances

Small area solar cells are deposited with three different configurations in order to analyze the influence of the back contact on the solar cell performances. In the first configuration the nip photoactive stack is deposited on top of a full back metal contact (500 nm Al, 30 nm Cr, 300 nm Ag). In the second configuration the back metal contact is substituted by 700 nm AZO layer. The third configuration is similar to the first one, but almost 200 nm of ITO is deposited on top of the back metal stack as protective layer.

None of the solar cells deposited in the first configuration produced any remarkable result. The deposition of the back metal by metal evaporation, indeed, does not produce a perfectly homogeneous layer and several localized uncovered spots are present. Defects and inhomogeneities are extremely numerous and shunting problems prevail.

In the remaining two configurations, working solar cells are measured. The measured J-V curves are shown in figure 6.6.

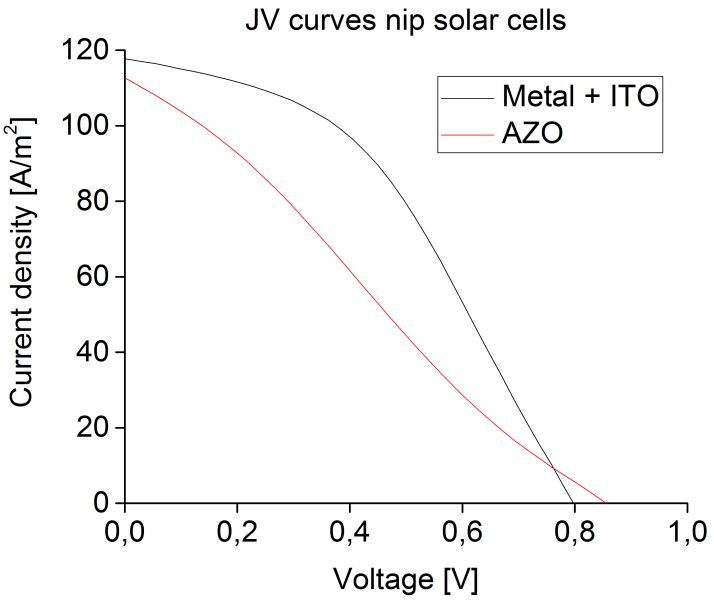

Figure 6.6: J-V curves of the nip solar cells

Solar cells deposited on AZO show poor performances with low values of efficiency: η is equal to 2.47% for the best performing 16 mm^2 nip solar cell. The low performances are both due to a not perfectly optimized recipe and to the fact that the absence of a reflecting back surface reduces the amount of energy absorbed. If a metal back contact is present, the solar rays are reflected back into the absorber layer and the energy absorption is enhanced. In the case of AZO layer used as back contact, the not absorbed part of the light is transmitted through the back contact and its energy is lost. The curve of the solar cell deposited on top of the metal is indeed showing better performances: the efficiency of the best performing 16 mm^2 solar cell rises up to 4.05%. Furthermore, to be noticed is the fact that the use of ITO allows the deposition of working solar cells on a back metal contact. The ITO layer acts as a protective layer smoothing the surface defects of the back metal contact.

Moreover, in none of the samples deposited not all of the delimited solar cells were performing at the same time, and some of them were shunted. This indicates that the possibility of shunting defects in the full area of the sample are significantly high. This fact becomes relevant when upscaling the solar cell to the 1 × 9 cm^2 solar cells designed for the mini-module configuration. None of the cells deposited, neither with Metal+ITO nor with AZO as back contact, show any significant performance and a working mini-module can not be produced.

6.3. Conclusion

In order to investigate the possibility of uspscaling lab-scale solar cells to a total surface area of 10 × 10 cm^2, two different solar cell configurations have been analyzed. Pin superstrate and nip substrate a-Si:H solar cells were deposited on various substrates to evaluate the difference in final performance between novel structures. In order to do that, the previously optimized front contact grid and the laser ablation process have been applied in the two configurations respectively, to decrease the detrimental effects that are created by the shunts. A large dimension of the sample increases indeed the likelihood of some shunts being present in the active area of the solar cell.

At first, a better isolation of the edges has been achieved in both the configurations through physical isolation and laser scribing. At the edges of a solar cell unpassivated dangling bonds are more probable, and localized points of recombination are likely. At the same time, the inhomogeneity of the layer thickness, due to the limitations of the equipment of the laboratory, and the higher possibility of having pinholes in the material are among the major causes of shunting defects in the deposited devices. Heat resistant Kapton tape for pin superstrate solar cells and the laser scribing process for nip substrate solar cells have been used to separate the central part of the sample from the sides. Compared to the initial samples deposited on a large area in which a performance could not be measured, a promising increase of the open circuit voltage has been reached.

In order to find the source of shunts, pin superstrate solar cells have been gradually upscaled through the deposition of several samples. On the one hand, we have observed that the presence of a 500 nm Al front grid did not introduce any further shunting defects. On the other hand, the effects induced by different front contact configurations have been investigated. Back contacts with an area of 16 mm^2 were deposited on the same transverse line of the front contact grid after the deposition of the photoactive stack. Different front contact and TCO combinations were used: metal grid first and AZO layer after on corning glass, AZO layer first and metal grid after on corning glass, metal grid on Asahi glass which has FTO already deposited on top. The fact that some of the back contact were transversely aligned to the fingers of the front grid and some were not, lead immediately to the first conclusion: even though it has a significant thickness with respect to the photoactive stack, the presence of the aluminum layer at the front was not inducing further shuntig defects. The decrease in performance of the cells in which the back contact was aligned to the front grid was indeed only due to the reduced active area of the solar cell. Furthermore, the difference in front contact configuration lead to another important consideration: the presence of the texture surface of the Asahi glass improves the absorption of light, and the deposited solar cells were achieving an average efficiency 3.5% higher than in the other configurations. By upscaling the solar cells to 1 cm^2 and further, it has been noted that the configuration of the front contact affects the amount of shunts present in the sample area. Working solar cells at a 1 × 1 cm^2 were indeed obtained only when depositing on Asahi substrates. We suspect that the smaller amount of impurities due to the industrial deposition of the FTO on top of the glass reduces the quantity of shunting defects in the sample area, allowing the deposition of larger solar cells. However, shunt resistance values were decreasing from almost 5200 $\Omega \cdot m^2$ to almost 800 $\Omega \cdot m^2$ comparing the 16 mm^2 to the 1 cm^2 solar cells on Asahi substrates. The presence of the designed front contact grid reduces the charge carrier movement distance to the contact, thus the chance of the charge carriers being drawn towards a shunt. However, the high density of shunts through the a-Si:H bulk prevents this technology from being upscaled. For solar cells larger than 1 cm^2 no significant performance was observed, even with the deposition on Asahi substrates

A similar analysis has been carried out also for nip substrate configuration. Solar cells with an area of 16 mm^2 have been deposited on different back contact configurations in order to analyze their influence on the performance of the solar cell. 700 nm thick AZO layer, 500 nm Al/30 nm Cr/300 nm

Ag metal contact and the same back metal contact but covered with 200 nm ITO have been used in different samples. Working solar cells have been obtained only when AZO or back metal+ITO were present. The use of ITO on top of the metallic back contact smoothened the pinholes and surface defects resulting from the metal evaporation deposition of the full area back contact, reducing the risk of shunts. Moreover, the presence of the metal layer at the back of the sample increased the fraction of light reflected back into the absorber layer. Solar cells deposited on top of metal+ITO were indeed generating better performances than the ones in which AZO was on the back. However, larger solar cells were not obtained. Even the use of the laser scribing process to reduce the size of the cell to try to prevent charge carriers from being drawn towards a shunt was not giving the expected result. The high shunt density that characterizes the a-Si:H material is dominant also in this configuration, and the subdivision of the sample in small cell is not enough to avoid the recombination of the charge carriers prior to their collection.

Overall, several solar cells configurations have been investigated and various problems related to the depositions in superstrate or substrate configuration have been solved. However, large area solar cells were not obtained due to the high shunt density of the a-Si:H technology. A thicker or different absorber layer should be investigated to verify if large working solar cells with the designs optimized to reduce the charge carrier recombination can be obtained.

7

Conclusions and Recommendations

This chapter gives first a summary of the most important results achieved during this thesis project and then provides recommendations on future research.

7.1. Conclusions

The upscaling process of the thin film solar cells has been divided in three different parts. The three following sections are meant to answer the scientific questions introduced in chapter 1.2.

7.1.1. Optimization of the front contact

In the first part of the thesis project, several different front contact layouts have been analyzed in order to answer to the first scientific question:

Is it possible to design a front contact grid to improve the charge carrier collection in a large area thin film solar cell?

Using the results of optical and electrical power losses simulations a front contact grid has been successfully designed. The number of busbars, the type of TCO, the solar cell technology and the size of the solar cell have been varied in order to analyze their influence on the power loss. Unexpectedly, an optimal design with respect to the total fractional losses could not be found: an increase of the number of busbars and fingers, together with the decrease of their width, progressively reduces the losses and enhances the charge carrier collection. Ideally, a front grid with infinite number of busbars and fingers with infinitesimal dimensions would reduce the total power loss to almost zero. Limitations due to the use of metal evaporation for the deposition of the front contact have been considered as boundary conditions in order to draw the final design. Two different front masks were produced for a-Si:H/a-Si:H solar cells on squared samples of 6.5 cm and 9.5 cm. FTO has been considered as the best TCO to guarantee good performances and reproducibility.

7.1.2. Laser scriber optimization

The second part of the thesis project aimed to answer the second scientific question:

What are the optimal parameters for the isolation of a solar cell by laser scribing and what are the major drawbacks of using a single wavelength infrared laser scriber?

The laser scribing process has been optimized in order to find the correct parameters to ablate the silicon layers both in pin superstrate and nip substrate configuration. The optimization was first based on a visual analysis, and later on the investigation of images made with a Scanning Electron Microscope.

At first, the input parameters of the laser were consistently varied to study their influence on the ablation process. From the very first experiments, it was clear that not only the amount of energy absorbed by the material but also the percentage of pulse overlapping were of fundamental importance. High values of pulse overlapping did not give the material the sufficient time to cool down. This resulted in a strong increase of the material removal rate. It was shown that the variation of the pulse repetition frequency and the laser speed allowed to control the percentage of pulse overlapping.

The material removal rate was also influenced by the laser fluence, that is, the amount of energy absorbed per unit area. The laser fluence could be controlled by varying the pulse width and the percentage of average input power. The higher the laser fluence, the larger was the amount of material removed. Moreover, the reduction of the pulse width led to a higher peak power per incident pulse on the sample. The variation of the peak power, however, was not sufficient to reach the sublimation of the material and melting remained the primary ablating method. Consequently, long laser pulses were used. This also allowed to increase the size of the heat affected zone. When a laser pulse impinges on an already affected area, the material evaporation strongly increases.

In the second step of the optimization process, the scribed lines have been analyzed using the Scanning Electron Microscope. Heat was identified as the major cause of the generation of cracks and other defects. It was also be shown that a high number of marking loops and a high value of pulse overlapping can cause defects. Therefore, the effects of the marking repetition loops and the speed of the laser were optimized.

A low number of marking loops and a high laser speed were needed to avoid the formation of shunting defects. Overall, a laser speed of 2500 mm/s and 100% of the nominal power were found to be the optimum settings for the ablation of both the pin superstrate and of the nip substrate solar cells. The pulse repetition frequency was set to 100 kHz for the first configuration and 200 kHz for the latter, while the optimized pulse widths were 8 ns and 6 ns respectively.

7.1.3. Solar cells deposition

The third and last part of the project was meant to answer the last research question:

Is it possible to deposit large area PIN or NIP solar cells by using the previously optimized techniques?

The optimized front contact grid has been implemented prior to the deposition of large area a-Si:H pin superstrate solar cell, to reduce the charge carrier movement distance to the metallic front contact and the chances of charge carriers of being lost to shunting defects. For the same reason, large area samples of a-Si:H nip substrate solar cells were divided into small cells, which were then interconnected to form a parallel connected mini-module.

At first, a better isolation of the edges of the sample has been achieved. The density of the shunts at the edges is indeed higher than in the central part: pinholes and unpassivated dangling bonds are likely due to the higher irregularity of the surface and the inhomogeneous thickness of the deposited layers. Therefore, heat resistant Kapton tape was used to isolate the central part of the sample from the extremities in the pin superstrate deposition. In the nip substrate configuration the isolation of the edges was instead achieved by laser scribing the solar cells from the front side. A promising increase of the open circuit voltage could be reached.

In order to find the source of the shunting defects, pin superstrate solar cells have been gradually upscaled by depositing several samples. On the one hand, the possible creation of shunts due to the introduction of the 500 nm Al front contact grid has been investigated. On the other hand, the influence of the composition of the front contact on the solar cell performance has been analyzed. Solar cells of 16 mm^2 have been deposited and the deposition order of the AZO layer and the front metallic grid were changed. Furthermore, solar cells of the same dimension have also been deposited on Asahi glass. A first important conclusion was immediately drawn: the introduction of the front contact grid did not generate additional shunts. The reduction in the short circuit current density was indeed only due to the reduced active area caused by the front grid. Secondly, the use of the Asahi glass guaranteed, on average, a 3.5% higher efficiency because the textured surface of the glass enhances the absorption of the light.

The use of Asahi glass gave advantages also in the process of upscaling the solar cell. Working devices of 1 cm^2 have been obtained using this configuration. However, when the AZO layer was used as TCO to make 1 cm^2 solar cells, a working device could not be achieved. Instead, we suspect that the smaller amount of impurities in the industrially deposited FTO on Asahi glasses reduced the quantity of shunting defects in the sample area, and resulted in working solar cells. Nonetheless, even if the Asahi substrate guaranteed the deposition of larger solar cells, shunt resistance values decreased from almost 5200 $\Omega \cdot m^2$ to almost 800 $\Omega \cdot m^2$ when comparing the 16 mm^2 to the 1 cm^2 solar cells. Although the presence of the designed front contact grid reduced the charge carrier movement distance to the contact, the high density of shunts through the a-Si:H bulk material prevented the device from achieving higher efficiencies for larger dimensions.

Similar conclusions were drawn from the analysis of the composition of the back contact of the nip substrate solar cell. The use of a full metal back contac did not result in any working solar cells. The metal evaporation process generated a significant amount of pinholes that increased the possibility of obtaining shunted devices. A protective layer of 200 nm of ITO has been used to reduce the problems related to the large number of defects. Solar cells with metal+ITO and AZO layer as back contact gave good results. The performance of the solar cell with an AZO layer were slightly lower because most of the non absorbed light was almost completely transmitted through the back contact instead of being reflected back into the absorber layer. Despite the fact that working solar cells were deposited, larger working devices could not be obtained even with the implementation of the laser scribing process, due to the large number of shunting defects in the sample.

Overall, several solar cell configurations have been investigated and various problems related to the depositions of pin superstrate or nip substrate configuration have been analyzed. However, large area solar cells were not obtained due to the shunting defect density of the a-Si:H technology.

7.2. Recommendations and outlook for future research

The process of upscaling thin film solar cells at laboratory level still need several improvements to allow the deposition of a large area solar cell.

Different or thicker absorber layers should be tested in order to verify to what extent the upscaling process depend on the intrinsic property of the absorber layer or wether they are related to the upscaling strategy used.

A front grid denser in fingers than the one optimized at the beginning of this thesis project might be an interesting and straightforward solution to overcome the problems related to the inhomogeneity of the material. A dense grid would indeed further reduce the space the charge carriers have to travel and the possibility of occurring in shunting problems.

Furthermore, the material ablation by laser scribing should be also tested in the second working region of the laser, the constant power region. This region allows a better control of fluence of the laser, since the machine works at a constant average output power for each and every pulse width.

Lastly, new design pin and nip solar cells should be tested in order to verify if with different manufacturing technique a working device can be obtained. Laser scribing together with lithography can be tested for a better isolation of the laser scribed lines and to deposit the back metal contact on top of the ablated lines. The use of lithography for material removal and for the isolation of the cells can also be tested as alternative to the laser scribing process, in order to avoid shunting problems deriving from the formation of debris and defects.

A

Laser cut-off frequency

Cut off frequency values depending on the pulse width. Data retrieved from [26]

YDFLP-30M1+-S	
Pulse width [ns]	Cut off frequency [kHz]
6	525
9	360
20	210
30	150
45	113
60	98
80	87
100	83
150	78
250	60

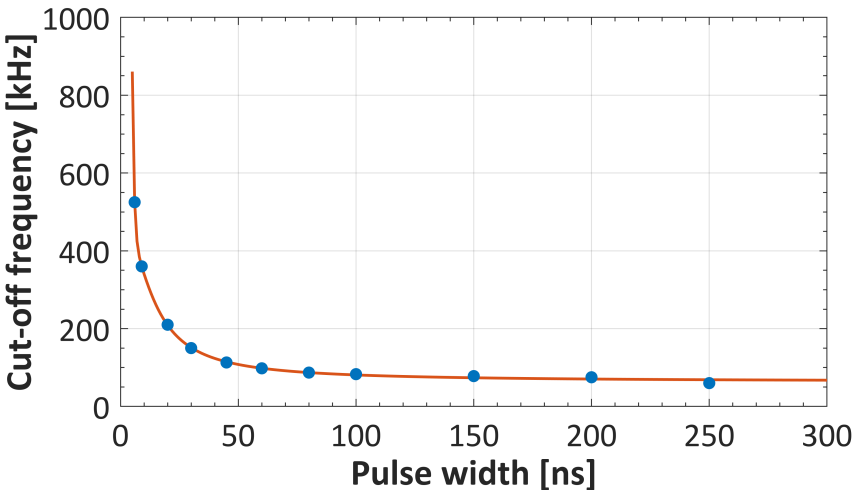

Figure A.1: Curve fitted from the Cut off frequency and pulse width values given in the datasheet [26]

Anlysing the data given in the laser datasheet, it is possible to assume a trend in the relationship between the cut off frequency and the pulse width. By fitting the values it is possible to extract the following cut off frequency-pulse width relationship:

$$f_{\text{cut-off}} = 62.5098 + \frac{1297.23}{Q_{\text{p}}} + \frac{61699.2}{{Q_{\text{p}}}^2} - \frac{696241}{{Q_{\text{p}}}^3} + \frac{2275440}{{Q_{\text{p}}}^4} \tag{A.1}$$

B

Front contact mask for the deposition of the busbars

The following figure shows the mask for the deposition of the busbars designed for the front contact of the nip mini-module.

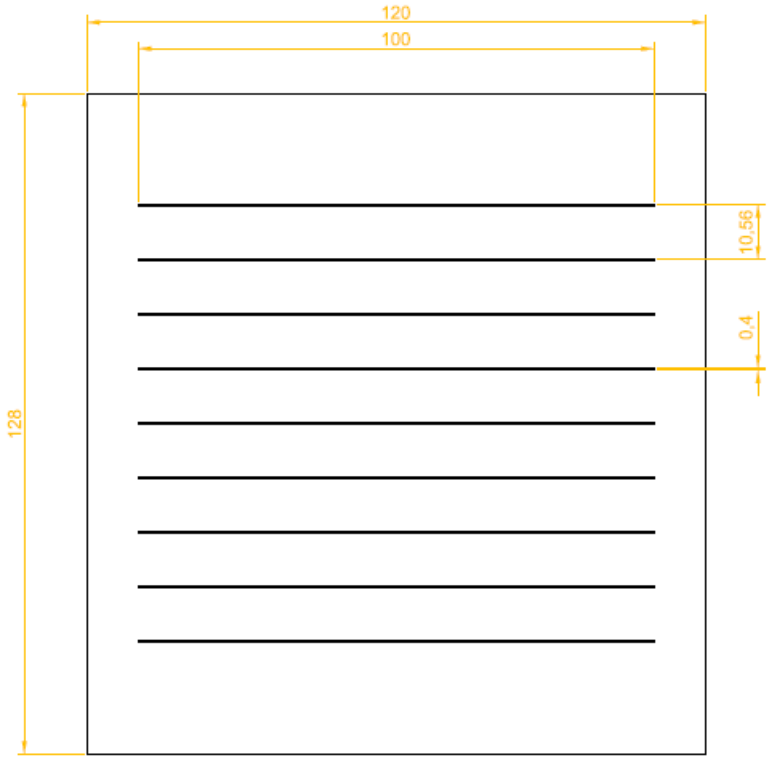

Figure B.1: Mask of the front contact busbars

Bibliography

[1] Jerry Adler. Why fire makes us human, 2013. Accessed: 26/07/2018. Smithsonian Magazine.

[2] Vujica Yevjevich. Water and civilization. *Water International*, 17(4):163–171, 1992. Retrieved from: https://doi.org/10.1080/02508069208686135.

[3] Richard Heinberg and David Fridley. *Our Renewable Future: Laying the Path for One Hundred PercClean Energy*. Island Press, 2016.

[4] cleanenergy2050. Population growth, energy demands and our fossil fuel addiction, 2013. Accessed: 14/08/2018. Retrieved from: https://cleanenergy2050.wordpress.com/.

[5] Bimal K Bose. Global warming: Energy, environmental pollution, and the impact of power electronics. *IEEE Industrial Electronics Magazine*, 4(1):6–17, 2010.

[6] Conserve Energy Future. What is water pollution?, n.d. Accessed: 26/07/2018. Retrieved from: https://www.conserve-energy-future.com/sources-and-causes-of-water-pollution.php.

[7] Carlos Maquieira González. Photoelectrochemical water treatment using solar cells and earth abundant materials. Master's thesis, Delft University of Technology, 2017.

[8] Olindo Isabella, Arno Smets, Klaus Jäger, Miro Zeman, and René van Swaaij. *Solar Energy: The physics and engineering of photovoltaic conversion, technologies and systems*. UIT Cambridge Limited, 2016.

[9] V.C.S. Hamoen. Thin-film silicon triple junction solar cell for solar fuels. Master's thesis, Delft University of Technology, 2017.

[10] Optique pour l'ingénier. Insulator, semiconductor, conductor, 2011. Accessed: 19/10/2017. Retrieved from: http://http://www.optique-ingenieur.org/en/courses/OPI_ang_M05_C02/co/Contenu_02.htmll.

[11] Guangtao Yang. *High-efficient n-i-p thin-film silicon solar cells*. PhD thesis, Delft University of Technology, 2015.

[12] Kazunobu Tanaka, Eiichi Maruyama, Toshikazu Shimada, and Hiroaki Okamoto. *Amorphous silicon*. John Wiley & Sons, West Sussex, UK, 1999.

[13] Michael Stuckelberger, Rémi Biron, Nicolas Wyrsch, Franz-Josef Haug, and Christophe Ballif. Progress in solar cells from hydrogenated amorphous silicon. *Renewable and Sustainable Energy Reviews*, 76:1497–1523, 2017.

[14] Nuno Neves. Azo - the replacement for ito? *Technology Insights*, 3:62–66, 2015.

[15] n.a. Review of tco thin film, 2008. Accessed: 5/03/2018. The Iby and Aladar Fleischman Faculty of Engineering. Tel Aviv University.

[16] Sourabh Dongaonkar, Jonathan D Servaites, Grayson M Ford, Stephen Loser, J Moore, Ryan M Gelfand, Hooman Mohseni, Hugh W Hillhouse, Rakesh Agrawal, Mark A Ratner, et al. Universality of non-ohmic shunt leakage in thin-film solar cells. *Journal of Applied Physics*, 108(12): 124509, 2010.

[17] Stefan Haas, Aad Gordijn, and Helmut Stiebig. High speed laser processing for monolithical series connection of silicon thin-film modules. *Progress in Photovoltaics: Research and Applications*, 16(3):195–203, 2008.

[18] Y Lawrence Yao, Hongqiang Chen, and Wenwu Zhang. Time scale effects in laser material removal: a review. *The International Journal of Advanced Manufacturing Technology*, 26(5-6): 598–608, 2005.

[19] Spectra-Physics Newport. Average and peak power - a tutorial., n.d. Photonic technical Note 1, Power Meters and Detectors.

[20] Paul van Kan. Improving the p1 scribe of the hyet solar module, flexible thin film a-si:h technology. Master's thesis, Delft University of Technology, 2015.

[21] n.a. Magnetron sputtering, n.d. Accessed: 22/05/2018. Retrieved from: Angstrom Sciences https://www.angstromsciences.com/magnetron-sputtering-deposition.

[22] Angstrong engineering. Electron beam evaporation: overview, n.d. Accessed: 23/05/2018. Retrieved from: Angstrom Engineering https://angstromengineering.com/tech/electron-beam-evaporation/.

[23] Lasergraaf. Mopa fiberlaser 30 watt kleur graveren "emma", n.d. Accessed: 24/05/2018. Retrieved from: Lasergraaf.nl https://lasergraaf.nl/product/mopa-fiber-laser-30w-kleur-graveren/.

[24] Rüdiger Paschotta. Fiber lasers. *Encyclopedia of Laser Physics and Technology*, Wiley-VCH (ISBN 978-3-527-40828-3), 2008.

[25] Imrana Ashraf. Laser systems and their applications, 2013. The Abus Salam International Centre for Theoretical Physics.

[26] JPT. 3owatt ytterbium pulsed fiber laser test data, 2017. Datasheet.

[27] Amrita Vishwa Vidyapeetham. Resistivity by four probe method, n.d. Accessed: 05/06/2018. Retrieved from: http://vlab.amrita.edu/?sub=1&brch=282&sim=1512&cnt=1.

[28] Tektronic company Keithley. Techniques for measuring resistivity for materials characterization, n.d.. Accessed: 05/06/2018.

[29] Keithley. 6517a electrometer, n.d.. Accessed: 06/06/2018. User manual.

[30] Temptronic. Tp03000 thermal inducing vacuum platform, n.d. Accessed: 06/06/2018. User manual.

[31] Australian Microscopy & Microanalysis Research Facility. Scanning electron microscope, n.d. Accessed: 01/06/2018. Retrieved from: http://www.ammrf.org.au/myscope/sem/introduction/.

[32] ThermoFisher Scientific. Nova nanosem, n.d. Accessed: 01/06/2018. Retrieved from: https://www.fei.com/products/sem/nova-nanosem/.

[33] Adam De Gree. The history and working principle of the scanning electron microscope (sem), 2015. Accessed: 02/06/2018. Retrieved from: https://www.azonano.com/article.aspx?ArticleID=3995.

[34] Susan Swapp. Scanning electron microscopy (sem), n.d. Accessed: 02/06/2018. University of Wyoming, Retrieved from: https://serc.carleton.edu/research_education/geochemsheets/techniques/SEM.html.

[35] Georgios Papakonstantinou. Investigation and optimization of the front metal contact of silicon heterojunction solar cells. Master's thesis, Delft University of Technology, 2014.

[36] Asahi Glass Company. Vu. tco coated glass for thin film application (a-si/*mu*c-si, n.d. Datasheet.

[37] Guillaume le Boucher d'Hérouville. High efficiency shj/poly-si hybrid solar cells. Master's thesis, Delft University of Technology, 2018.

[38] Lei Hao, Xungang Diao, Huaizhe Xu, Baoxia Gu, and Tianmin Wang. Thickness dependence of structural, electrical and optical properties of indium tin oxide (ito) films deposited on pet substrates. *Applied surface science*, 254(11):3504–3508, 2008.

[39] Fai Tong Si. *Quadruple-junction Thin-Film Silicon-Based Solar Cells*. PhD thesis, Delft University of Technology, 2015.